Title
Additive Manufacturing Processes for Structural and Hybrid Architectured Materials

Author
Xu, Zhenpeng

Publication Date
2023

Peer reviewed|Thesis/dissertation

UNIVERSITY OF CALIFORNIA

Los Angeles

Additive Manufacturing Processes for Structural and Hybrid Architectured Materials

A dissertation submitted in partial satisfaction of the requirements for the degree Doctor of Philosophy in Civil Engineering

by

Zhenpeng Xu

2023

ABSTRACT OF THE DISSERTATION

Additive Manufacturing Processes

for Structural and Hybrid Architectured Materials

by

Zhenpeng Xu

Doctor of Philosophy in Civil Engineering

University of California, Los Angeles, 2023

Professor Mathieu Bauchy, Co-Chair

Professor Xiaoyu Zheng, Co-Chair

Architectured materials have gained significant attention in recent years due to their unique properties and potential applications, such as lightweight structural materials and functional devices. Projection stereolithography is a promising additive manufacturing technique for fabricating these materials with precisely designed geometries. However, several key processing factors have limited the development of this technique. One of the primary challenges of using projection stereolithography is the limited control over printing material properties, especially resin viscosity. High-viscosity resins may not flow easily or could potentially result in the loss of fine details in the final print. Another challenge is structure printability, as the geometrical

arrangement of building blocks to create the desired microstructure may lead to overhanging features or unsupported regions. Such design complexities can result in deformation, detachment, or even collapse of the printed structure. Size scalability is another challenge in projection stereolithography, which is inherently restricted by the pixels of the light engine.

This work focuses on addressing the aforementioned challenges by developing new additive manufacturing processes. Specifically, an extendable multi-material projection stereolithography system integrated with a tape-casting method is developed to create architectured lattice materials made of carbon fiber reinforced polymer composites. This system improves material processability by allowing for precise control of resin fluidity. Then, a light-based approach capable of printing arbitrary micro-architectures with a large array of internally suspended features is presented. This method eliminates the need for manual removal of internal supports, which improves structure printability. It also enables the creation of multi-functional metamaterials with a range of designed properties, including wide bandgaps for elastic waves and switchable wave transmissions. Lastly, a large-scale high-resolution scanning projection stereolithography process integrated with an optical scanning system is presented. This system provides the ability to print unprecedented large-scale parts of 50 cm with a minimal feature size of 50 μm, which enables the fabrication of architectured materials with features spanning over four orders of magnitude for many applications. Overall, these proposed approaches address several critical challenges in the projection stereolithography process and have a profound impact not only on the industry but also on other research works.

The dissertation of Zhenpeng Xu is approved.

Eric M.V. Hoek

Sanjay K. Mohanty

Xiaoyu Zheng, Committee Co-Chair

Mathieu Bauchy, Committee Co-Chair

University of California, Los Angeles

2023

Table of Contents

List of Figures

List of Tables

List of Acronyms

AM Additive manufacturing

CAD Computer-aided design

FDM Fused deposition modeling

MEMS Microelectromechanical systems

CTE Thermal expansion

PSL Projection stereolithography

DLP Digital light processing

LCD Liquid crystal display

DMD Digital micromirror devices

PμSL Projection micro-stereolithography

CFRP Carbon fiber reinforced polymer

UV Ultraviolet

PDMS Polydimethylsiloxane

FEP Fluorinated ethylene propylene

SLA Stereolithography

TMPTA Trimethylolpropane triacrylate

mSLAD Multi-material projection stereolithography technique with dissolvable support

PEGDA Poly(ethylene glycol) diacrylate

BPAEDA Bisphenol A ethoxylate dimethacrylate

MAG Magnetic resin

SEM Scanning electron microscope

NS Negative stiffness

SLS Selective laser sintering

SPSL Scanning projection stereolithography

TSP Traveling salesman problem

FOM Figure of merit

DIW Direct ink writing

TPP Two-photon polymerization

Acknowledgements

I would like to express my gratitude to Prof. Xiaoyu (Rayne) Zheng for dedicating his time to guide and work with me over the past five years. I am grateful for the opportunity Dr. Zheng provided me to explore diverse research areas.

I am deeply grateful to all the members of my committee who assisted me in completing my Ph.D. degree at UCLA.

I would like to acknowledge my group mates at the Advanced Manufacturing and Metamaterials Laboratory (AMML) for their invaluable advice and support.

I would like to express my gratitude to my collaborators, with whom I had the opportunity to work on various projects.

I wish to extend my heartfelt appreciation to my family for their unwavering support throughout my journey. They have always been my pillar of strength, motivating me to strive forward.

I would like to acknowledge UT-Battelle, LLC (4000162266), NSF (CMMI-1727492), US Air Force Office of Scientific Research (FA9550-18-1-0299), US Office of Naval Research (N00014-18-1-2553 and N00014-19-1-2723) and Startup support from Virginia Tech, University of California, Los Angeles and University of California, Berkeley for funding support.

Chapter 3.8 is reproduced from "**Zhenpeng Xu**, Chan Soo Ha, Ruthvik Kadam, John Lindahl, Seokpum Kim, H. Felix Wu, Vlastimil Kunc, Xiaoyu (Rayne) Zheng, Additive manufacturing of

two-phase lightweight, stiff and high damping carbon fiber reinforced polymer microlattices, Additive Manufacturing, 2020, Volume 32, p.101106". DOI: https://doi.org/10.1016/j.addma.2020.101106

Chapter 4 is reproduced from "**Zhenpeng Xu**, Ryan Hensleigh, Nikhil JRK Gerard, Huachen Cui, Mourad Oudich, Wentao Chen, Yun Jing, Xiaoyu (Rayne) Zheng, Vat photopolymerization of fly-like, complex micro-architectures with dissolvable supports, Additive Manufacturing, 2021, Volume 47, p.102321". DOI: https://doi.org/10.1016/j.addma.2021.102321

Chapter 5 is a manuscript in preparation for publication.

Vita

Education

Doctor of Philosophy, Civil Engineering Expected: Mar. 2023
UCLA, Los Angeles, CA
Doctor of Philosophy, Mechanical Engineering Transferred to UCLA, Sep. 2019
Virginia Tech, Blacksburg, VA
Master of Science, Mechanical Engineering Jun. 2018
University of Florida, Gainesville, FL
Bachelor of Engineering, Mechanical Engineering Jun. 2016
Beihang University, Beijing, China

Publications

- J. Wang, R. Hensleigh, **Z. Xu**, Z. Wang, X. Zheng, Y. Rahmat-Samii, Fully 3D-printed lightweight combination of a circularly polarized transmitarray and a feed horn, ***IEEE International Symposium on Antennas and Propagation and USNC-URSI Radio Science Meeting (AP-S/URSI)***, 645-646, 2022.
- H. Cui, D. Yao, R. Hensleigh, H. Lu, A. Calderon, **Z. Xu**, S. Davaria, Z. Wang, P. Mercier, P. Tarazaga, X. Zheng, Design and printing of proprioceptive three-dimensional architected robotic metamaterials, ***Science*** 376, 1287-1293, 2022. (Reported by LA Times, UCLA news, etc.)
- P. P. Indurkar, A. Shaikeea, **Z. Xu**, H. Cui, X. Zheng, V. Deshpande, The coupled strength and toughness of interconnected and interpenetrating multi-material gyroids, ***MRS Bulletin*** 47, 461-473, 2022.
- **Z. Xu**, R. Hensleigh, N. J. Gerard, H. Cui, M. Oudich, W. Chen, Y. Jing, X. Zheng, Vat photopolymerization of fly-like, complex micro-architectures with dissolvable supports, ***Additive Manufacturing*** 47, 102321, 2021.
- M.T. Hsieh, C. S. Ha, **Z. Xu**, S. Kim, H. F. Wu, V. Kunc, X. Zheng, Stiff and strong, lightweight bi-material sandwich plate-lattices with enhanced energy absorption, ***Journal of Materials Research*** 36, 3628-3641, 2021.
- N. J. Gerard, M. Oudich, **Z. Xu**, D. Yao, H. Cui, et al., Three-dimensional trampolinelike behavior in an ultralight elastic metamaterial, ***Physical Review Applied*** 16, 024015, 2021.
- D. Behera, S. Chizari, L. A. Shaw, M. Porter, R. Hensleigh, **Z. Xu**, et al., Current challenges and potential directions towards precision microscale additive manufacturing–Part IV: Future perspectives, ***Precision Engineering*** 68, 197-205, 2021.
- C. Wang, W. Ping, Q. Bai, H. Cui, R. Hensleigh, R. Wang, A. H. Brozena, **Z. Xu**, et al., A general method to synthesize and sinter bulk ceramics in seconds, ***Science*** 368, 521-526, 2020. (Featured on the front cover, reported by c&en, Nanotechnology Now, Yahoo News!, Science

Daily, etc.)

- R. Hensleigh, H. Cui, **Z. Xu**, J. Massman, D. Yao, J. Berrigan, X. Zheng, Charge-programmed three-dimensional printing for multi-material electronic devices, ***Nature Electronics*** 3, 216-224, 2020. (Reported by c&en, Tech Xplore, 3D printing industry, etc.)
- **Z. Xu**, C. S. Ha, R. Kadam, et al., Additive manufacturing of two-phase lightweight, stiff and high damping carbon fiber reinforced polymer microlattices, ***Additive Manufacturing*** 32, 101106, 2020.

Presentations

- **Z. Xu**, R. Hensleigh, et al., Ultra-light antennas via charge programmed deposition additive manufacturing, ***International Mechanical Engineering Congress & Exposition*** (***IMECE2022)***, Columbus, OH, USA, October 2022.
- **Z. Xu**, C. S. Ha, R. Kadam, et al., Additive manufacturing of two-phase lightweight, stiff and high damping carbon fiber reinforced polymer microlattices, ***32nd Annual International Solid Freeform Fabrication*** (***SFF***) ***Symposium***, Virtual, USA, August 2021.

Chapter 1 Introduction

In this chapter, an introduction to additive manufacturing techniques, structural and hybrid architectured materials is presented. The chapter concludes by outlining the initiation and objectives of the studies. The primary aim of this chapter is to provide readers with a comprehensive understanding of the context and rationale behind the research presented in this dissertation.

1.1 Additive manufacturing

Additive manufacturing (AM), also known as 3D printing, is a rapidly growing technology that has revolutionized the way we manufacture products. The AM process involves building three-dimensional objects by adding material layer-by-layer. It starts with a 3D model created using computer-aided design (CAD) software. The model is then sliced into thin layers, and the AM machine deposits material, typically a thermoplastic or metal, layer-by-layer to create the final product. The process is highly customizable, enabling the production of complex shapes and geometries that were previously impossible or difficult to produce.

AM has several meanings and implications for society, including:

1. Customization and personalization: AM enables the production of highly customized and personalized products, from medical implants to consumer goods. This can lead to improved quality of life for individuals with specific needs and preferences.

2. Manufacturing of complex geometries: AM technology allows for the production of complex geometries that would be difficult, if not impossible, to produce using traditional manufacturing techniques. This allows for the creation of innovative designs that were previously unachievable.
3. Reduced time-to-market: AM technology allows for rapid prototyping and iteration, which significantly reduces the time it takes to bring a product to market. It eliminates the need for tooling, which is a significant time and cost factor in traditional manufacturing.

In conclusion, AM has the potential to transform the way we design and manufacture products. It enables greater customization and personalization, reduces waste and environmental impact, and offers economic benefits through distributed manufacturing and new business opportunities. Additionally, AM has the potential to revolutionize healthcare by enabling the production of personalized medical implants and prosthetics and creating new opportunities in drug delivery and tissue engineering.

The adoption of AM is not without challenges. The technology requires significant investment in both hardware and software, and there are still limitations in terms of materials, speed, and scalability. Despite these challenges, the potential benefits of AM for society are significant, and it is likely that the technology will continue to grow and mature in the years to come.

In this work, the author addresses a range of challenges associated with different AM processes and proposes innovative solutions to overcome them. By leveraging advances in materials science, process control technologies, and data analytics, the proposed solutions expand the capability of AM processes and applications.

1.2 Architectured materials

Architectured materials with tailored geometries exhibit extraordinary structural and multi-functional properties that are not observed in nature, making them attractive candidates for applications in energy absorption [1, 2], wearable electronics [3, 4], acoustics [5-7], etc. Metamaterials with rationally designed architectures can be realized through AM technologies with the goal of creating materials with digital control of the spatial distribution of micro-architectures [8-10]. Extremal mechanical properties and behaviors, including cloaking [11], Penta-mode [12], negative stiffness [13-16], extreme Poisson ratios [17, 18], and transformative behaviors [19-22], can be inversely designed into a digital 3D model that could be replicated via AM.

The design principles behind architectured materials can be broadly categorized into two main categories: geometry-based design and topology-based design. Geometry-based design involves controlling the shape, size, and orientation of the building blocks that make up the material's architecture, while topology-based design involves controlling the connectivity and arrangement of these building blocks.

Architectured materials have been used in a wide range of applications, from the iconic Eiffel Tower to micro-structures in diamonds. The Eiffel Tower, a wrought iron lattice tower located in Paris, France, is an excellent example of the use of structural architecture in engineering. The tower's intricate lattice design provides both strength and stability, enabling it to withstand high winds and other external forces. At the microscale, diamond is an example of a material that has a highly structured architecture. The arrangement of carbon atoms in a diamond crystal lattice

provides it with unique physical properties, including exceptional hardness and thermal conductivity. By mimicking the architecture of diamonds at the nanoscale, scientists have been able to develop novel materials with similar properties, such as ultra-hard coatings and thermal management materials.

Architectured materials have found widespread application in various fields, including aerospace, automotive, biomedical, and energy, owing to their unique properties. For instance, in aerospace and automotive applications, architected materials have been utilized to create structures that are both lightweight and mechanically robust [23]. In biomedical applications, they have been used to fabricate scaffolds for tissue engineering and drug delivery systems [24]. Moreover, in the energy sector, architected materials have been employed to improve the performance of batteries and fuel cells [25]. They have also been leveraged to design materials with distinctive optical and acoustic properties, thus expanding their applications to fields such as photonics and acoustic metamaterials.

- Architectured materials can be fabricated using a wide range of techniques, each offering unique advantages and limitations. Fused deposition modeling (FDM) is a type of AM technique that involves the extrusion of a thermoplastic filament to create a desired 3D shape. FDM is a popular technique for creating architectured materials due to its ability to create complex geometries with ease.
- Casting is another commonly used technique for fabricating architectured materials. This process involves the pouring of molten material into a mold that has the desired microstructural pattern. Once the material solidifies, the mold is removed, leaving behind

the final product. Casting is a versatile technique that can be used with a variety of materials, including metals, polymers, and ceramics. However, the complexity and resolution of the structure are of utmost concern.

- Lithography is a widely used technique for fabricating architectured materials due to its versatility and precision. This process involves the use of light to create a pattern on a photosensitive material, which is then used to create the desired microstructure. Lithography can be used to create high-resolution patterns and is commonly used in the production of microelectromechanical systems (MEMS).

In summary, the choice of fabrication technique depends on the specific properties and characteristics required for the application, as well as the desired microstructure of the material. As new materials and applications emerge, researchers continue to explore new fabrication techniques to further expand the possibilities of architectured materials. This work involved developing a profound comprehension of architectured materials, designing and additively manufacturing various architected materials intended for structural applications.

1.3 Hybrid materials

Hybrid materials are a class of materials that combine two or more different materials, each with distinct properties, to achieve synergistic or enhanced mechanical, chemical, or other physical properties. The combination of materials can be done at different length scales, ranging from atomic to macroscopic levels, and can result in a wide range of material properties.

The properties of hybrid materials depend on the properties of the individual materials used, the processing method, and the microstructure of the resulting material. Therefore, the design and fabrication of hybrid materials require a deep understanding of the properties of the constituent materials and the interactions between them.

The utilization of hybrid materials has witnessed remarkable growth in recent years, primarily owing to their distinctive properties and enormous potential for diverse applications. The aerospace industry, for instance, has leveraged hybrid materials to fabricate sturdy yet lightweight materials capable of withstanding extreme conditions [26]. Apart from exceptional mechanical properties, such as high stiffness and strength, hybrid materials can have various functional properties like piezoelectric [9], electromagnetic, shape-memory, thermal, and acoustic properties etc. The creation of these multi-functional materials involves the amalgamation of functional materials with rationally designed micro-structures. Several research studies regarding hybrid materials are reviewed below.

- Xu et al. presented a novel approach to address the trade-off between the coefficient of thermal expansion (CTE) and structural efficiency by demonstrating a lightweight bi-material thermal metamaterial [27]. This metamaterial exhibits not only remarkable stiffness and strength but also a broad range of tunable CTE. They achieved this by combining two distinct mechanisms of thermal expansion illustrated in a tetrahedron and incorporating them into an octet-truss lattice. This allowed them to produce tunable CTE values, including negative, zero, or positive, while maintaining the excellent mechanical

properties of the material. The demonstrated metamaterial can find broad applications in various fields, such as aerospace systems, antennas, and more.

- Yu et al. showcased the effectiveness of stimuli-responsive acoustic metamaterials that extend the two-dimensional phase space to three dimensions via the rapid and repeated alteration of the constitutive parameters' signs using remote magnetic fields [22]. These metamaterials contain magnetoactive lattice structures whose effective modulus can be reversed between positive and negative within controlled magnetic fields. The demonstrated metamaterials possess a wide range of applications, including remote, rapid, and reversible modulation of acoustic transportations, refraction, imaging, and focusing on subwavelength regimes.
- Zhang et al. developed biocompatible and biodegradable composite shape-memory structures that can be triggered by a magnetic field [28]. The authors experimentally investigated the shape memory effect of these printed structures. The printed shape memory lattices have potential applications in healthcare and biomedicine due to their biocompatibility and biodegradability.

Hybrid materials offer a promising approach for creating materials with tailored properties for specific applications. With advancements in material science and processing techniques, hybrid materials have the potential to revolutionize industries. In this study, the author presents the development of several types of hybrid materials enabled by AM techniques.

1.4 Research goal and research framework

The aim of my research is to develop innovative AM processing techniques, particularly projection stereolithography (PSL), that harness the potential of 3D micro-architectures and diverse materials, with the goal of fabricating materials with various applications.

To achieve my research objective, I have developed a research framework, as illustrated in Fig. 1-1, with a focus on three key aspects: process, structure, and property.

I started with developing novel AM processes capable of fabricating architectured materials with complex 3D topology using various materials.

Then, I designed and manufactured structures incorporating multi-scale feature sizes and multi-phase materials.

Finally, I conducted investigations into the structural properties that arise from the unique combination of these structures and materials.

The advanced fabrication techniques that we developed enabled us to create multi-functional materials with distinctive mechanical, acoustic, and magnetic properties. This, in turn, opened up new opportunities for exploring the potential of 3D-printed architectured materials.

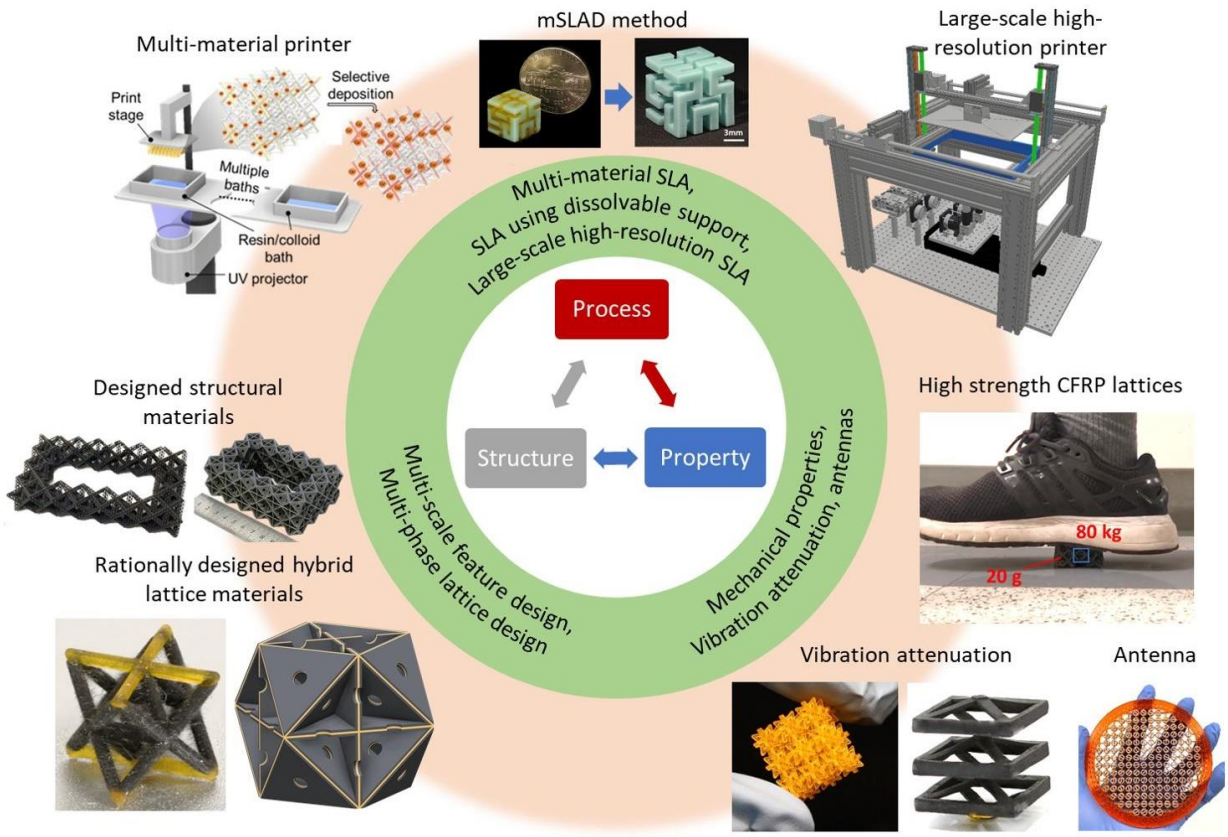

Figure 1-1 Research framework.

1.5 Research questions

The dissertation's primary research questions are presented below, and their corresponding responses are provided in the subsequent chapters.

Research Question 1 How to enable the printing of highly viscous composites for use in projection stereolithography?

Research Question 2 How to print architectured materials with numerous inner overhangs at the micro-scale?

Research Question 3 How to develop new AM processes to increase the building area of projection stereolithography while maintaining a high level of resolution?

Research Question 4 What are the new opportunities enabled by projection stereolithography?

1.6 Dissertation outline

The projection stereolithography process presented in this work is built upon pre-existing AM techniques. However, the incorporation of distinct materials, topologies, and multi-scale feature sizes creates new scientific challenges. This dissertation is structured with each chapter, from 3-5, dedicated to addressing these individual challenges. Specifically, the author identifies the unique problems associated with each challenge and presents original contributions toward overcoming them.

Chapter 2 provides a comprehensive review of the current status of projection stereolithography processes. The fundamental theory underlying these processes is thoroughly explained. Furthermore, a detailed discussion of the advantages and disadvantages of available projection stereolithography technologies is presented, comparing them with traditional manufacturing processes and other AM technologies. Additionally, an in-depth literature review of the most advanced projection stereolithography processes is included, highlighting the limitations of each technology in terms of fabrication capability, production speed, and manufacturing cost. Lastly, this chapter presents the scientific challenges and research objectives

required to develop each process as a solution. Overall, this chapter provides a thorough and informative analysis of the current state of projection stereolithography processes and highlights the areas where future research and development efforts are needed to overcome the current limitations.

Chapter 3 focuses on the development of an extendable multi-material projection micro-stereolithography process capable of producing cellular materials with carbon fiber reinforced composites.

The fiber-reinforced composites exhibit superior mechanical properties. Leveraging the free-forming capability of AM, the author expanded on this concept and developed a series of truss-based lattices, subsequently studying their mechanical behavior. Furthermore, inspired by the upper bounds of the stiffness-loss coefficient in a two-phase composite, the author designed and additively manufactured carbon fiber reinforced composites (CFRP) microlattices with a soft phase architected into selected stiff-phase struts. The results, confirmed by experimental and analytical calculations, revealed that the damping performance could be significantly enhanced by adding only a small fraction of the soft phase. The presented design and AM strategy allow for optimizing mutually exclusive properties. As a result, these CFRP microlattices achieved high specific stiffness per density comparable to commercial CFRP, technical ceramics, and composites while dissipative as elastomers.

Chapter 4 presents the development of a selective dissolution method (mSLAD) for support structures. The author developed a novel light-based additive manufacturing approach, which is capable of printing arbitrary micro-architectures comprising a large array of internally suspended

features, large span overhang, and high aspect ratio struts. This method eliminates the need for manual removal of internal supports and enables a suite of multi-functional metamaterials with a range of designed properties, including wide bandgaps for elastic waves at low frequency, switchable wave transmissions, and products requiring no post support removal. The author describes the synthesis and rapid printing of a variety of metamaterials comprising an extensive array of suspended features and demonstrates their metamaterial behaviors. The proposed approach removes scale and unit cell limitations and is capable of achieving embedded features across multiple materials.

Chapter 5 presents the development of a large-scale high-resolution scanning projection system. The system integrates an optical scanning system to expand the printing scale to over 50 cm while reducing printing time through optimized scan paths. The author demonstrates the capability of this system by additively manufacturing lightweight architected lattice materials of various sizes using carbon fiber reinforced polymer. The system provides concurrent ability to print unprecedented large-scale parts of 50 cm with a minimal feature size of 50 μm, thereby enabling the fabrication of metamaterials with features spanning four orders of magnitude for many applications. The author successfully printed a range of lattice structures as well as a car bumper energy absorber that spans over 1 meter in length. This innovative technique opens up new possibilities for the efficient production of complex architectures that demand intricate features and large sizes.

Chapter 6 summarizes the study's main findings and contributions while also outlining future research directions to address the identified limitations and challenges in projection stereolithography processes.

Chapter 2 Overview of projection stereolithography

This chapter provides a comprehensive review of the current state of PSL processes. It starts by thoroughly explaining the fundamental theory underlying these processes. Next, an in-depth literature review of the most advanced PSL processes is presented, which highlights their limitations in terms of fabrication capability, production speed, and manufacturing cost. Furthermore, this chapter identifies the scientific challenges and research objectives required to develop each process as a viable solution. Overall, Chapter 2 offers a thorough and informative analysis of the current state of PSL processes and emphasizes the areas where future research and development efforts are required to overcome current limitations.

2.1 Introduction

Projection stereolithography, also known as digital light processing (DLP), is a type of 3D printing technology that uses a digital projector to create 3D objects. It is a form of stereolithography (SLA), which is an AM process that involves curing liquid resin using a laser.

In PSL, a digital projector shines light onto a vat of liquid resin, which is typically a photopolymer that cures when exposed to light. The projector displays a 2D cross-sectional image of the object to be printed onto the surface of the liquid resin. The resin solidifies in the areas where the light hits, and the build platform moves, allowing the projector to display the next layer of the object. The process repeats until the entire object is printed. A more detailed step-by-step process is described below.

1. Preparing the digital model: The first step is to prepare a digital model of the desired 3D object using CAD software.
2. Generating the slicing file: The digital model is then processed using slicing software to convert it into a series of cross-sectional layers.
3. Setting up the printer: The printer is prepared by loading the resin into the vat and setting up the build platform.
4. Calibrating the printer: The printer's calibration is checked to ensure that the light source, resin, and build platform are correctly aligned.
5. Starting the print: Once the printer is set up, the printing process begins. The build platform is lowered into the resin vat, and the first layer of the object is exposed to UV light, which cures the resin and solidifies the layer.
6. Successive layer printing: The build platform is then raised by a distance equivalent to the thickness of the next layer, and the process is repeated. The projector displays the image of each layer onto the surface of the resin, curing it and building up the object layer by layer.
7. Finishing the print: Once the printing is complete, the object is removed from the printer and rinsed in a cleaning solution to remove any uncured resin. The object is then cured in a UV oven to strengthen the material.
8. Post-processing: Post-processing may involve sanding or polishing the object to remove any roughness or blemishes, painting, or adding other finishing touches as required.

The dynamic mask plays a critical role in the PSL process, and it can be implemented using either a liquid crystal display (LCD) or digital micromirror devices (DMD). In the past, an LCD panel

was used to manipulate pixels and control light patterns by changing the orientation of liquid crystal molecules. However, one of the limitations of using LCD devices is their limited UV light transmissivity, making them unsuitable for high-power UV applications. As a result, modern PSL systems more commonly employ DMD chips as the dynamic mask due to their smaller pixel size, faster response times, and superior UV transmissivity.

There are two types of PSL processes, top-down and bottom-up configurations, each with distinct advantages and disadvantages [29]. In top-down PSL, the resin is placed on a flat platform, and the UV light is projected from above to cure each layer. This configuration provides excellent resolution but may be limited in the size of the structures that can be created. In contrast, bottom-up PSL involves placing the resin in a vat and curing the material from the bottom up, layer by layer. This configuration is suitable for creating large structures, but it may suffer from inferior resolution due to the membrane and support panel between the light source and the resin. Both top-down and bottom-up PSL have been widely used in various fields, and advancements in the technology have led to improvements in speed, resolution, and scalability, making PSL a promising manufacturing technique for the future.

In this study, the author employed the bottom-up configuration in most of the PSL system setups due to several advantages, including the ability to process viscous resin and the reduced amount of resin required for printing large samples. By building the object on the build plate and using a constrained surface, the printing process was able to accommodate the use of viscous resin that would have been difficult to work with using other printing configurations. In addition, the bottom-

up configuration allows for the printing of large samples with less resin, which reduces the material costs and waste associated with the printing process.

2.2 State of the art

To date, numerous outstanding works have been published on advanced PSL processes, specifically in terms of their resolution, fabrication capability, and production speed.

Sun et al. developed a high-resolution projection micro-stereolithography (PμSL) system, which was used to fabricate intricate 3D microstructures for application in MEMS [30]. The study involved the quantification of the photo-curing process, and the technique achieved a remarkable resolution, with the smallest feature produced measuring 0.6 μm.

Cui et al. presented a design and manufacturing approach to produce piezoelectric materials with arbitrary piezoelectric coefficient tensors that were previously inaccessible [9]. Their approach involves the manipulation of electric displacement maps from families of structural cell patterns. They used PSL to fabricate free-form perovskite-based piezoelectric nanocomposites with complex three-dimensional architectures. The resulting piezoelectric metamaterials exhibit high specific piezoelectric constants and tailored flexibility while using only a fraction of their parent materials. The activated piezoelectric metamaterials demonstrate selective suppression, reversal, or enhancement of voltage response at a given mode with applied stress. This approach has the potential to enable the creation of intelligent infrastructure capable of performing structural and functional tasks, such as simultaneous impact absorption and monitoring, three-dimensional pressure mapping, and directionality detection, in the next generation of materials.

Tumbleston et al. achieved the continuous printing of monolithic polymeric parts with feature resolution below 100 micrometers, up to tens of centimeters in size, using PSL [31]. They employed continuous liquid interface production by incorporating an oxygen-permeable window beneath the ultraviolet (UV) image projection plane, which creates a "dead zone" (persistent liquid interface) that inhibits photopolymerization between the window and the polymerizing part. The researchers identified critical control parameters and demonstrated the capability of drawing complex solid parts out of the resin at rates exceeding hundreds of millimeters per hour. This high printing speed enables the production of parts in minutes rather than hours.

Walker et al. developed a stereolithographic 3D printing method for polymeric components that utilizes a mobile liquid interface (fluorinated oil) to reduce the adhesive forces between the interface and the printed object, enabling continuous and rapid printing [32]. The direct cooling provided by the flowing oil enables printing without thermal limitations on the bed area. The researchers achieved continuous vertical print rates exceeding 430 millimeters per hour, with a volumetric throughput of 100 liters per hour. Additionally, proof-of-concept structures made from hard plastics, ceramic precursors, and elastomers were successfully printed using this technique.

2.3 Scientific challenges and research objectives

2.3.1 Material processability

The material processability in PSL is highly dependent on the viscosity and curing behavior of the resin. The resin viscosity must be optimized to enable effective processing by the PSL system. Resins that are too viscous may not flow easily or may lead to a loss of fine details in the final

print. The curing behavior of the resin is another critical factor in the material processability in PSL. The resin should have a suitable curing rate to allow for effective solidification during the printing process. The curing rate must also be carefully matched to the intensity and wavelength of the light source used in the PSL system.

Furthermore, the material processability in PSL is influenced by several other factors, including the light sources characteristics, such as intensity and focus, and the build parameters, such as layer thickness and exposure time. These factors must be carefully optimized to ensure high-quality 3D-printed parts.

2.3.2 Structure printability

Among additive fabrication approaches, including FDM, selective laser sintering (SLS), and material jetting, the light-based technique is the best method suitable for micro-architected metamaterials due to its high resolution (<100 μm) and robust mechanical properties of photopolymers [33]. However, only a small fraction of inversely designed architectures can be realized [34], as current AM is still limited to self-supporting architectures with a small number of unit cells [35].

Different from traditional manufacturing techniques, AM process joins materials together in a layer-by-layer fashion. Overhanging and free-hanging features that lack continuous support layers in the previous build volume cannot be directly manufactured, imposing a design limitation. Therefore, the need for support scaffolding and structures has been well appreciated from the early stages of the AM techniques development [35-37]. In most cases, light-based printing techniques

use support materials made of the same constituents, which later have to be manually removed in post-processing [38]. These limitations make the realization of highly complex metamaterials elusive, as internal supports within an extensive array of unit cells cannot be manually removed due to the blockage of internal areas by the complex 3D features. This limitation is becoming increasingly acute as inversely designed 3D topologies aided by topology optimization and artificial intelligence become commonplace [39, 40].

2.3.3 Size scalability

PSL is particularly well-suited for the fabrication of architected metamaterials, as it allows for the creation of intricate geometries and architectures that are difficult or impossible to achieve using traditional manufacturing techniques [41]. Despite its many advantages, however, PSL is often limited to small-scale production due to the inherent restrictions imposed by the resolution of the light engine [29, 42].

To achieve large-scale and high-resolution 3D printing using PSL, researchers have explored various approaches. Lee et al. (2015) [43] proposed a tiling process wherein small high-resolution tiles were sequentially projected across the resin surface. However, the work circumvented the layer fabrication time problem by tiling 2D patterns across the entire resin surface. Emami et al. (2014) [44] and Meenakshisundaram et al. (2019) [45] also attempted to eliminate size restrictions by mounting the projection unit on an X-Y stage and continuously moving the projector along with the exposure process. While achieving perfect blending of each section and high resolution became computationally expensive as the complexity of the part geometry increased. Zheng et al. (2016) [46] developed a scanning PSL process using a fixed projection and X-Y scanning galvo-mirrors.

While the use of a flat-field scan lens solves the keystone problem, manufacturing large flat-field lenses remains a challenge, limiting scalability for industrial manufacturing. To date, none of the reported PSL systems has demonstrated the 3D printing of architectured lattice structures larger than 50 cm. This limitation hinders the efficient production of commercial products, metamaterials, and large-scale antennas [47, 48] that require both large sizes and intricate features.

2.3.4 Research objectives

Material processability, structure printability, and size scalability are three critical factors that determine the success and capability of AM techniques. This dissertation focuses on using PSL to create architected structural hybrid materials. Specifically, the author investigated the 3D printing process for highly concentrated carbon fiber reinforced composites and developed a method to print complex architectures with inner overhangs. Furthermore, the author proposed a technique to enlarge the printing area of the PSL. This dissertation highlights the importance of optimizing the AM process for specific materials and structures to enable the creation of advanced architected materials with desirable properties.

The dissertation's main research objectives are as follows:

1. To understand the projection stereolithography process and comprehensively characterize the material processability of 3D printable feedstock;
2. To develop new advanced 3D printing techniques and discover their potential applications;
3. To investigate feasible methods for 3D structure printability and explore possible structural materials with extreme performance.

Chapter 3 AM of strong and tough carbon fiber reinforced composites for structural applications

This chapter outlines the development of an extendable multi-material PSL system and its application to carbon fiber reinforced polymer composites. The section begins with an introduction to the development of the composites, followed by a demonstration of the fabrication capability using representative samples with multi-scale features. The third section investigates factors that affect the printability of the resin, such as viscosity and cure depth, with the ultimate goal of achieving optimal printing results. Mechanical testing of bulk CFRP composites is then performed and verified by theoretical analysis. The octet-truss based CFRP lattices are fabricated using this methodology and subjected to mechanical testing. The size effect of the CFRP lattices is analyzed, and finally, a group of two-phase lightweight, stiff, and high-damping CFRP microlattices is introduced.

3.1 Development of carbon fiber reinforced polymer composites

A UV-curable CFRP composite, made of a UV-sensitive resin reinforced with short carbon fibers, was developed for fabrication. The matrix materials contained methacrylated monomers and oligomers (Formlabs Rigid, Formlabs Inc). A photoinitiator, phenylbis (2,4,6-trimethylbenzoyl) phosphine oxide (Sigma-Aldrich Inc), was added to the fiber-matrix mixture for photopolymerization. The fibers were obtained from E&L Enterprises, Inc (PC100). A high-energy ball mill was used to mix the monomer, photoinitiator, and carbon fiber (up to 20 vol% loadings). This mixing method ensured a uniform spatial distribution of the fibers (Fig. 3-1).

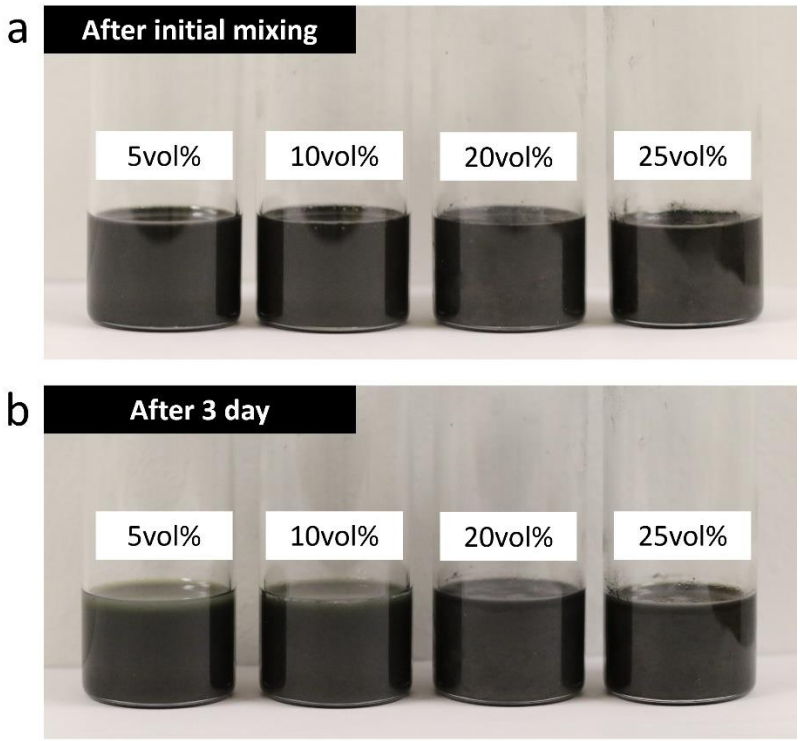

Figure 3-1 Optical images of the CFRP resins mixed with different carbon fiber loadings. (a) After initial mixing. (b) After three days. The resins are stable, and the sediment phenomenon is not obvious.

Resins reinforced by different fiber loadings were formulated. These resins after curing exhibited higher stiffness than that of the base monomer, with measured tensile stiffness increased from 2.47 GPa to 3.02 GPa with an addition of 5 vol% of fibers. The fibers had a diameter of 5 μm and an average length of 70 μm (measured by ZEISS SteREO Discovery.V20).

3.2 Development of an extendable multi-material PμSL system

Based on the work of D. Chen et al. [17, 49, 50], a multi-material PμSL system that could print viscous multiply resins via a recoating fixture and a material switching system was designed and

built, as shown in Fig. 3-2a. To fabricate a multi-material part, a CAD model was sliced into different groups of closely spaced images such that each group represented one material. These two-dimensional slices were subsequently digitized and sent to a DMD chip which projected an image at 405 nm wavelength through a series of lenses onto the corresponding photosensitive resin. This process initiated the polymerization of the resin, converting it into a solid single-layer part that had the same shape as the projected images. Each cured layer was followed by a recoating process in which the build platform was raised, allowing the resin to settle for the next layer. The recoating process for CFRP resin was achieved by a doctor blade, which will be discussed later. If the other material needs to be fabricated in the same layer or the next layer, the transition stage will move the washing vat to the position of the platform. Then, a cleaning dispenser will be used to clean the previously printed part. After cleaning, the platform moved to the other resin vat to print the next layer.

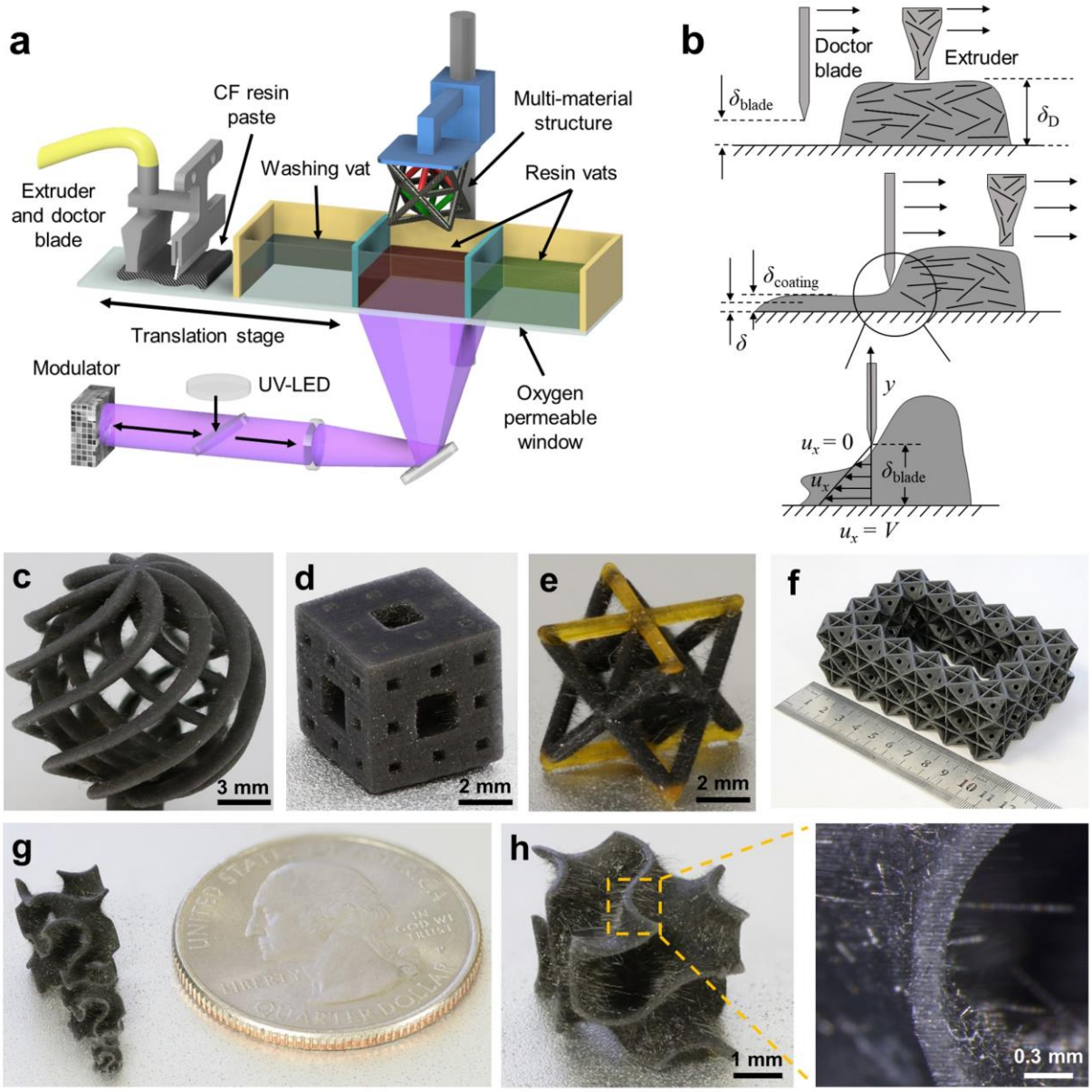

Figure 3-2 Customized multi-material PμSL system and fabricated samples. (a) Schematic of multi-material PμSL process integrated with the tape-casting method. (b) Schematic of the recoating process. (c)-(d) Complex 3D structures fabricated by the system. (e) A multi-material octet-truss unit cell comprising CFRP and polyethylene glycol diacrylate (PEGDA) resin. (f) A closed-cell lattice with a dimension over tens centimeters. (g-h) Gyroid 3D structure with a wall thickness of 150 μm.

Our PμSL system was designed to achieve a minimum printable 3D feature size of ~50 μm in the projection plane. This was determined by the pixel resolution of the DMD array and the printing area. The resolution in the vertical direction was determined by a driving motor, which was 5 μm, and we set the layer thickness as 40 μm. After printing, all samples were cleaned with ethanol and post-cured using the UV light. This process was followed by thermal post-cure at 150°F for 24 hours. To demonstrate the capabilities of our technique, samples with complex 3D structures in millimeter-scale were fabricated, as shown in Fig. 3-2c and 3-2d. Fig. 3-2e shows a multi-material octet-truss unit cell comprising CFRP and PEGDA, and Fig. 3-2g and 3-2h show a gyroid structure with a minimal feature size of 150 μm. The process is not limited to the dimensions demonstrated in microlattices here, while it can be extended to samples of tens of centimeters or larger, as shown in Fig. 3-2f.

To process highly viscous fiber-loaded resin (μ~7.8 Pa.s), we developed a recoating fixture employing the tape-casting technique [9, 51] to ensure the viscous resin was efficiently recoated as shown in Fig. 3-2b. Firstly, a small amount of CFRP was extruded onto the oxygen-permeable window. Then, a doctor blade was moved from left to right, spreading the resin on the window. The blade had a speed of $V = 5$ mm/s relative to the window. The distance between the blade and window δ_{blade} was controlled to ensure that the resin's height was high enough and it could spread to the whole printing area. The thickness of the coating layer $\delta_{coating}$ is half of δ_{blade}. Moreover, to guarantee each layer could be fully cured, $\delta_{coating}$ was set as $\delta_{coating} > k\delta$ ($k > 1$), where δ is the layer thickness and k is the safety factor. The recoating quality of different fiber loading resins was tested (Fig. 3-3), and we observed that the maximum fiber loading that yielded a layer with good

quality was approximately 20 vol%. For the resin that had fiber loading more than 20 vol%, the fibers massed into clusters during the recoating process, making the resin non-printable.

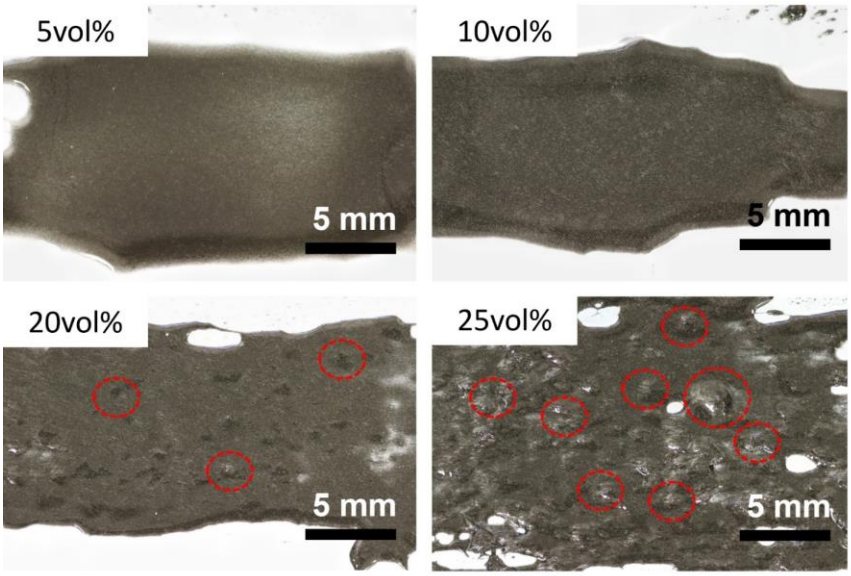

Figure 3-3 Optical images of CFRP resin films with different fiber loadings after recoating. Circled areas refer to pieces of a dense cluster of massed fibers. While some clusters may be present in a 20 vol% resin film, they can still be used for fabrication purposes. However, the situation worsens when the fiber loading increases to 25 vol%, making the recoating process more challenging.

3.3 Cure depth characterization of CFRP resins

3.3.1 The effect of carbon fiber concentration on cure depth

Fig. 3-4 shows the measured cure depth of the CFRP resins with a range of different fiber loadings. Each value is averaged over 5 measurement points. Here, in order to get an idea of how the fiber loading affects the cure depth, we vary the loading from 0 to 15 wt% while maintaining the fiber type and other parameters to be the same. For a specific fiber loading, we observe that the cure

depth shows an exponential relation with the exposure energy. For example, for the resin without any carbon fiber, the trendline approaches an asymptotic value of the cure depth to be approximately 600 μm when the exposure energy is larger than 25 mW/cm^2. Similar cases can be found for other resins. Moreover, we found that adding carbon fiber significantly reduces the cure depth even for a fiber loading of only 5 wt%. With the same exposure energy, the cure depth of 5 wt% CFRP resin is only ~100 μm, while the resin without any fiber can be as large as 600 μm. When the fiber loading increases further, the cure depth continues to decrease. This finding implies that CFRP resin is not easy to be cured, and one needs to optimize the printing parameters carefully before printing.

Adding carbon fibers to the matrix can add functionality to the resin while posting challenges for UV curing because the fiber suspensions can have very high turbidity due to radiation scattering. The scattering-induced turbidity limits the distance of penetration into the resin and largely reduces the cure depths. The curing process can be modeled from the Beer-Lambert law: $Z_{cd} = (1/\alpha) \cdot \ln(E/E_c)$, where α is the resin absorption coefficient, E is the actual energy of light, and E_c is the critical exposure energy required to initiate polymerization [52]. Our test results show a promising trend that agrees well with the theory. The obtained diagram can be used as a guide map for selecting printing parameters for specific resin. For example, when dealing with 5 wt% resin, a cure depth of 100 μm with an exposure energy of 21.25 mW/cm^2 can be found from the plot. Then, one could define each layer's exposure time based on the system's light intensity. Usually, higher light intensity is preferred as it can reduce the curing time. For example, our system has a maximum light intensity of 1.2 mW/cm^2, and an exposure time of ~18 s can be used to achieve a

cure depth of 100 μm for the 5 wt% CFRP resin. To ensure the bounding between adjacent layers, a layer thickness of 50 μm, half of the cure depth, can be set for the printing.

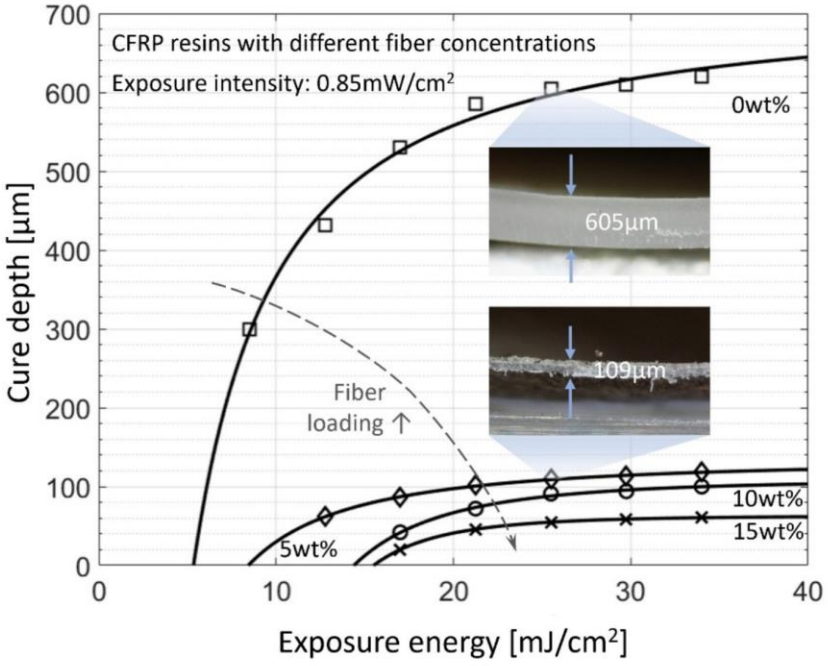

Figure 3-4 Cure depth as a function of energy density for CFRP resin with different fiber concentrations. The CFRP resins are composed of Formlabs 10k resin and a certain amount of short carbon fibers (average length of 70 μm). The two insets are cross-sectional views of the cured layer.

3.3.2 The effect of initiator concentration on cure depth

It is worth noting that when the fiber loading is as high as 15 wt%, the cure depth is only ~60 μm, even if the exposure time is over 40 s, according to Fig. 3-4. Such a long exposure time is not desired as it will prolong the printing process. It was found that the CFRP resin is not very active upon UV light when carbon fibers are present in the resin, although the matrix material already

contains photoinitiators. We found that adding more photoinitiators makes the resin more sensitive to UV light and thus allows for an increased depth of cure at the same exposure energy.

Qualitative results of cure depth and the effect of the initiator are presented in Fig. 3-5. Irg 819 (0, 1, 2 wt%) was added to 15 wt% CFRP for the measurements. The result shows that the curing depth of the resin is significantly increased when 1 wt% initiator is added. For example, for an exposure energy of 20 mJ/cm^2, we can see the cure depth increase from 40 to 80 μm, doubled for resin without an initiator. While when further increasing the concentration to 2 wt%, the increase is not much from 1 wt%. Nevertheless, this result shows that the initiator plays an important role in the curing process, and one could manipulate the initiator's concentration to control such a process.

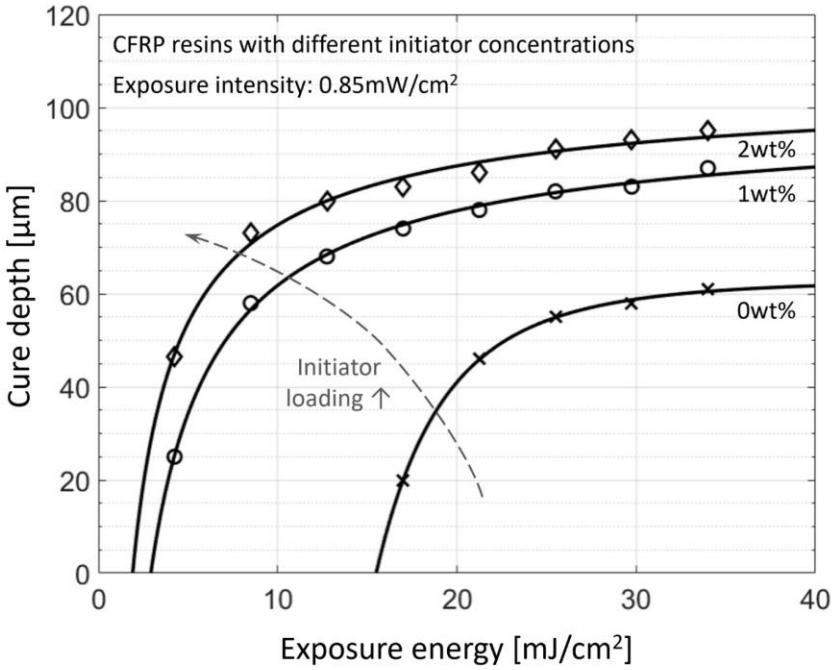

Figure 3-5 Cure depth as a function of energy density for CFRP resin with different initiator concentrations. The CFRP resins are composed of Formlabs 10k resin and 15 wt% short carbon fibers (average length of 70 µm).

3.3.3 The effect of fiber lengths on cure depth

In addition to the fiber weight fraction, fiber length is crucial for the mechanical properties of a CFRP composite. In order to determine their influence on the curing behavior, we compared two types of fibers. The evaluation of the fiber length distribution with their relative frequency is shown in Fig. 3-6. A minimum of 350 fibers for each fiber class was used for examination in Fiji. By using the same fiber weight fraction, the two types of fiber differ in terms of the total number of fibers.

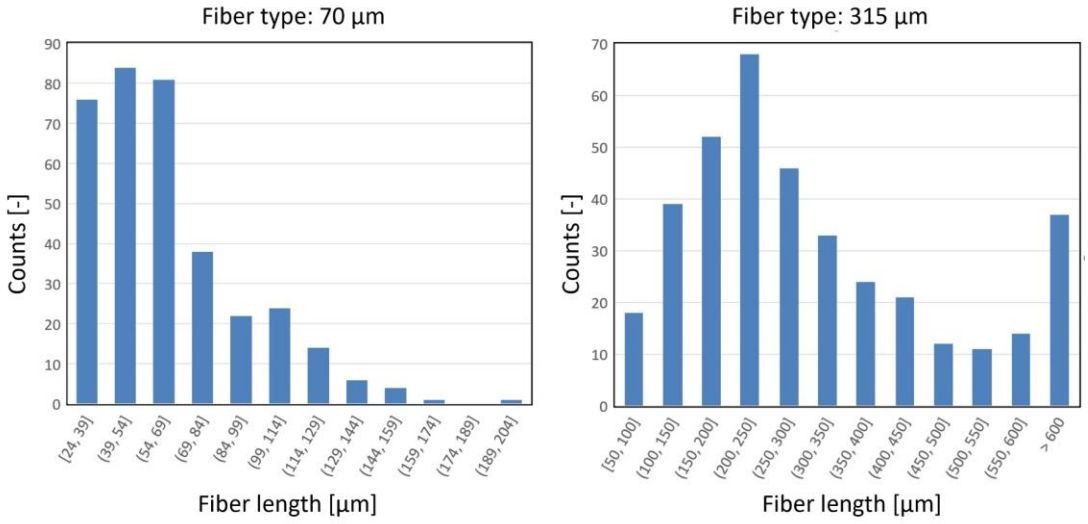

Figure 3-6 Measured fiber length distribution histogram of two types of carbon fibers.

In Fig. 3-7, it is found that the resin loaded with 70 μm fibers is harder to be cured than 315 μm resin. This is consistent with the results obtained by Badev et al. [53], who found a lower degree of polymerization can be triggered due to increased scattering with an increased number of particles. This is reasonable because the amount of fibers inside 70 μm resin is more, causing more scattering and less polymerization. Such a phenomenon can also be found in ceramic/magnetic particle-loaded resin printing. Schlotthauer et al. [54]. found that the variation of the cure depth follows a linear law with the mean diameter of particles: the larger the particle size (from 0.6 μm to 4.4 μm), the larger the cure depth.

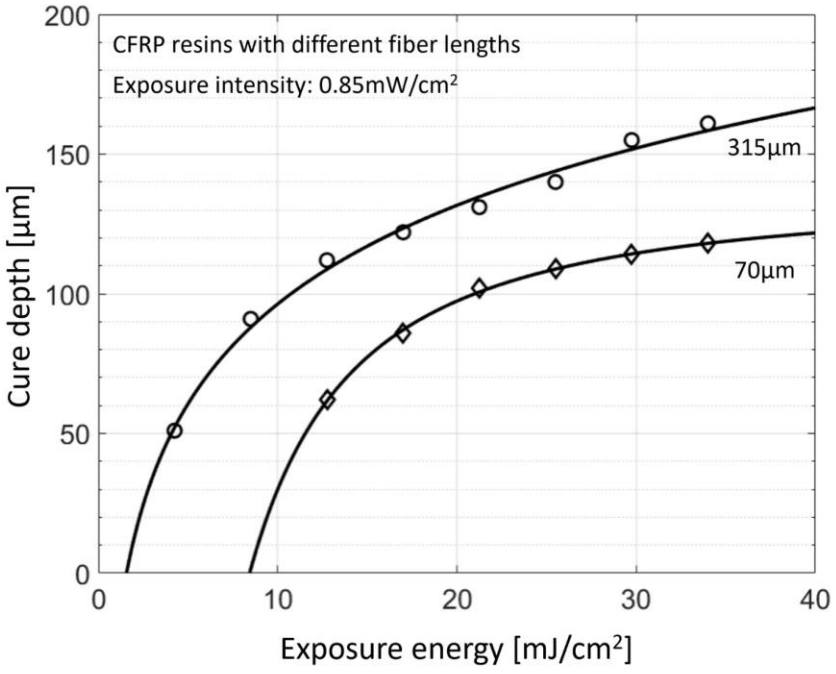

Figure 3-7 Cure depth as a function of energy density for CFRP resin with different fiber lengths. The CFRP resins comprise Formlabs 10k resin and 5 wt% carbon fibers.

3.4 Rheology and processability study

As mentioned in chapter 2, there are two configurations for the PSL process: top-down and bottom-up. For the bottom-up approach, the UV light projects from beneath to a vat with a transparent bottom to solidify resin onto the printing stage (Fig. 3-8a). After curing, the stage elevates to allow for the replenishment of new resin. A separation interface made of non-stick materials like polydimethylsiloxane (PDMS) and FEP (Fluorinated ethylene propylene) is used to help with separation [55]. Such a process is called the "recoating process", which is highly related to the resin viscosity. For both configurations, thin resins are always desired because they can be recoated via its gravity, while viscous resin usually is hard to be recoated efficiently. Although the bottom-up approach is less demanding on resin viscosity than the top-down method, it still requires the resin to settle down in a reasonable time. Therefore, it is necessary to study the rheology of the CFRP to understand the printing process and further expand the range of printable materials.

We measured the viscosity of CFRP resins loaded with different fiber loadings (average fiber length of 70 μm), as shown in Fig. 3-8b. The pure matrix resin (0 wt% carbon fiber) exhibits a complex viscosity (η) of ~1.9 Pa·s that is almost independent of the shear rate. Such a resin can flow easily during the recoating process. When the fiber concentration increases, the viscosity increases, and the resin with 25 wt% carbon fibers becomes a shear-thinning fluid. The resulting resin has a high viscosity at low shear rates and a low viscosity at high shear rates, making it flow only upon pressure. In order to process such viscous resin, a tape-casting method can be applied, as discussed before. Such a method utilizes the resin's shear-thinning effect to recoat each layer efficiently.

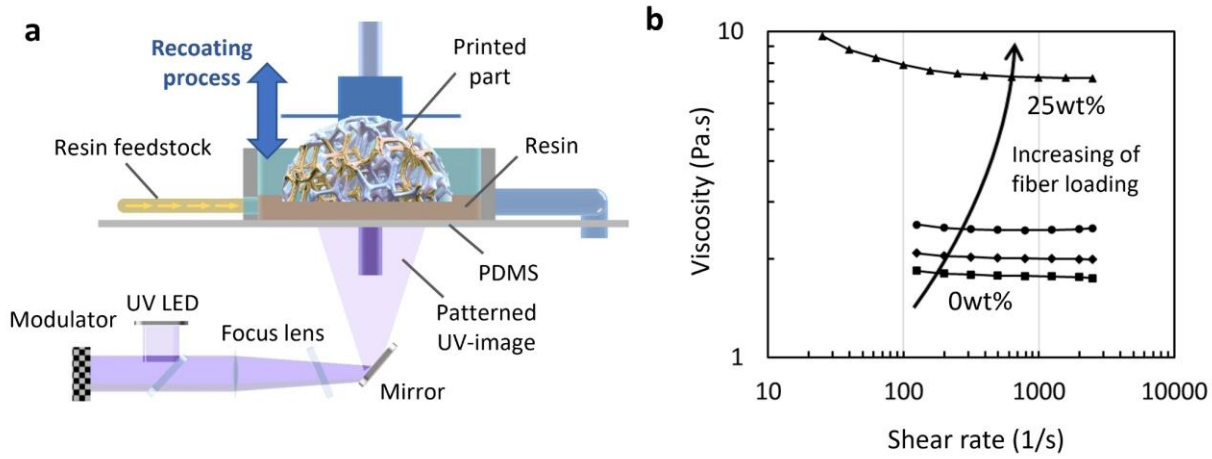

Figure 3-8 Schematic of bottom-up PSL configuration and CFRP resin's viscosity. (a) Schematic of a typical bottom-up PSL system. (b) Measured viscosity of CFRP resin with different fiber concentrations (0, 5, 10, 25 wt%) under different shear rates.

Alternatively, heating could also reduce the viscosity. We successfully designed and built a heating system to be integrated with the printing system. The heating element can be heated up to 130℃, which then heats the resin to over 90℃ in minutes. Through the experiment, we observed that the viscosity of resin decreases upon heating, and this decrease in viscosity greatly facilitated the recoating process.

Another solution is adding a diluter to the matrix material to reduce viscosity directly. A polymer, PEGDA (polyethylene glycol diacrylate), which has a viscosity of ~ 0.025 Pa · s at room temperature, can be used as the diluter. It was found that adding 25 wt% PEGDA can significantly reduce the resin's viscosity, enabling an easier recoating process. PEDGA was selected both for its low viscosity and its good mechanical performance. For the final printed part with a diluted

resin, we observed a slight drop in its Young's Modulus compared with resin without diluter, and the Modulus/Viscosity can be further tuned by changing the ratio of the diluter.

3.5 Mechanical property of bulk CFRP composite

3.5.1 Mechanical testing methods

To determine the tensile mechanical properties of the 3D printed samples, ASTM standard tensile test samples were fabricated and tested. The tensile tests were done on an Instron 5944 equipped with Bluehill data acquisition software and a 2000N load cell. Unidirectional tensile tests were performed to evaluate the stress-strain curve of the unit cell and determine Young's modulus. A strain rate of $10^{-3}/s$ was employed on each sample until fracture. Several samples per volume fraction were tested to determine the modulus. The ASTM standard used for the test was ASTM designation – D3039 (Standard Test Method for Tensile Properties of Polymer Matrix Composite Materials). Similarly, compression tests were performed using samples complying with ASTM designation – E198 (Standard Test Method of Static Tests of Lumber in Structural Sizes, Section 13). The above standard was obtained from ASTM designation – E2954 (Standard Test Method for Axial Compression Test of Reinforced Plastic and Polymer Matrix Composite Vertical Members) for short structures. Shear tests were performed using cylindrical samples of 0.5 inch diameter and 2 inches length.

3.5.2 Mechanical property measurement

We tested several samples composing different volume fractions of carbon fibers: namely, 0 vol% (i.e., pure Formlabs Rigid resin), 5 vol%, and 10 vol% CFRP. All samples were tested in the

transverse direction with respect to the print direction. This ensures that failure does not occur due to layer debonding and that the fibers are arranged axially to the printing direction. This treatment is critical because the properties of fiber-reinforced composites depend on the direction of the fibers. Since fiber-reinforced composites exhibit different behavior in tension and compression, the elastic modulus was tested separately for each loading condition.

Fig. 3-9 shows the test results for tensile, compressive, and shear modulus, respectively. The modulus is plotted against different volume fractions of carbon fibers loaded in the matrix resin. The red diamond in each plot represents the average value from the samples that were tested, and the error bars are positioned at one standard deviation. It is seen that the addition of carbon fibers to the matrix increased the modulus in all three cases. The tensile modulus of the pure matrix (without CF reinforcement) measured was slightly lower than the modulus claimed by Formlabs Inc. on their website. This can be attributed to the change in printing systems, printing parameters, and post-curing techniques. The tensile modulus increased linearly with an increase in CF loading.

The compressive modulus also increases linearly with an increase in fiber loading. However, the stiffness in this direction is lower than the tensile modulus measurements due to the anisotropy in fiber-reinforced composites. This is because fibers under compressive loading fail via buckling, making them less stiff. It is also seen that the error bars in all cases are close to the average value. This suggests that the stiffness in the compressive direction is less susceptible to 3D printing defects such as porosity and layer adhesion. These defects were particularly evident in the measurement of shear modulus tests. As the volume fraction increases, the shear modulus also

increases more or less linearly. However, these measurements were prone to large errors due to print quality.

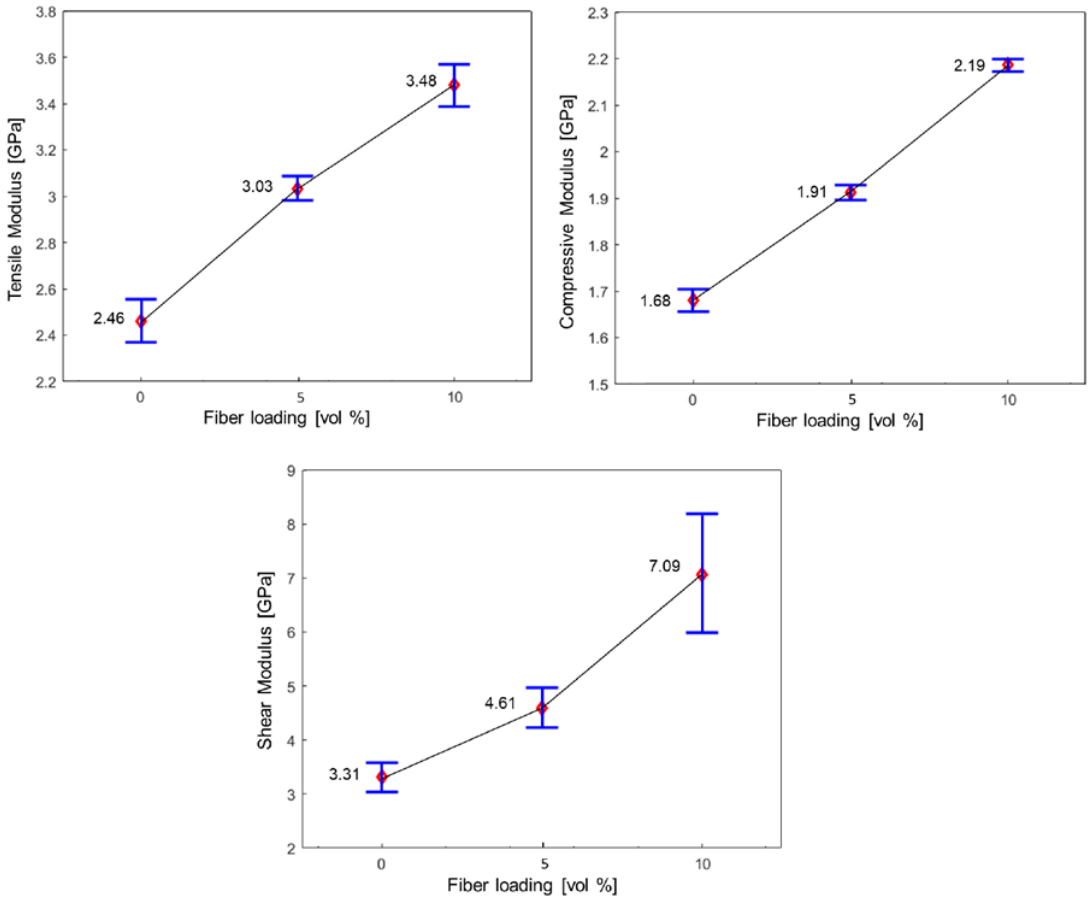

Figure 3-9 Tensile, compressive, and shear modulus of CFRP composites with different fiber loadings.

3.5.3 Theoretical analysis

It is seen that the stiffness in tensile, compressive, and shear directions increases linearly with an increase in fiber volume fraction. This, however, was only proved at low-volume fractions of carbon fiber. As the volume fraction increases, the print quality turns bad due to the difficulty in

the 3D printing of CFRP composites using PSL. As a result, the improvement in properties of 3D printed CFRP composite at high volume fractions cannot be guaranteed unless the PSL system is improved.

As shown in Fig. 3-10, when compared to the theoretical bounds as given by Eq. 3-1 and 3-2, the printed samples tested were close to the lower Reuss bound. This could be attributed to several factors. The upper Voigt bound assumes an ideal case of continuous fiber reinforcement in the sample, perfect alignment, and perfect fiber-matrix adhesion. This is not the case in the samples tested. The fibers used for reinforcement are short and discontinuous. Despite the use of a tape casting recoating technique, it is not possible to achieve perfect fiber alignment. Also, since the fibers are not treated, there is slippage between the fiber and matrix. All these factors result in the stiffness being closer to the lower bound. These factors also provide methods to improve the stiffness and reach closer to the upper bound. However, the results obtained show higher stiffness when compared to other studies using SLA and FDM techniques to 3D print CFRP composites [56, 57].

Theoretical bounds:

$$E_{upper} = fE_{CF} + (1 - f)E_{matrix} \qquad \text{(Eq. 3-1)}$$

$$E_{lower} = \frac{E_{CF}\,E_{matrix}}{fE_{matrix} + (1-f)E_{CF}} \qquad \text{(Eq. 3-2)}$$

Where, E_{CF} = Young's modulus of carbon fiber

E_{matrix} = Young's modulus of the matrix

f = volume fraction of carbon fiber

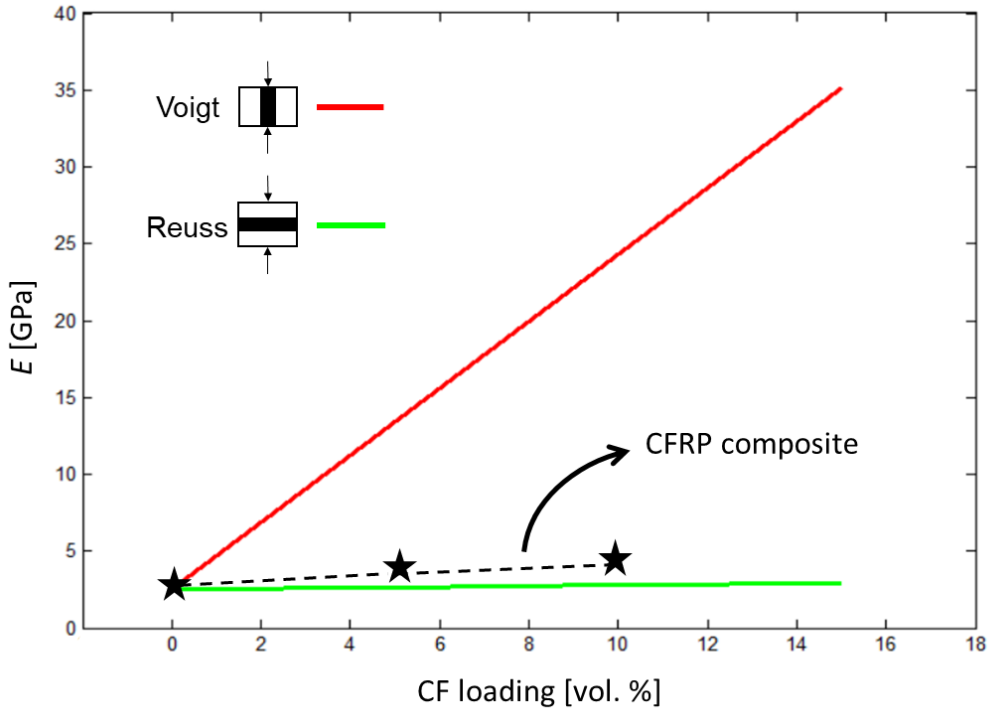

Figure 3-10 Comparison of the tensile modulus test results with theoretical bounds.

3.6 Mechanical property of octet-truss based CFRP lattices

The above tests show that the addition of carbon fibers improves the base material's mechanical properties a lot, then we extend the work to a class of lightweight, high-stiffness lattice topologies [58, 59]. Here, we developed lightweight CFRP microlattices consisting of periodically arrayed octet-truss unit cells. The octet-truss topology was chosen as a repeating unit cell in the microlattices because its deformation mechanism is stretching-dominated, which gives rise to a favorable stiffness-to-weight ratio compared to stochastic bending-dominated cells [46, 58, 59]. The relative density of the microlattice, $\bar{\rho}$, is approximated by $\bar{\rho} = 6\pi\sqrt{2}(r/l)^2$, where r is the

strut radius and l is the strut length [59, 60]. The microlattice's density equals the product of its relative density and the base material's density.

To investigate the mechanical performance of the present microlattice, unit cells having a range of relative densities ($\bar{\rho}$ ~ 4 % to 30 %) with a side length of 15 mm were fabricated using the PμSL system. The inset picture in Fig. 3-11 shows an octet-truss unit cell sample having $\bar{\rho}$ = 4 %. The density of the bulk CFRP composite after curing is 1230 kg/m^3. Therefore, the unit cell sample ($\bar{\rho}$ = 4 %) has a density of 49.2 kg/m^3. The modulus is plotted against the density of the microlattice, where the diamond means the average value based on several testing results, and the red line is the scaling power.

The effective stiffness E of the octet microlattice is related to the virgin base materials by E = (1/9) $\bar{\rho}E_b$, where E_b is the stiffness of the base material and $\bar{\rho}$ is the relative density of the octet-truss structure [59, 60]. For example, the CFRP base material has a measured stiffness of 2.71 GPa; our 12% octet lattice has a measured stiffness of 32.2 MPa (compared to the theoretical 36.2 MPa).

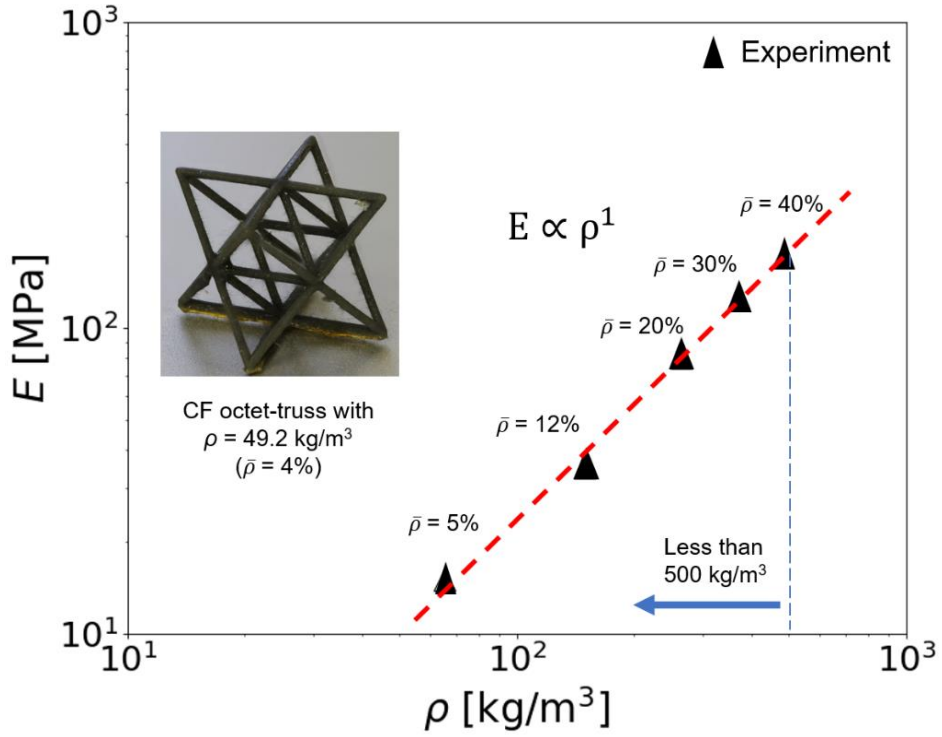

Figure 3-11 Testing results of CFRP octet-truss lattice material with different relative densities.

During the compression tests, we observed obvious buckling behavior before fracture for a unit cell having $\bar{\rho}$ = 4 %. As shown in Fig. 3-12, there was an extended plateau area after the stress reached its maximum value. Therefore, the failure mode for the ultra-low-density octet-truss samples (relative density < ~5%) is the buckling failure of the constituent struts. On the other hand, such buckling behavior diminishes when the relative density rises over ~10%. In the normalized stress-strain plot, the slope of the sample with $\bar{\rho}$ = 12 % is always positive. The sample experiences a brittle-like failure mode.

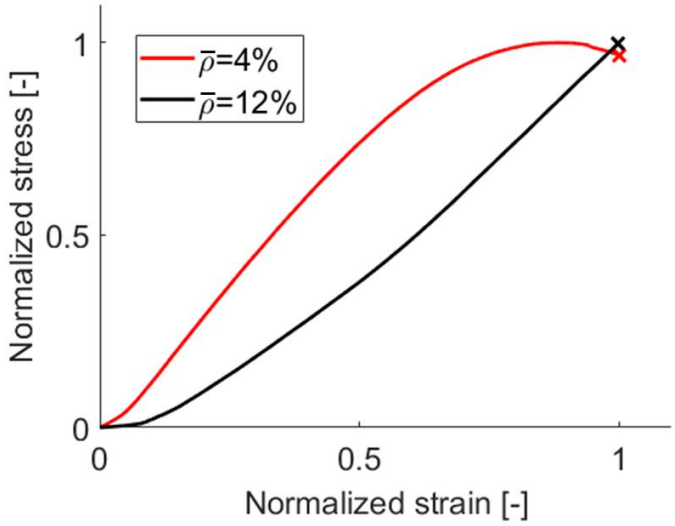

Figure 3-12 Normalized stress-strain curve for the octet-truss lattice with a relative density of 4% and 12% (The cross symbols represent the fracture points).

3.7 Size effect of CFRP lattices

3.7.1 Introduction

The unit cell design approach is often employed in the design of 3D non-stochastic cellular structures [58, 59], and idealized boundary conditions are often assumed to simplify analysis. Simplifying cellular structures can significantly reduce the computational costs of modeling and analyzing them. However, this can result in various deviations from reality [61, 62]. The effective material properties of cellular materials are typically obtained by testing samples where the global sample size is considerably larger than the local unit cell size [63]. However, when the size of the sample approaches the scale of structural features (i.e., a unit cell) within a material, such material

properties experience a size effect. Literature on size effect studies for various cellular structures has been reported based on experiments and modeling [64, 65].

In the previous sections, the author presented an extendable multi-material projection micro-stereolithography process capable of producing cellular materials reinforced by short fibers. The microlattices presented, however, are limited by the printing area of the designed PμSL system as they are unit cells. Cellular structures that contain various unit cells along each design direction are more valuable for practical applications. Therefore, it will be beneficial to study the size effect of the presented lattices so that we can learn more about the mechanical properties of the lattices and extend the study from the unit cell to cellular structures.

3.7.2 Size effect study based on TMPTA lattices

To study the size effect caused by boundary condition and topology in detail, we first considered two stretch-dominated topologies: namely, iso-truss and reinforced square unit cells (Fig. 3-13). The rationale of this study is that the size effect is expected to be independent of the base material properties and to reveal similar relationships with the effective material properties across other stretch-dominated latticed structures, such as an octet-truss lattice which will be discussed later. By keeping the relative density (ρ/ρ_s = 10 %) and the overall volume ($V_{\text{lattice}} = 40^3$ mm^3) constant, lattices with different numbers of cells were additively manufactured. The number of cells per side N_{cell} varied from 1 to 5 for the iso-truss lattices and from 1 to 4 for the reinforced square lattices (Fig. 3-13a and Fig. 3-13f). The base material for these samples was TMPTA (Trimethylolpropane triacrylate), which is relatively easy to fabricate as compared to using CFRP due to its lower viscosity and effortless curing conditions.

The following results were measured from compressive stress-strain curves of the iso-truss and reinforced square lattices, respectively, as shown in Fig. 3-13c and Fig. 3-13h. In these figures, the curves start from zero strain to a strain in which any fracture occurs. Fig. 3-13(d-e, i-j) show the effective elastic modulus and yield strength as a function of N_{cell}, which are averaged values over the 3 repeats of each size with standard deviation indicated by error bars. For both topologies, the effective elastic modulus decreases with N_{cell} (generally $N_{cell} > 2$), and a similar trend is also seen in the effective yield strength. This indicates a softening size effect in which samples comprising smaller unit cells are softer than those with larger ones. This softening size effect can be explained by the fact that stress distributions are concentrated differently near free and loaded edges for different sample sizes. The cells adjacent to these edges most likely carry more stress than those on the interior due to the stress concentration, and samples with a high N_{cell} (i.e., small unit cells) have lower theoretical peak stress than its counterpart, leading to lower values of properties. Material arrangements, defined by a strut orientation within a material, also contribute to different stress distributions for different topologies; however, this does not affect a general trend of the softening size effect.

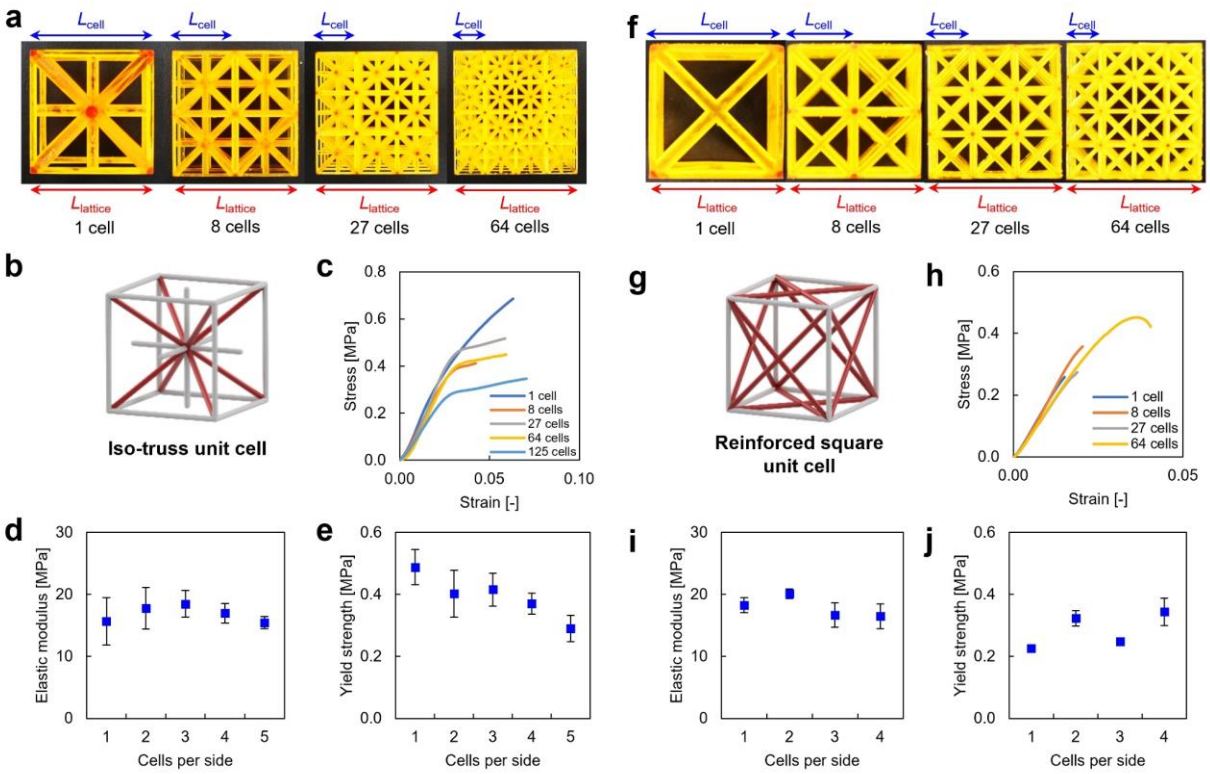

Figure 3-13 Size effect study on TMPTA lattices. (a) Iso-truss samples made of TMPTA. (b) 3D representation of iso-truss unit cell. (c) Compressive stress-strain curves of iso-truss samples with different numbers of cells. (d-e) The effective elastic modulus and yield strength of iso-truss samples with different sizes. (f) Reinforced square samples made of TMPTA. (g) 3D representation of reinforced square unit cell. (h) Compressive stress-strain curves of reinforced square samples with different numbers of cells. (i-j) The effective elastic modulus and yield strength of reinforced square samples with different sizes.

In addition, two distinct failure modes depending upon N_{cell} were observed for both topologies with a fixed relative density. For example, an iso-truss sample having N_{cell} of 1 clearly shows brittle-like failure; fracture is seen near a center node, and the corresponding stress-strain behavior reveals very little or no plastic deformation. On the other hand, similar samples made of N_{cell} equal to 2 or greater experience buckling failure of the constituent struts. A similar observation was seen

in reinforced square lattice samples, but the brittle-like failure persists with a higher N_{cell} as compared to that of the iso-truss samples. This implies that the size effect can lead to different failure modes due to different stress distributions within the material domain.

3.7.3 Size effect study based on CFRP lattices

To discover the material independency of the softening size effect, we investigated the effective material properties of octet-truss lattice structures with different numbers of cells made of CFRP, as shown in Fig. 3-14a. The relative density ρ/ρ_s of all samples was 10 %, which is approximated via $\rho/\rho_s = 6\pi\sqrt{2}(r/l)^2$, where r is the strut radius and l is the strut length [59, 60]. Samples with different sizes were realized by acquiring various N_{cell} ranging from 2 to 5, and the overall volume was 32^3 mm^3. The same compression tests described earlier were used to compute the effective material properties from compressive stress-strain curves shown in Fig. 3-14b. Similar to the two topologies studied earlier, both effective elastic modulus and yield strength display the softening size effect with an increase in N_{cell} (Fig. 3-14c and 3-14d). In addition, all samples showed brittle-like failure regardless of size.

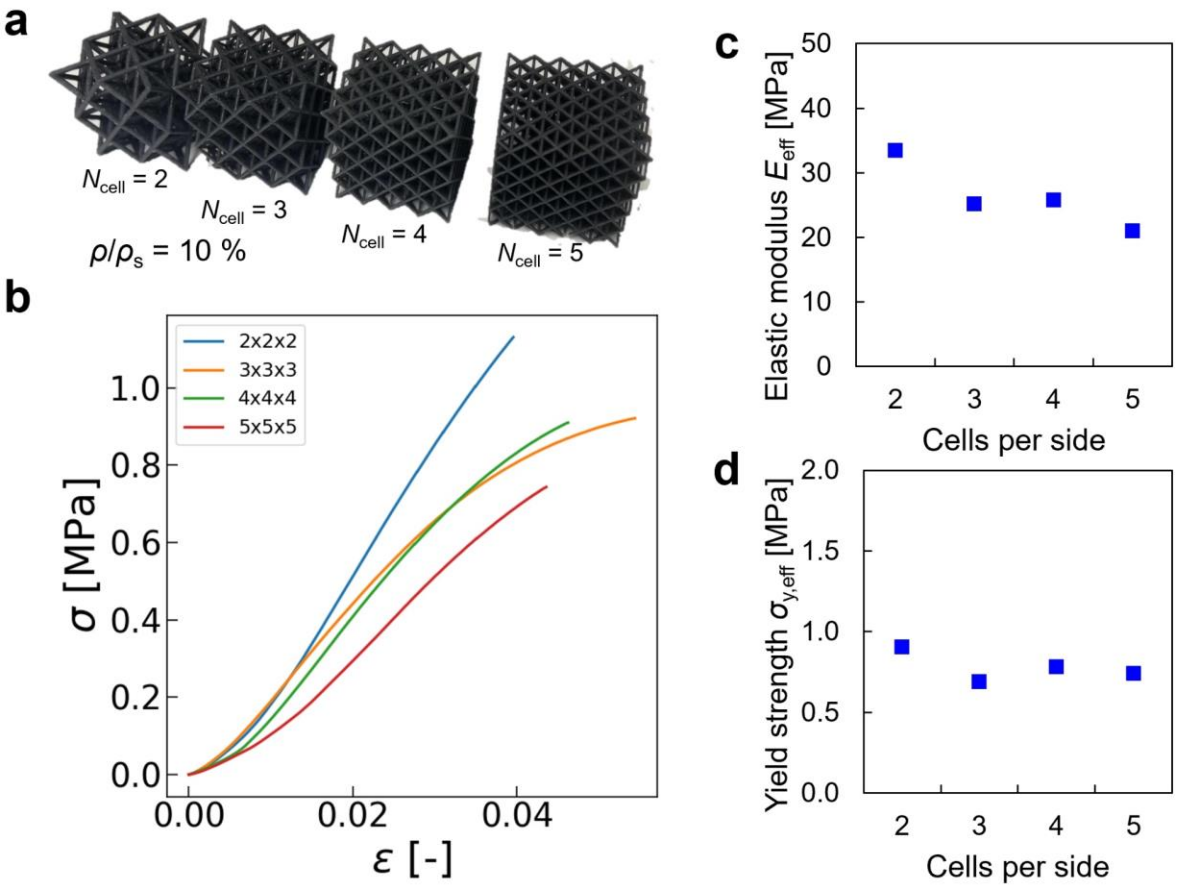

Figure 3-14 Size effect of octet-truss lattices made of CFRP composite. (a) Octet-truss samples with different numbers of cells made of CFRP. (b) Compressive stress-strain curves of samples with different sizes. (c-d) Effective elastic modulus and yield strength of octet-truss samples as a function of the number of cells per side.

3.7.4 Comparison and conclusion

To have a better understanding of the material independence regarding the softening size effect, the effective material properties of the iso-truss (made of TMPTA) and octet-truss samples (made of CFRP) were normalized by the corresponding base material properties and were fitted with a power-law function, as illustrated in Fig. 3-15. As expected, a similar trend is seen for both material

properties regardless of different base materials. Deviations in the magnitude of these normalized properties are most likely caused by different topologies (i.e., different strut arrangements).

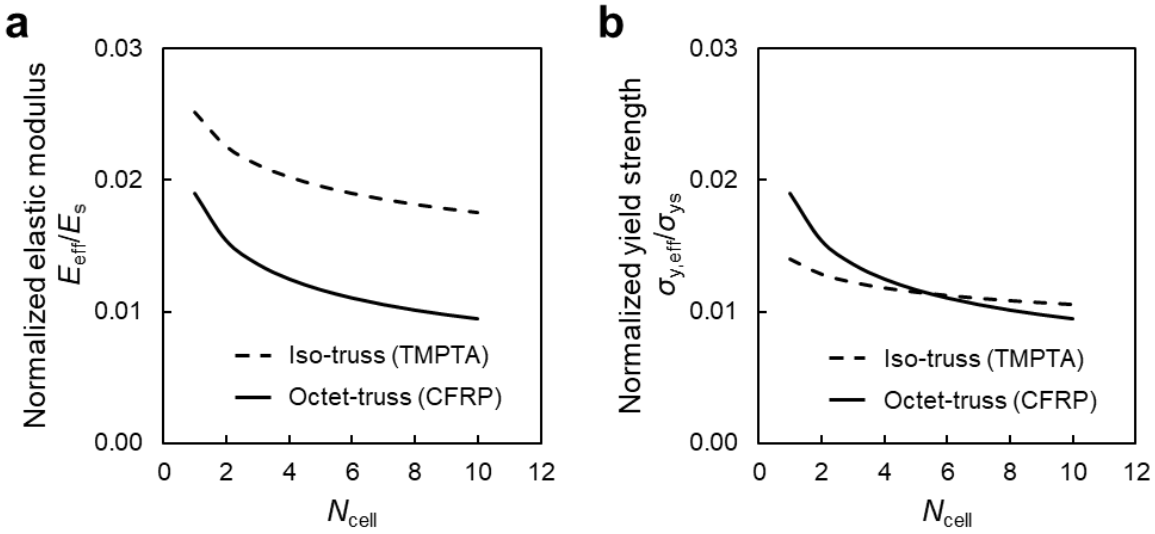

Figure 3-15 Power-law fitted normalized material properties of iso-truss samples (made of TMPTA) and octet-truss samples (made of CFRP).

In this section, using the PSL system, we fabricated cellular materials consisting of various types of unit cells. Several stretch-dominated lattices made of two different polymer-based resins (i.e., TMPTA and CFRP) showed a generalized trend on the softening size effect of stretch-dominated cellular structures, which indicates that this size effect is independent of base materials. While the failure mode of the lattices at a fixed relative density is influenced by the size effect due to boundary condition-induced localized stress concentrations, cellular topology (or material arrangement within a material) shows negligible effects on the softening trend in the normalized properties.

3.8 Development of two-phase lightweight, stiff, and high-damping carbon fiber reinforced polymer microlattices

3.8.1 Theory and hypothesis

Despite brittleness from the nature of stiff CFRP composites, it is promising that a two-phase composite layout incorporating the CFRP composites with a soft phase can lead to high stiffness-loss efficiency. To determine the effects of the soft phase on the bulk CFRP stiffness-damping properties, we performed an analytical study of several representative two-phase layouts by varying volume fraction of the soft phase and computed their effective stiffness (equivalent to storage modulus, E) and loss tangent based on two-phase composite theory [66, 67]. Fig. 3-16a illustrates the E-tanδ relationship of the different layouts; the percentage in this figure corresponds to the volume fraction of phase 1. Layouts considered here included Reuss and Voigt composites, Hashin-Shtrickman composites, stiff fibers in a soft matrix, and soft spheres in a stiff matrix. Here, phase 1 (stiff phase) was the CFRP composite (5 vol% fiber loading), and phase 2 (soft phase) was a soft elastomer. Our calculations show that a small volume fraction of phase 2 in the Reuss composite led to a substantial increase in loss tangent with a reasonable reduction in stiffness. Conversely, the Voigt composite required a substantial addition of phase 2 to achieve an appreciable increase in loss tangent. The upper and lower bounds of Hashin-Shtrickman composites were bounded by those of the Voigt and Reuss composites, respectively, and the stiff fibers- and soft spheres- inclusion composites behaved similarly to the Voigt composite.

Since the Reuss and Voigt layouts represented the upper and lower bounds in the stiffness-loss relationship in our study, we assessed these two layouts to identify the volume fraction of phase 2

that maximizes damping performance in terms of the damping figure of merit (*FOM*), $E^{1/3}\tan\delta/\rho$. This material index is intended for the plate- or panel-shaped applications for energy absorption, and it expresses how fast a clamped plate subject to forced vibrations reaches rest when the forcing term is removed, applicable to applications of lattice materials for damping management [68-71]. The lightest material for the plate or panel application is that with the highest value of $E^{1/3}/\rho$ [69, 72]. As depicted in Fig. 3-16b, the Reuss layout having a volume fraction of phase 2 equal to approximately 0.9 % was found to exhibit a maximal figure of merit. Therefore, the Reuss layout is a pertinent framework for designing a structure with high stiffness-damping efficiency.

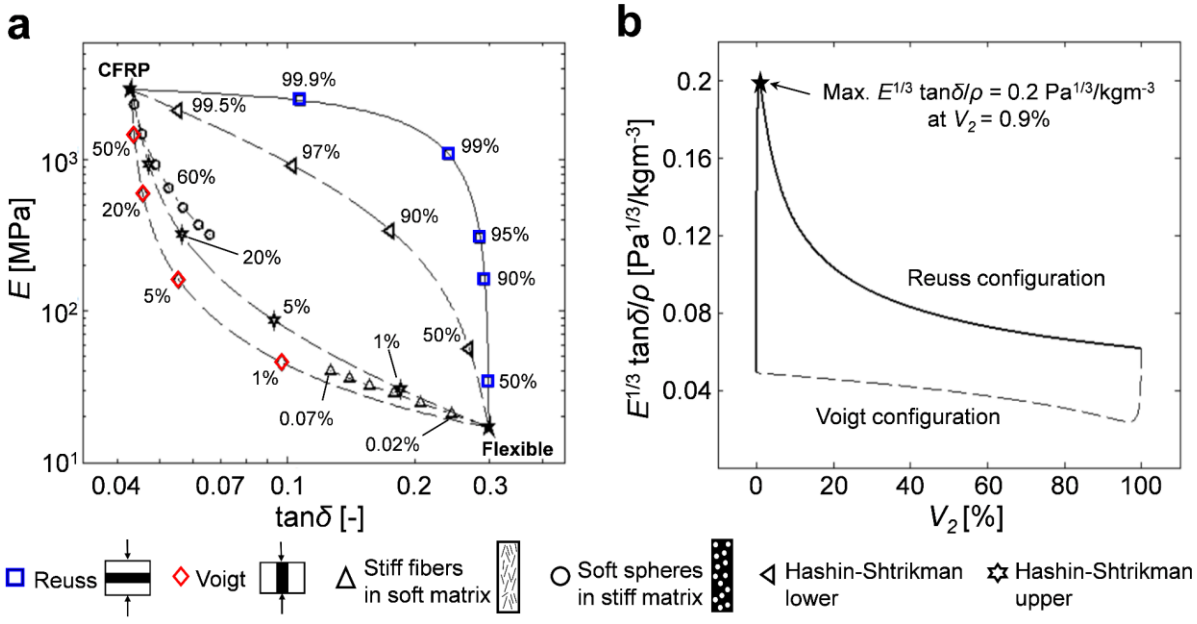

Figure 3-16 The effect of soft phase on the bulk CFRP stiffness-damping properties. (a) Stiffness (E) vs. loss tangent ($\tan\delta$) for various two-phase configurations incorporating CFRP and soft phase of bulk material. The percentage shown here corresponds to the volume fraction of the stiff phase (V_1). Graphical legends are provided at the bottom of this figure. (b) $E^{1/3}\tan\delta/\rho$ versus the volume fraction of the soft phase (V_2). This index has its maximum at $V_2 = 0.9$ %.

3.8.2 Design and production of two-phase CFRP microlattices

The above rationales provide conceptual design guidelines to optimize the stiffness-damping efficiency for two-phase bulk composites; then, we extend these principles to a class of lightweight, high-stiffness lattice topologies [58, 59]. Here, we developed lightweight CFRP microlattices consisting of periodically arrayed octet-truss unit cells in which the soft phase is embedded in selected out-of-plane struts, as shown in Fig. 3-17a. The octet-truss topology was chosen as a repeating unit cell in the microlattices because its deformation mechanism is stretching-dominated, which gives rise to a favorable stiffness-to-weight ratio compared to stochastic bending-dominated cells [46, 58, 59]. The soft phase was then intentionally inserted at the center of the selected struts to increase the maximum global strain, which in turn enlarges the area of the stress-strain hysteresis loop, leading to an improved energy absorption performance.

The soft phase ratio in the octet-truss unit cell, V_{soft}, defined as the ratio of h to H, controls the volumetric material distribution between the CFRP and the soft phase, which tailors the stiffness-damping property of the microlattices. Here, $V_{\text{soft}}^{\text{lattice}} = (2/3)V_{\text{soft}}$, where $V_{\text{soft}}^{\text{lattice}}$ is the ratio of overall soft phase volume to microlattices' volume (i.e., the volume fraction of soft phase) since the Reuss layout presents only in the selected out-of-plane struts.

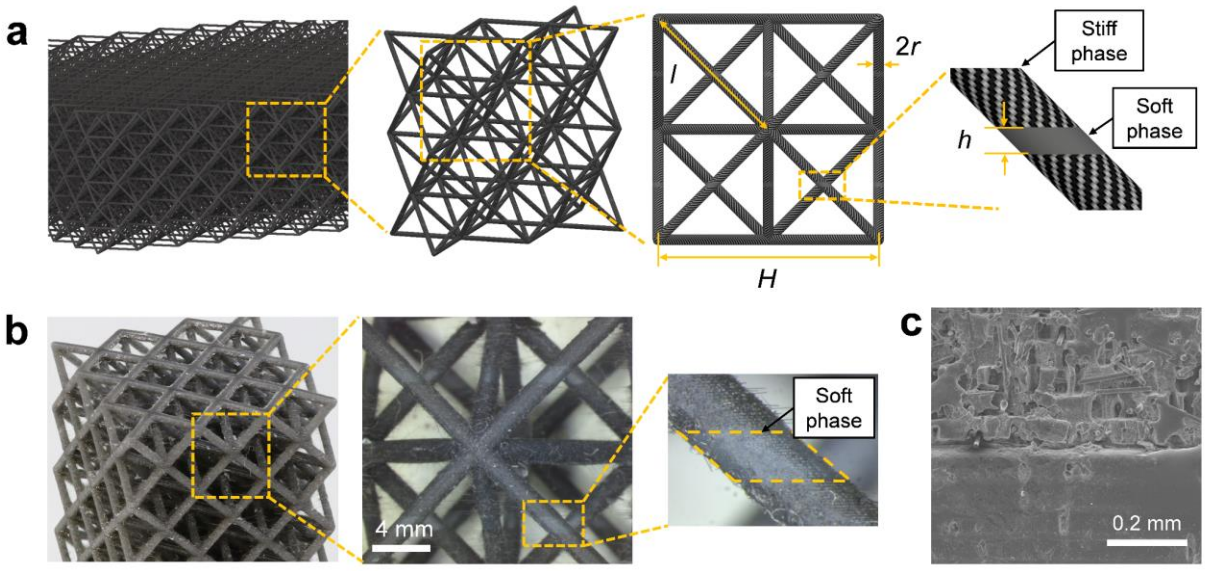

Figure 3-17 Octet-truss lattices made of soft and stiff materials. (a) Design of lightweight, stiff, high-damping microlattice with two-phase materials incorporating CFRP and soft phase. (b) Fabricated lightweight cellular CFRP microlattice having $\bar{\rho}$ = 7 % with V_{soft} = 9 %. (c) SEM image showing the interface between the two phases, where the top section is CFRP, and the bottom section is the soft phase.

To investigate the damping performance of the present microlattices, unit cells (3 for each density group) having a range of relative densities ($\bar{\rho}$ ~ 4 %, 7 %, 12 %) and soft phase ratios (V_{soft} ~ 0 %, 5 %, 9 %, 13 %, 20 %) with a side length of 15mm were fabricated using the multi-material PμSL system. Fig. 3-17b depicts an as-fabricated 3×3×3 lattice sample having $\bar{\rho}$ = 7 % with V_{soft} = 9 % as an example. The interface between the soft and stiff phases is covalently bonded after radical photopolymerizations and was experimentally confirmed to be adequately strong to transfer tensile and compression loads to adjacent layers. As shown in Fig. 3-17c, a scanning electron microscope (SEM) image was taken at the interface of the CFRP and soft phase.

3.8.3 Experimental setup and bulk material properties

The damping capacity of a material is often defined as loss tangent (tanδ). In the field of viscoelasticity, δ is called the phase (or loss) angle (or shift) between stress and strain sinusoidal responses and is a measure of the loss angle of a linearly viscoelastic material. This angle also represents the width of the elliptic Lissajous figure [66]. The procedure to determine the tanδ of the bulk sample is as follows. First, a compression or tension film clamp was used to load the sample onto a DMA apparatus (TA Instruments DMA 850). A nitrogen tank attached to the DMA test frame was used to regulate the temperature. Once the desired temperature (25° in Celsius) was reached, a strain sweep was carried out from 0.01 % strain to 10 % strain at a frequency of 1 Hz to determine the maximum strain within the elastic region for the sample (per ASTM D5026). This method is destructive because the sample must enter its plastic region as the strain increases and becomes permanently deformed. Thus, this plastically deformed sample was replaced with a new sample. The new sample was loaded with a frequency sweep from 0.1 Hz to 20 Hz to measure its tanδ. Within this range, the results at 0.1 Hz were adopted because the corresponding tanδ allows for a direct comparison with structural damping property obtained from the quasi-static cyclic compression tests since the frequency of such tests is in general below 0.1 Hz [68]. The fiber loading of all tested samples is 5 vol%. The measured material property is listed in Table 3-1.

Table 3-1 CFRP and flexible bulk material properties

Material	Storage modulus [MPa]	Loss modulus [MPa]	tanδ [-]
CFRP	2717.6	184.7	0.068
Flexible	7.4	2.2	0.299

We measured 3 samples at each point and took the average of a data set. Error bars in the stiffness and damping figures refer to the standard deviation, which is calculated by the equation $s = \sqrt{\frac{\sum_{i=1}^{n}(x-\bar{x})^2}{n-1}}$. The standard deviation of the *FOM*, $\frac{E^{1/3}\tan\delta}{\rho}$, is calculated by the error propagation equation, $s_{FOM} = \sqrt{\frac{1}{9}\,(s_s)^2 + (s_d)^2}$, where s_s and s_d are the standard deviation of stiffness and damping. The test data after averaging and curve fitting are provided below.

Storage modulus and intrinsic damping of samples, representing the lightweight CFRP cellular microlattices with a relative density of 7 %, are provided in Table 3-2. We performed the curve fit on these measured mechanical properties using $E = a\cdot\exp(b\cdot V_{soft}) + c\cdot\exp(d\cdot V_{soft})$ and $\tan\delta = a\cdot\exp(b\cdot V_{soft}) + c$ to see their trends and the coefficients of the curve fits are listed in Table 3-3.

Table 3-2 Testing data of the samples with a relative density of 7 % at small strains

V_{soft}	0%	3%	5%	9%	11%	13%	20%
Storage modulus [MPa]	27.060	13.112	9.323	6.130	5.320	4.108	2.659
tanδ [-]	0.076	0.141	0.183	0.267	0.279	0.304	0.318
$SD_{storage\_modulus}$ [MPa]	1.218	0.577	0.438	0.294	0.208	0.337	0.242
$SD_{\tan\delta}$ [-]	0.009	0.017	0.023	0.028	0.023	0.019	0.021

Table 3-3 The coefficients of fitting equations of 7 % relative density samples

Coefficients	*a*	*b*	*c*	*d*	R^2
Storage modulus [MPa]	18.43	-38.22	8.62	-5.36	0.9989
tanδ [-]	-0.27	15.37	0.33	n/a	0.9711

Stiffness and loss coefficients of the samples at large strains are listed in Table 3-4 and Table 3-5. These measured properties were curve fitted via $E = a \cdot \exp(b \cdot V_{soft}) + c \cdot \exp(d \cdot V_{soft})$ and $\tan\delta = a \cdot \exp(b \cdot V_{soft}) + c$. The coefficients of the curve fits are provided in Table 3-6 and Table 3-7.

Table 3-4 Stiffness and corresponding standard deviation (*SD*) in [MPa]

$\overline{\rho}$ \ V_{soft}	0%	5%	9%	13%	20%
4%	17.725	6.720	4.510	3.012	1.988
7%	26.597	8.969	5.510	4.004	2.337
12%	32.213	11.250	6.250	4.440	2.740
$SD_{4\%}$	0.798	0.229	0.239	0.069	0.131
$SD_{7\%}$	1.011	0.413	0.314	0.092	0.096
$SD_{12\%}$	1.546	0.315	0.219	0.120	0.090

Table 3-5 Structural loss coefficients and corresponding standard deviation (*SD*) [-]

$\overline{\rho}$ \ V_{soft}	0%	5%	9%	13%	20%
4%	0.305	0.479	0.558	0.611	0.679
7%	0.207	0.415	0.468	0.527	0.614
12%	0.142	0.260	0.310	0.419	0.453
$SD_{4\%}$	0.015	0.016	0.018	0.020	0.014
$SD_{7\%}$	0.014	0.009	0.014	0.012	0.015
$SD_{12\%}$	0.011	0.017	0.009	0.011	0.016

Table 3-6 The coefficients of fitting equations of modulus of samples

$\overline{\rho}$ \ Coefficients	*a*	*b*	*c*	*d*	R^2
4%	13.84	-27.14	3.86	-2.93	0.9992
7%	20.58	-31.89	6.00	-4.07	0.9987
12%	26.37	-28.28	5.84	-3.66	0.9999

Table 3-7 The coefficients of fitting equations of loss coefficient of samples

$\overline{\rho}$ \ Coefficients	a	b	c	R^2
4%	-0.27	10.71	0.46	0.9967
7%	-0.29	10.06	0.42	0.9880
12%	-0.23	10.75	0.31	0.9889

3.8.4 Intrinsic damping at small strains

Fig. 3-18a and 3-18b show measured modulus and loss tangent of samples with a range of soft phase ratios obtained by DMA tests, as described above. Single relative density was considered here since the intrinsic damping is invariant with respect to the relative density [66], and this was verified by our analytical model. We observed that the effective modulus of the samples showed an exponential relationship as a function of V_{soft} via $E = a^*\exp(bV_{soft}) + c^*\exp(dV_{soft})$.

Conversely, intrinsic damping $\tan\delta$ is nonlinearly proportional to V_{soft} via $\tan\delta = a^*\exp(bV_{soft}) + c$. A trendline approaches an asymptotic value of the loss tangent to be approximately 0.32, which corresponds to the inherent loss tangent of the soft phase. Moreover, the loss tangent reaches its asymptotic value earlier than the modulus at a given change in V_{soft}. For example, the magnitude of the modulus at V_{soft} = 9 % is still a factor of approximately 2 larger than that at V_{soft} = 20 % (from 6.13 MPa to 2.66 MPa), whereas the magnitude of the loss tangent at V_{soft} = 20 % was approximately 1.2 times larger than that at V_{soft} = 9% (from 0.267 to 0.32). This result is consistent with the theoretical response of a bulk Reuss composite illustrated in Fig. 3-16a, which implies that the design rules for bulk composites can be applied to these two-phase lattice materials at small strains.

We further investigated the stiffness-damping performance of our designed microlattices by the damping figure of merit, defined as $E^{1/3}\tan\delta/\rho$ in the previous section. The figure of merit was calculated using the measured effective modulus and loss tangent values to identify the optimal soft phase percentage, as shown in Fig. 3-18 c. A solid line represents a curve fit of the damping figure of merit. The computed value reached its peak when V_{soft} was equal to approximately 10 %, which was a factor of 3 times larger than obtained from pure CFRP.

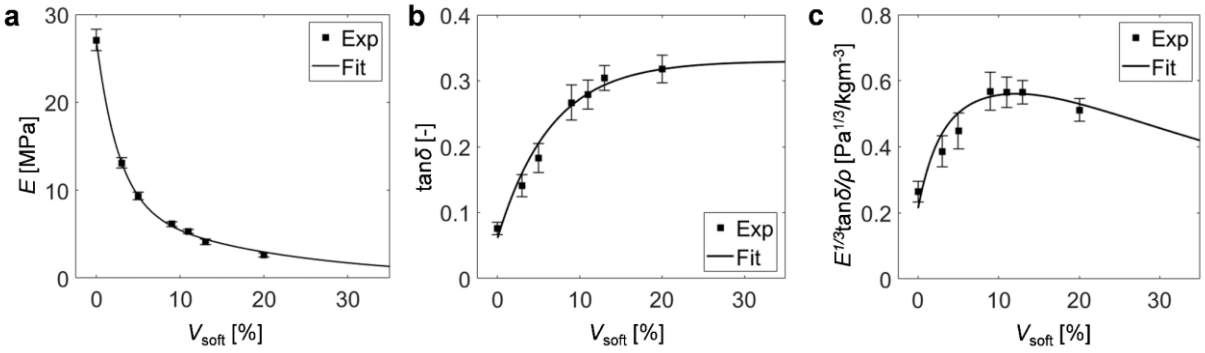

Figure 3-18 Intrinsic damping properties of the lightweight cellular CFRP microlattices having a relative density of 7 % with different soft phase ratios. The values were averaged over three test results, and error bars represent the standard deviation. Solid lines in these figures represent the curve fit. (a) The effective modulus (E) as a function of the soft phase ratio V_{soft}. (b) Loss tangent ($\tan\delta$) as a function of V_{soft}. (c) Damping figure of merit as a function of V_{soft}.

3.8.5 Structural damping at large strains

Stress-strain hysteresis loops of samples with $\bar{\rho}$ = 4% and $\bar{\rho}$ = 12% having V_{soft} = 20% in response to multicyclic compression (30 cycles) are shown in Fig. 3-19a and 3-19b, respectively. We observed that the hysteresis loops stabilized after the first three cycles, which implies the presence of non-recoverable mechanisms such as localized nodal fractures and possible inelastic deformation. The loss coefficient monotonically decays with cycle number, in which a reduction

of approximately 25% was seen after the first three cycles (see insets in these figures). In Fig. 3-19c, the evolution of the stress-strain hysteresis loop is presented over different relative densities ($\bar{\rho}$ = 4%, 7%, 12%) while holding V_{soft} constant (V_{soft} = 20 %). To adequately display this evolution, we normalized both the stress and strain of the loops with respect to their maximum values. Dominant deformation mechanism at a low relative density ($\bar{\rho}$ = 4 %) was elastic buckling of the constituent struts; however, this buckling response diminished with an increase in the relative density ($\bar{\rho}$ = 7 %), and plastic yielding mechanism started to dominate deformation at a higher relative density ($\bar{\rho}$ = 20 %). The variation in deformation mechanisms at different relative densities results in a difference in the shape of stress-strain hysteresis loops. This, in turn, leads to a change in the dissipated energy per cycle.

We observed that the measured modulus decreases monotonically with an increase in V_{soft}, and this relationship is nearly identical to one observed from intrinsic properties (Fig. 3-19d). This is because the modulus is a mechanical property that is invariant to the magnitude of global strains according to the nature of elasticity. Curve fits for the measured modulus were found to follow an exponential relationship of V_{soft} . Structural loss tangent of the microlattices, computed via $\tan\delta = 2\Psi/\pi$, is shown in Fig. 3-19e. The structural loss tangent increases monotonically with V_{soft} but decreases with relative density. Additionally, the loss tangent reaches its asymptotic value with an increase in V_{soft}, and this convergence is more rapid for samples with higher relative densities. Our finding implies that a cellular structure is preferable to a bulk material for structural damping. Structural damping figure of merit was calculated and plotted in Fig.3-19f. Results showed that the maximum figure of merit for different relative densities occurs at different V_{soft}. For example,

samples having $\bar{\rho}$ of 4 % and 7 % showed such peaks when V_{soft} ~ 6 %, whereas a peak for a sample having $\bar{\rho}$ of 12 % occurs when V_{soft} is equal to approximately 12 %.

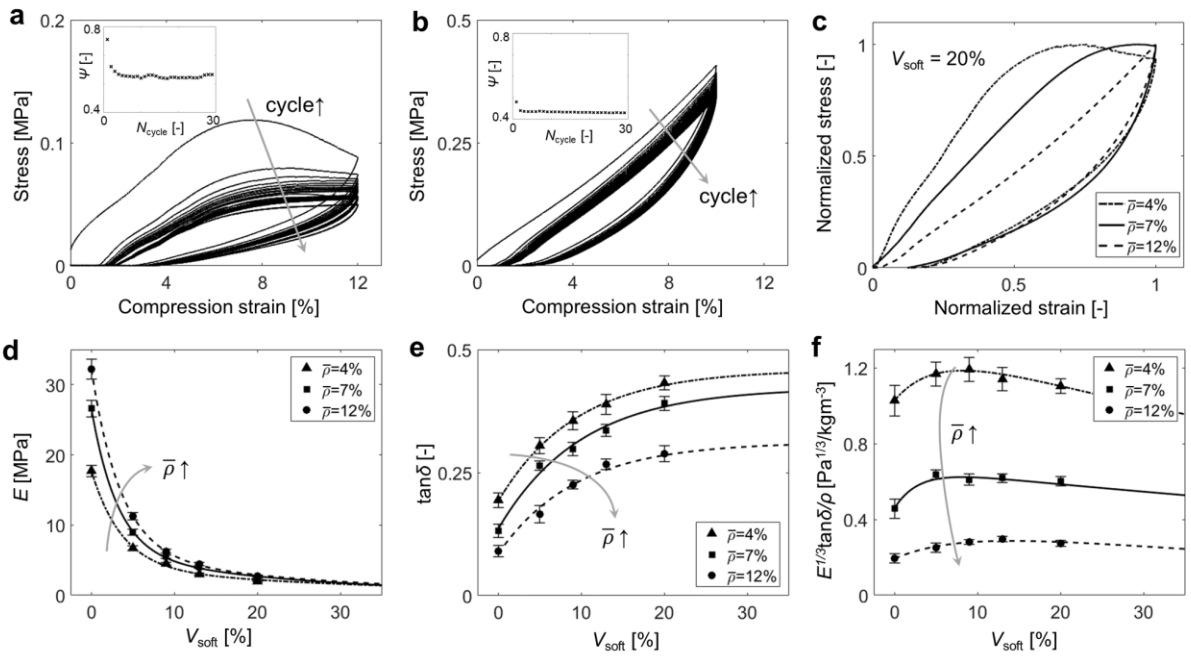

Figure 3-19 Structural damping properties of the lightweight cellular CFRP microlattices obtained from large strains quasi-static cyclic compression tests. (a)-(b) Hysteresis loops from multicyclic compression tests for 30 cycles and evolution of the loss coefficient with cycle number. (a) Sample with $\bar{\rho}$ = 4 % having V_{soft} = 20 %. (b) Sample with $\bar{\rho}$ = 12 % having V_{soft} = 20 %. (c) Normalized stress-strain hysteresis loops of samples having V_{soft} = 20 % with various $\bar{\rho}$. (d)-(f) The values were averaged over three test results, and error bars represent the standard deviation. (d) The effective modulus as a function of V_{soft} for different relative densities. (e) Loss tangent (tanδ) as a function of V_{soft} for different relative densities. (f) Damping figure of merit as a function of V_{soft}, showing its maximum at different V_{soft} for different relative densities.

3.8.6 Analytical model

We developed analytical models valid at small-strains and large-strains separately to compare with experimental results. By applying force-moment equilibrium, Timoshenko beam theory, and the

correspondence principle in the context of viscoelasticity together, the effective modulus of the structure under uniaxial compression can be written as

$$E_z^* = \frac{2\sqrt{2}}{9}\pi\left(\frac{r^2}{L_{\text{strut}}L_{\text{eff}}}\right)\left[E_{\text{CF}} + 2E_{\text{Reuss}}^*\left(1 + 12C_1\frac{r^2}{L_{\text{eff}}^2}\right)\right] \qquad \text{Eq. (3-3)}$$

where $E_{\text{Reuss}}^* = \left[\frac{V_{\text{soft}}}{E_{\text{soft}}^*} + \frac{1-V_{\text{soft}}}{E_{\text{CF}}}\right]^{-1}$, $C_1 = \left[\frac{12E_S I}{\kappa A G_{\text{Reuss}} L_{\text{eff}}^2}\right]^{-1}$, $G_{\text{Reuss}} = \frac{E_{\text{Reuss}}}{2(1+\nu_{\text{strut}})}$, and $\nu_{\text{strut}} = \left[\frac{V_{\text{soft}}}{\nu_{\text{soft}}} + \frac{1-V_{\text{soft}}}{\nu_{\text{CF}}}\right]^{-1}$, V_{soft} is the volume fraction of the soft phase, V_{CF} is the volume fraction of the CFRP phase in the single strut, and L_{eff} refers to the effective length, defined as $L_{\text{eff}} = L_{\text{strut}} - 2r$ where L_{strut} is the length of the strut and r is the radius of a circular cross-section of the strut. When the deformation is small, the intrinsic damping can be obtained via $\tan\delta = E''/E'$ using Eq. 3-3, where E'_z is the storage modulus (real part of E^*_z), and E''_z is the loss modulus (imaginary part of E^*_z). On the other hand, structural damping is caused by large strain deformations, and the microlattice results in energy dissipation through either elastic buckling or brittle-like deformation. Here, we assume that in-plane CFRP struts would not dissipate any mechanical energy because CFRP has negligible damping as compared to that of soft phase ($\tan\delta_{\text{CF}} \sim 0.07$ and $\tan\delta_{\text{soft}} \sim 0.3$). In a case of a dominant failure due to elastic buckling, the out-of-plane strut would buckle when the maximum stress reaches the critical buckling strength of the strut. According to Euler's buckling theory and a simple energy balance, the energy dissipation of the microlattice due to buckling can be written as

$$E_{\text{strut,buckling}}^{\text{out-of-plane}} = \frac{1}{2}\frac{F_{\text{buckling}}^{\text{cr,strut }2}}{K_{\text{strut}}^{\text{out-of-strut}}} = \frac{72\mathrm{E}_{\text{Reuss}}^{*}\pi^{5}r^{2}\left(\frac{r}{L_{\text{eff}}}\right)^{2}}{\left[1+2\left(\frac{L_{\text{eff}}}{r}\right)\right]^{2}\left[\frac{1}{L_{\text{eff}}}+12C_{1}\frac{r^{2}}{L_{\text{eff}}^{3}}\right]} \quad \text{Eq. (3-4)}$$

$$\Delta U_{\text{dissipated}}^{\text{buckling}} = \frac{fN_{b}\Delta E_{\text{strut,buckling}}^{\text{out-of-plane}}}{WLH} = \frac{24f\Delta E_{\text{strut,buckling}}^{\text{out-of-plane}}}{L^{3}\sin^{2}\theta\cos\theta} \quad \text{Eq. (3-5)}$$

where f is the fraction of the struts that need to buckle to accommodate the global displacement, N_b is the number of struts that need to buckling, W, L, and H are the dimensions of the microlattice, and $\Delta E_{\text{strut,buckling}}^{\text{out-of-plane}}$ is the elastic strain energy of the strut due to buckling. The fraction of the struts was assumed as $f = \varepsilon_{\max}/(1\text{-}2\sqrt{2}*r/L_{\text{eff}})$ [68]. Another main collapse mechanism is brittle-like deformation (mainly due to the yielding of base material). This mechanism may occur either globally or locally. With a similar procedure described above, the energy dissipation of the microlattice due to brittle-like deformation can be expressed as

$$\Delta E_{\text{strut,yielding}}^{\text{out-of-plane}} = \frac{1}{2}\frac{F_{\text{yielding}}^{\text{cr,strut }2}}{K_{\text{strut}}^{\text{out-of-strut}}} = \frac{72\pi\mathrm{r}^{2}\sigma_{\mathrm{y}}^{2}}{\mathrm{E}_{\text{Reuss}}^{*}\left[1+2\left(\frac{L_{eff}}{r}\right)\right]^{2}\left[\frac{1}{L_{eff}}+12C_{1}\frac{r^{2}}{L_{eff}^{3}}\right]} \quad \text{Eq. (3-6)}$$

The energy dissipation due to yielding $\Delta U_{\text{dissipated}}^{\text{yielding}}$ can be obtained similarly with Eq. (3-5) by replacing ΔE. Overall trends of the effective modulus and damping were reasonably predicted by the analytical model. However, we observed several discrepancies because the model assumes linear viscoelasticity, whereas the samples experienced a localized nodal fracture, finite size

effects, possible plastic deformation, and some degree of nonlinearity present in the stress-strain hysteresis loops. Moreover, we approximated a relationship between Ψ and tanδ as a linear relation since there was no reported literature. Nonetheless, the model was intended to provide an estimate of the damping properties with an order-of-magnitude margin.

3.8.7 Discussion

Fig. 3-20 illustrates the tunability maps of intrinsic and structural damping figure of merit using measured data and polynomial fittings in the V_{soft} -- $\bar{\rho}$ space. This map allows the designer to choose the volume fraction of the soft phase and the relative density for the desired figure of merit. The figure of merit for both intrinsic and structural damping has its maximum at low relative densities and at the soft phase ratio ranging approximately from 6 % to 12 %.

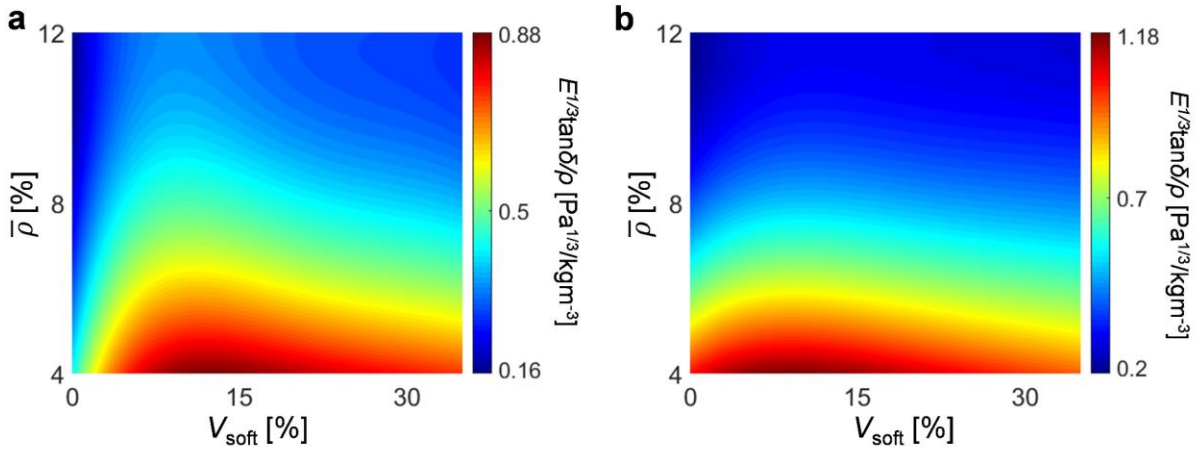

Figure 3-20 Tunability maps for (a) intrinsic and (b) structural damping performance in terms of the damping figure of merit obtained from experimental measurements.

A specific stiffness per density vs. loss tangent ($E^{1/3}/\rho$ --- tanδ) map was created to quantitatively assess the performance of the stiffness-damping pair of the CFRP microlattices against other existing materials (CES EduPack 2018, Granta Design [73]) for vibrational management (Fig. 3-21) [69, 71, 72]. The envelope defined by all experimental results is highlighted by an orange ellipse in $E^{1/3}/\rho$ vs. tanδ material space. The CFRP microlattices have specific stiffness comparable to commercially available CFRP while being dissipative as elastomers. For instance, the microlattices exhibit similar $E^{1/3}/\rho$ to that of technical ceramics and other composites and achieve improved damping by almost two orders of magnitude in loss tangent tanδ.

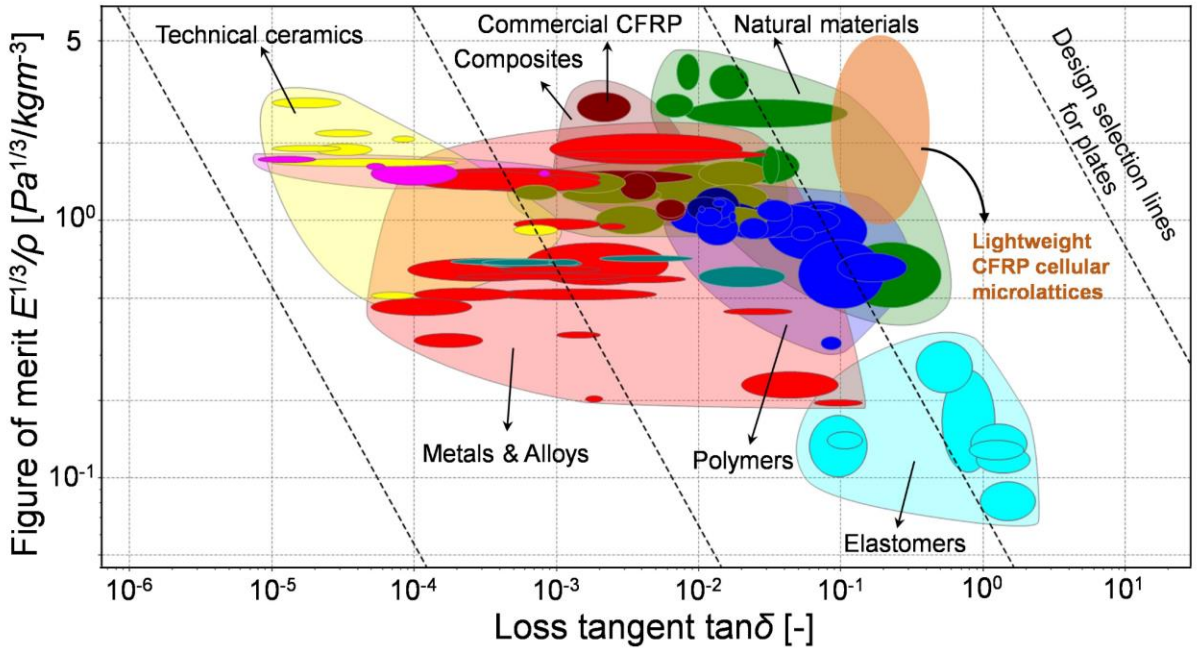

Figure 3-21 Assessment of vibration management of plates. The lightweight cellular CFRP microlattices developed in this work are compared against all existing natural and manmade materials in a log-log graph. The orange ellipse represents the envelope of all experimental results.

3.9 Conclusion

This chapter provides a detailed account of the development of an extendable multi-material projection stereolithography system, as well as its application to the fabrication of carbon fiber reinforced polymer composites. We focus on identifying the factors that can affect resin printability, such as viscosity and cure depth, to achieve optimal printing results. To verify the effectiveness of the system, mechanical testing is carried out on bulk CFRP composites, which is also supported by theoretical analysis. Following the successful mechanical testing of the bulk CFRP composites, we create octet-truss-based CFRP lattices using this methodology, which are then subjected to mechanical testing as well. The mechanical testing results are analyzed, with a specific focus on the size effect of the CFRP lattices. Finally, we introduce a group of two-phase lightweight, stiff, and high-damping carbon fiber reinforced polymer microlattices. The mechanical properties of these microlattices are characterized and discussed in detail, highlighting their potential for various applications. Overall, this work demonstrates the significant potential of the extendable multi-material PSL system for creating high-performance CFRP composites and microlattices.

Chapter 4 Additive manufacturing of fly-like, complex micro-architectures with dissolvable supports

In this chapter, the author introduces a novel light-based additive manufacturing approach called the multi-material projection stereolithography technique with dissolvable support (mSLAD), which enables the creation of arbitrarily complex architectures, including a large array of overhanging, fly-like micro-architectures. To achieve this, we developed a multi-material digital light printing technique that incorporates a dissolvable material. In this process, a soluble resin is used to print pillars or scaffolds that are designed to support overhangs. These printed supports can then be selectively dissolved in NaOH solution with the aid of sonication to accelerate dissolution. By doing so, we have eliminated the geometry constraints of the design and can access arbitrarily complex structures made from various polymers and composites. This work showcases the AM of a range of micro-scale structures without the need for manual support removal. Furthermore, the author designed and printed a suite of 3D metamaterials that incorporate a variety of overhanging features, including fly-like micro-architectures, with extreme aspect ratios exceeding 40. These developments enable a range of novel applications, such as the attenuation of structure-borne waves across wide and tailorable frequency ranges with a fraction of the weight of conventional counterparts. Additionally, the printed metamaterials offer mode-selective propagation through active soft 3D magnetic metamaterials.

4.1 System design and methodology

4.1.1 System setup

A generalized schematic of the bottom-up multi-material PSL system [1, 17] is presented in Fig. 4-1a. To manufacture structures with dissolvable supports, firstly, CAD models are sliced into two different groups of cross-sectional images such that each group represents one material. These two-dimensional slices are subsequently digitized and sent to a UV light engine, which projects images at 405 nm. Then, the spatially patterned UV light is projected through a set of optics and focused on the oxygen-permeable window, which is made of transparent glass coated with PDMS. Polymerization initiates at the light-exposed areas, converting it into a solid single-layer part and sticking to the build platform. A thin oxygen inhibition layer (dead zone) forms above the printing window, preventing solidified resin adhesion. The build platform elevates to replenish resin and repeat the cycle. A material exchanging system is connected to the vat, allowing different resins to be delivered to the vat and solidified. When material change is needed, ethanol is quickly pumped to the chamber, washing off the previous resin trapped inside the printed structure and the resin tank; afterward, a new resin is pumped via the exchanging system to replace the ethanol for printing the following layers. The exchanging process takes 15s to 30s, depending on the resin viscosity. The process was repeated layer by layer, combining multiple materials into a 3D structure. With the current configuration, the light irradiance of the projection system can be up to 7 mW/cm^2 with a lateral printing area of 15×20 mm^2. The light engine is equipped with a DMD chip of 912×1140 pixels with a projection resolution of 20 μm after projection optics. The layer thickness is set by the vertical motion axis to be 30-50 μm, depending on the cure depth of each

resin. After printing, the sample is cleaned with ethanol and dried using compressed air, followed by UV post-curing (~10 mW/cm^2) for several minutes.

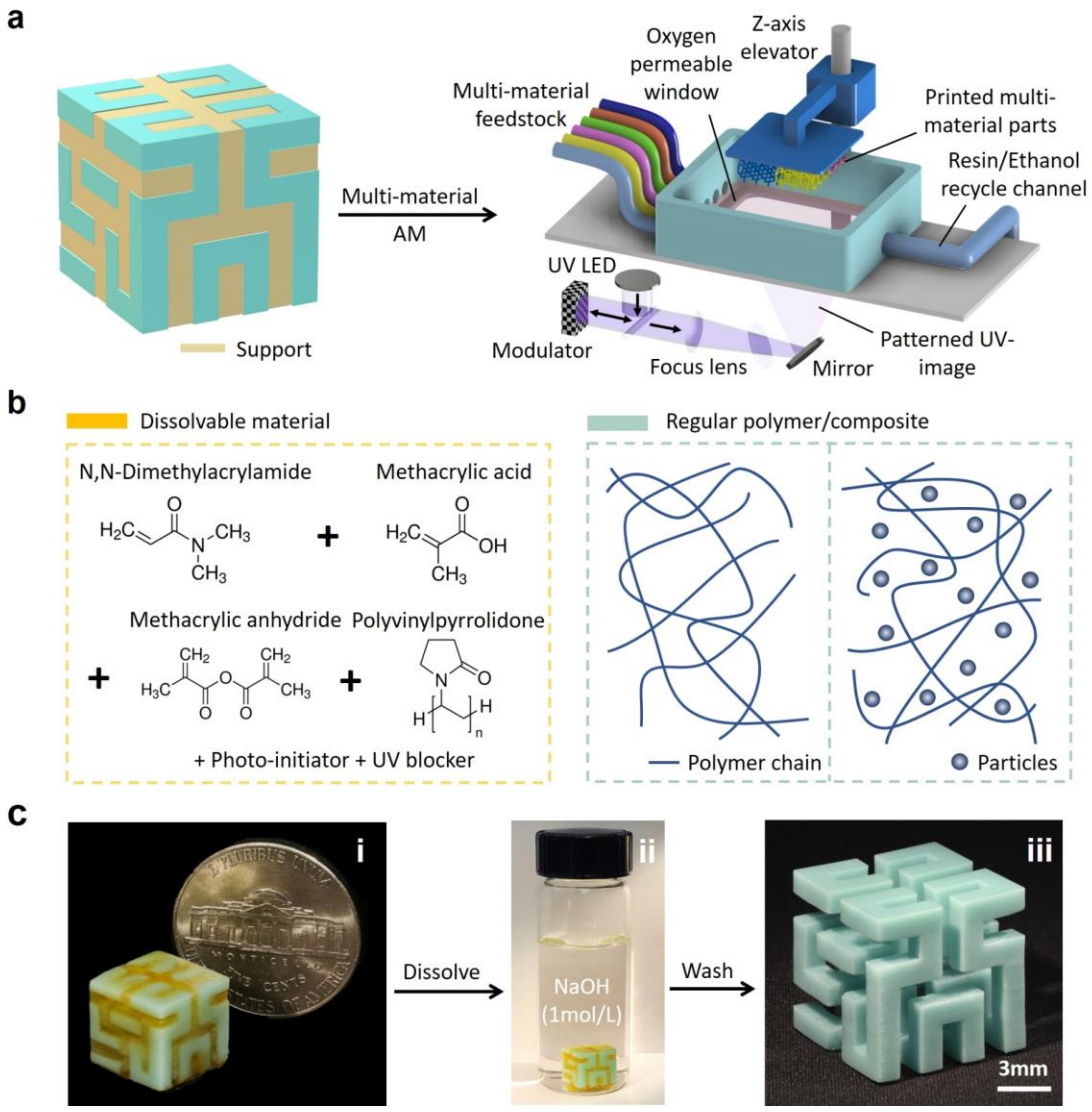

Figure 4-1 Multi-material projection stereolithography technique with dissolvable support (mSLAD) process. (a) Schematic of a Hilbert cube with dissimilar constituent material and the multi-material PSL system. (b) Chemical composition of soluble material and schematic of the photopolymer/composite after solidification. (c) Dissolution process of the Hilbert cube: (i) 3D printed Hilbert cube was printed using the multi-material printer. The cyan part is the cube, and the yellow part is the dissolvable support. (ii) The cube was then sonicated in NaOH solution. (iii) Hilbert cube after dissolving.

4.1.2 Selective dissolution methodology

Our 3D selective dissolution scheme is based on the arrangement of different materials in a 3D structure and the multi-vat photopolymerization process. To achieve this, we set out to prepare a group of UV-curable resins that will be applied for multi-material printing. As shown in Fig. 4-1b, we formulate blends of monomers and fillers, a radical initiator, and dye to form a photopolymer resin which is rapidly dissolvable by aqueous base-catalyzed ester hydrolysis to be used as the support material. Base-catalyzed hydrolysis is selected because it has been well-known and characterized for 3D-printed photopolymer materials. The resins consist of hydrophilic, low molecular weight monomers, which can be rapidly photocured in air, and poly(vinyl pyrrolidone) filler to increase water solubility. A high content of monoacrylates makes a low crosslink density network to enhance alkaline solution diffusion in and hydrolyzed polymer out. Through the custom multi-material PSL system, we combine dissolvable resin with typical photopolymer resins, as well as composites, into 3D architectures programmed by the part's digital design.

To demonstrate our scheme, we combined the dissolvable material with a regular commercial photopolymer and printed out a Hilbert cube, which was then soaked in NaOH solution (1 mol/L), along with sonication, to dissolve the support structures (Fig. 4-1c). Subsequently, the cube was washed in ethanol and dried using compressed air. In this way, a Herbert cube with high feature fidelity (beams width variation: < 5%) and a good surface finish could be formed.

Dissolution time, which ranges from a few minutes to tens of minutes, highly depends on the volume and the surface area of the printed dissolvable material. The smaller the volume and the larger the surface area, the faster the speed. Sonication and temperature are the other two factors that affect dissolving speed. We tested the dissolving rate of cubes made by dissolvable material under different conditions, and the results revealed that sonication significantly helps the dissolving process, and heating also accelerates the process (Fig. 4-2). With sonication and heating applied simultaneously, ~80% of the cube (560 mm^3) is dissolved in 10 minutes. In practice, heating up to 50 ℃ might damage the desired structure, causing deformation of delicate architecture. Therefore, in this study, the temperature was controlled to be around 30-40℃. Moreover, we find that the heating/etching process won't affect regular polymer's mechanical properties within 6 hours (Fig. 4-3).

4.1.3 Dissolving speed test

Cubes were fabricated using dissolvable material, as shown in Fig. 4-2, and were immersed in NaOH solution. Increasing temperature slightly increases the dissolving speed. Sonication and heating dramatically increase the dissolving speed. The dissolved percentage refers to the ratio between the dissolved weight and the original weight of the cube. The dissolution curves were fitted based on experimental results in MATLAB.

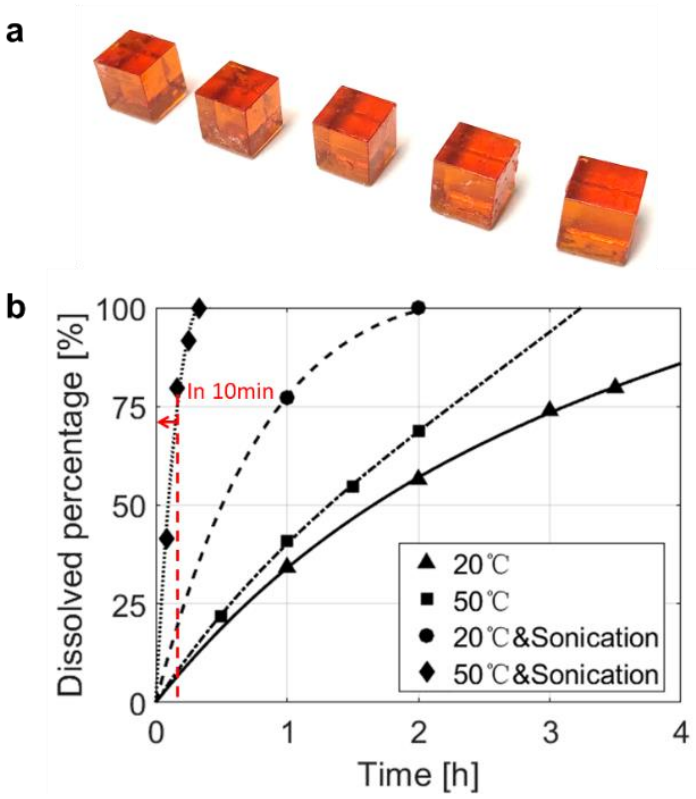

Figure 4-2 Dissolving speed measurement of the soluble materials. (a) Optical image of cubes (length=8.25mm) made of dissolvable material. (b) Dissolution curves of the cubes in NaOH solution (1 mol/L) under four different conditions.

4.1.4 The effect of heating/etching on the mechanical property of the 3D printed polymer

To verify whether heating/etching will affect the mechanical property of 3D printed regular polymers or not, we performed mechanical tension tests on a representative polymer (PEGDA) before and after heating/soaking (heating up to 40℃/soaking in 1 mol/L NaOH solution) for 6 hours. As shown in the stress-strain curves below, we can see that the mechanical properties of the three groups of the sample are close and within the margin of error.

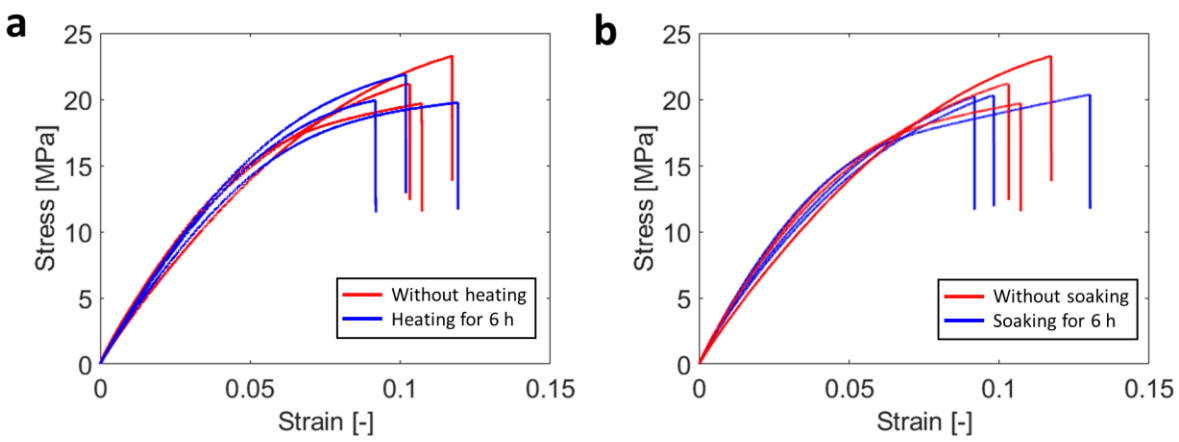

Figure 4-3 Measured stress-strain curves of the samples made of PEGDA before and after heating/soaking.

4.2 Materials and methods

To demonstrate the methodology's ability to process various polymers/composites for complex architectures, we formulated dissolvable resin, regular polymers, and a photocurable magnetic-responsive soft suspension. These materials have dramatically different properties regarding their inherent mechanical property, processability, and functionality. In this work, a suite of micro-architectures with embedded overhanging features, including elastic and active metamaterials, were 3D printed and applied to a few application scenarios as validations of the approach. The following section documents the materials and methods used herein.

4.2.1 Materials and resin preparation

Most materials were purchased from Sigma-Aldrich and used as received: N, N-Dimethylacrylamide, Methacrylic acid, Methacrylic anhydride, Polyvinylpyrrolidone, Phenylbis

(2,4,6-trimethylbenzoyl) phosphine oxide (Irg819); Sudan (I); polyethylene glycol diacrylate (PEGDA); Bisphenol A ethoxylate dimethacrylate (BPAEDA); trimethylpropane triacrylate (TMPTA). For the magnetic resins, Ebecryl 242 and 114 were donated by Allnex. Black iron oxide (Fe_3O_4, size of 30 μm) was purchased from Alpha Chemicals, and EPD particles were purchased from Rahn. Cyan resin was purchased from Anycubic.

Dissolvable resin: Acrylic-based photopolymers N, N-Dimethylacrylamide (40 wt%), Methacrylic acid (40 wt%), Methacrylic anhydride (7% wt%), water-soluble filler Polyvinylpyrrolidone (11 wt%), and photoinitiator Irg819 (2% wt%) [74]. PEGDA resin: PEGDA, with 0.05 wt% Sudan (I), and 2 wt% Irg819. BPAEDA-TMPTA: Mixture of BPAEDA and TMPTA (85:15), with 0.05 wt% Sudan (I), and 2 wt% photoinitiator Irg819. Magnetic resin (MAG, 15 vol%): A flexible resin consisting of a mixture of 20 ml Ebecryl 242 and 114 (1:1), 2 wt% EPD, and 2 wt% Irg819 was prepared. 15 g iron oxide particles were combined with the flexible resin in a 50 ml grinding jar and then dispersed with a high-energy ball mill (Retsch) for 50 min.

4.2.2 Measurement of the mechanical properties and printing resolution

To evaluate the mechanical property of the base materials, which will be used as inputs for numerical verification of the experimental results, tensile test samples were prepared using the same printing parameters as the lattices for the mechanical test (per ASTM D3039). The stress-strain response of the samples was captured using an INSTRON 5944 test frame equipped with a 2000 N load cell. A strain rate of 10^{-3} 1/s was adopted to ensure that all samples deform quasi-statically. Load-displacement curves were collected by the software linked to the test frame and were converted into engineering strain and stress. Material properties were averaged over the

results of three samples per base material. 3 primary materials that were used in this work have Young's modulus of 426.9 MPa (PEGDA), 62.3 MPa (BPAEDA-TMPTA), and 6.5 MPa (MAG, 15 vol%).

Since the curing behavior of different materials varies, their printing resolution can also differ. To determine the resolution for each material, we printed several small patterns using the aforementioned materials, as illustrated in Fig. 4-4.

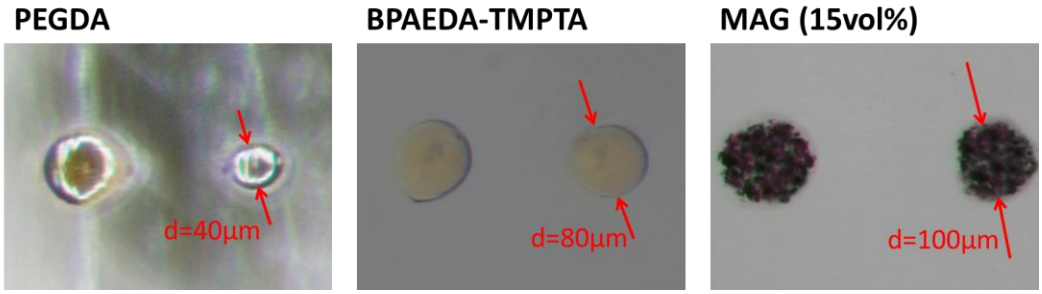

Figure 4-4 Optical images of the minimal printable features with 3 types of resins that are used in this chapter.

4.2.3 Measurement of wave transmission

A custom measurement platform was built to characterize the dispersion of elastic waves of the metamaterials experimentally. A piezo actuator (PC4QR, ThorLabs) or a piezo film sheet (X2B, TRS technologies) was attached to the bottom plate of the star-shaped lattice/magnetic lattice to produce the input longitudinal excitations. A function generator (SDG 1025, Siglent) and a piezo amplifier (VP7206-24H805, Piezo Master) were used to drive the piezo actuator at a frequency range of 10-10000 Hz for star-shaped lattice and 10-2500 Hz for magnetic lattice (sine wave output). A displacement sensor (LK-H008, Keyence) was used to capture the displacement at 100

kHz sampling frequency. The measured transmission through the sample was then normalized with respect to measurement without the sample. The transmission curves were calculated via the formula, $T = 20\log_{10}(A(f)/A_o(f))$, where T refers to the transmission in dB, $A_o(f)$ is the amplitude of the actuator and $A(f)$ is the amplitude of the data measured when the sample is in place.

4.2.4 Band structure and wave transmission simulation

In order to verify the experimentally measured results and understand the underlying wave transmission mechanisms via the trampoline effect enabled by the large overhanging features, numerical simulations were implemented in a commercial finite element software (COMSOL Multiphysics v5.5). For the start-shaped lattice solid, Young's modulus of 62.3 MPa, a density of 1.1 g/cm^3, and Poisson's ratio of 0.4 were employed. For the magnetic lattice solid, a modulus of 6.5 MPa, density of 1.6 g/cm^3, Poisson's ratio of 0.4, and a loss factor of 0.75 were employed.

4.3 Realization of various complex micro-architectures

4.3.1 Fabrication of various complex 3D structures and surface roughness measurement

We printed the dissolvable resin into various 3D structures, creating highly complex arbitrary structures with delicate features that were not feasible with manual support removals. As shown in Fig. 4-5a, a freely moving Voronoi-ball was printed within an enclosed birdcage. Support was added between the cage and ball, which is not accessible for a plier or tweezer, restricted by its small-scale and structural geometry. Two intersected hollowed annuls (Fig. 4-5b) were printed. Fig. 4-5c shows printed jewelry molds that eliminate post-manual support removal and sanding.

The reported method leaves almost no residue on the delicate features. Furthermore, this technique could benefit the consumer jewelry industry because any surface that supports are in contact with requires extra post-processing to remove supports manually [75, 76]. Due to the unique property of the dissolvable material, using mSLAD, residues can be avoided on the surface of the printed rings, and many hours could be saved for post-processing. Fig. 4-5d compares the surface finish of the as-fabricated sample using the conventional support removal method and mSLAD. We observe that the solution can remove most of the dissolvable material with little residual.

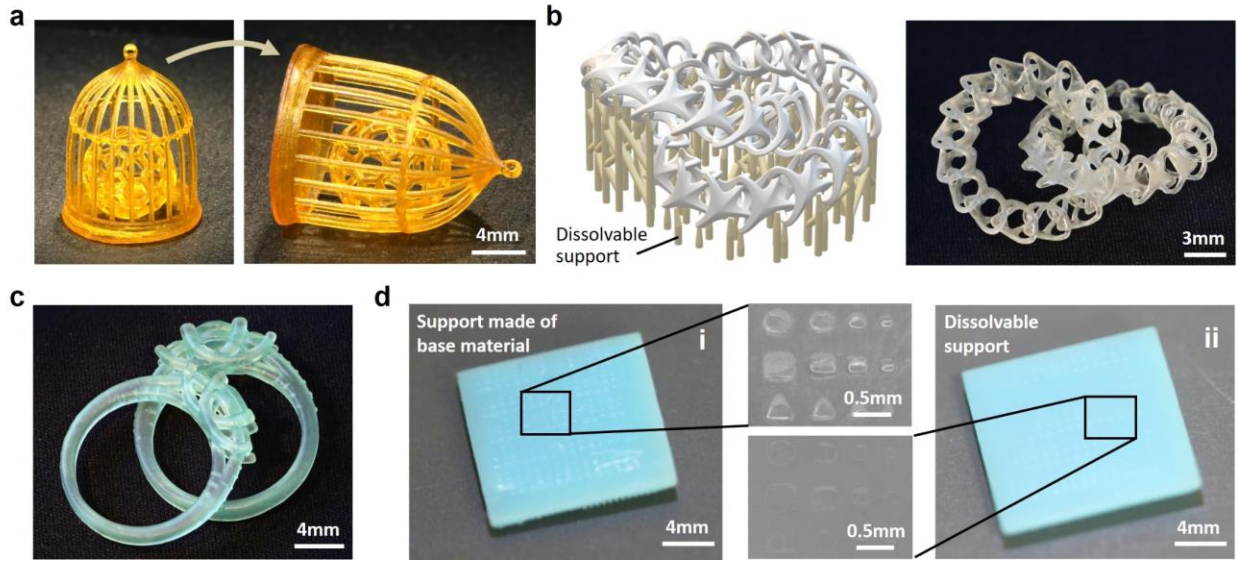

Figure 4-5 Fabricated samples using mSLAD. (a) Freely moving Voronoi ball in a birdcage. (b) Intersected hollowed annulus. (c) 3D printed rings with delicate features. (d) Optical images of structure surface post-fabrication by (i) regular PSL + manual support removal; (ii) mSLAD + Dissolving.

To evaluate the surface roughness of the structure post-fabrication, we set up a measurement platform, as shown in Fig. 4-6a. A regular commercial UV resin and the dissolvable resin were used for fabrication. Regular support was removed manually using a knife, while the dissolvable

support was selectively dissolved in NaOH solution. The distance sensor captures the distance from the sensor to the sample surface, while the translation stage moves from one side to the other to capture the displacement profile of the cross-section where supports are added. From plot Fig. 4-6b, we can see that the stubborn residual can be as high as 200 μm for regular support, even though a knife was used for removing. In contrast, little residual can be seen using mSLAD from the plot. Here maximum peak (Ry) can be used as a parameter to evaluate the surface roughness. For regular support, Ry = 217.1 μm; for mSLAD, Ry = 15.4 μm.

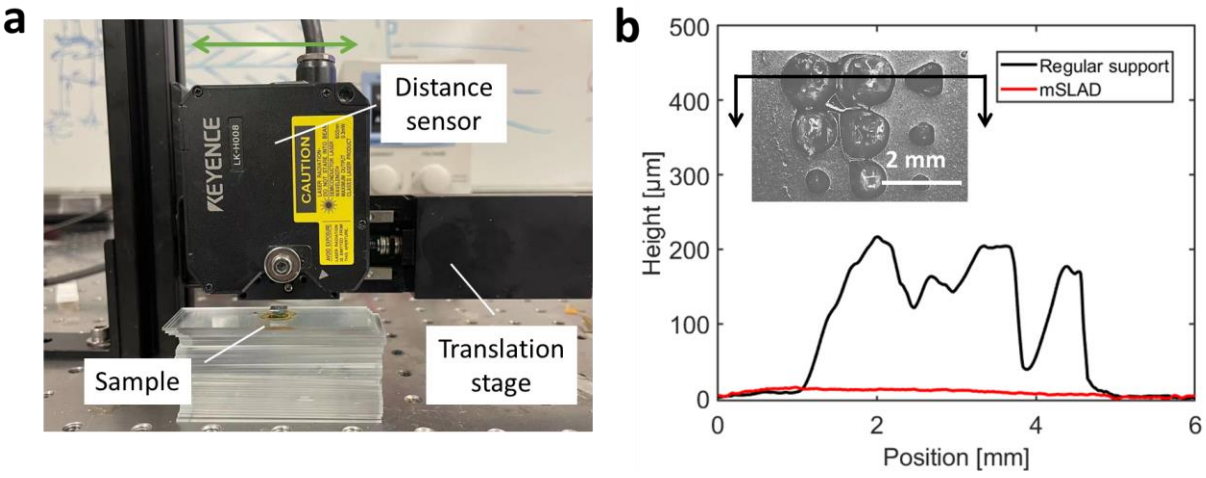

Figure 4-6 Surface roughness measurement of the support residuals. (a) Surface roughness measurement setup. (b) Measured surface profiles of the samples post-fabrication by (i) regular PSL + manual support removal; (ii) mSLAD + Dissolving.

4.3.2 Fabrication of micro-architected materials with large arrays of overhanging features

The rapid elimination of support material makes it possible to print complex micro-architected materials with a large array of flying or overhanging features where support removal is extremely challenging in the PSL approach. In Fig. 4-7, we show a group of as-fabricated lattices with

hundreds of internal microscale overhangs, not feasible to be fabricated by other AM techniques. These architectures are typically isotropic, with suspended or fly-like features that will flow away inside liquid once polymerized without solids connecting to the substrate during printing.

Fig. 4-7a shows a class of isotropic re-entrant metamaterials [77] with internal suspended nodes in all six planes. Thin rods were added in the digital model as dissolvable supports connecting each internal node to the substrate to fix their location during printing. Once printed, these internal rods were subsequently dissolved, leaving behind isotropic re-entrant lattices with all internal fly-like suspended nodes.

The second category of micro-architectures that are not possible to be printed is embedded large overhangs, which need multiple vertical supports to prevent them from detachment during printing. Fig. 4-7b shows a type of cubic metamaterial with negative stiffness (NS) [13]. The outer cubic frame and the inner re-entrant elements feature large overhangs that are entirely isolated from the substrate. Multiple support beams were designed and selectively dissolved post-fabrication.

Another class of metamaterials is micro-architectures that are self-supported but with high aspect ratio features and a large inclination angle that, due to gravity and separation force during printing, will significantly deform due to bending-induced deflection. Fig. 4-7c demonstrates a non-self-supported auxetic metamaterial with a high aspect ratio strut members as high as 40 [78, 79]. Fig. 4-7d demonstrates the printing of previously unachievable large inclination angle features with soft composite. With an ultimate strength of 0.65 MPa after curing, without support materials at the inclined beams, the soft resin (MAG, 15vol%) tends to fracture and break away from the substrate within a few layers.

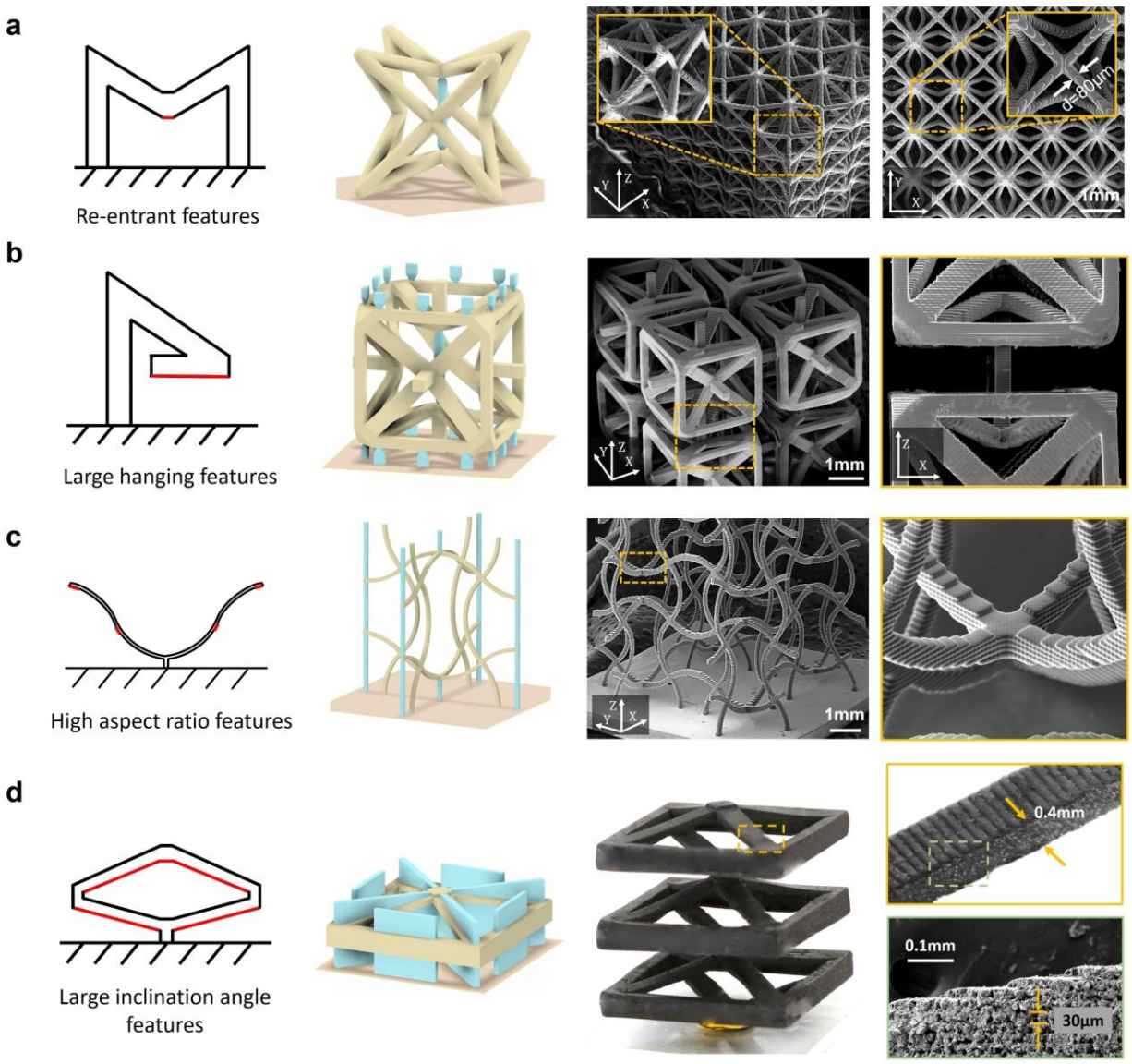

Figure 4-7 Classifications of free-standing micro-architectures that require support removal and results of features post mSLAD process. The red marks in the 2d schematics denote the overhanging features that need support. The cyan sections in the 3d schematics refer to the supports. The lattices were printed by mSLAD, and the images were captured using SEM. (a) A re-entrant lattice structure with struts diameter of 80 μm. (b) A micro-scale cubic architecture with large overhangs. (c) An auxetic lattice with high aspect ratio struts. (d) A negative stiffness lattice with large inclination angle beams made of soft magnetic composite. The enlarged area shows the high aspect ratio beams that were printed with a layer thickness of 30 μm.

4.4 Ultralight elastic metamaterials

4.4.1 Design of star-shaped lattice and simulation

Incorporating a large number of embedded overhanging and flying features within micro-architectures allows novel metamaterials not achievable by existing approaches. Here we demonstrate a new class of ultralow density elastic micro-architected metamaterials with star-shaped re-entrant topologies that can achieve wide-band omnidirectional vibration attenuation. The high porosity (exceeding 90% void space) of the proposed micro-lattice enables low mass density as low as 0.09 g/cm^3. The design features a network of low-stiffness suspended nodal structures within overhanging micro-unit cells that facilitate a pair of distinct local resonance-based bandgaps at relatively low frequencies.

As shown in Fig. 4-8a, the star-shaped re-entrant lattice structure composed of isotoxal square stars that are mutually perpendicular to each other in the three orthogonal planes is designed, where over 130 internal supports are needed inside the lattice topology. Each unit cell comprises 30 solid cylindrical rods of the same diameter and intrinsic material. Here, the outer connecting rods and the unique re-entrant structure allow for the existence of multiple omnidirectional local resonance bandgaps for elastic waves and enable complete vibration attenuation over tailorable frequency ranges (For further information, the reader is referred to the author's previous work [80, 81].). In contrast to metamaterial such as octet truss lattices with all nodes identical and highly connected [46, 58], the unit cell topology of the star-shaped re-entrant metamaterials reveals two distinct nodal structures (node 1 and node 2), where node 1 is suspended in the air. The two distinct types

of nodal structures allow for unique local resonance behaviors, giving rise to two distinct bandgaps (Fig. 4-8b).

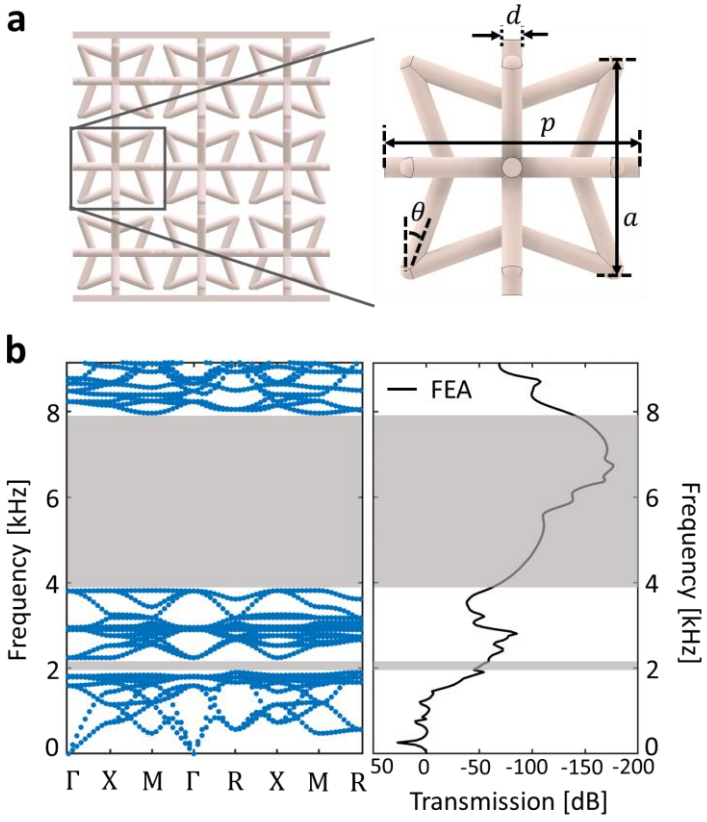

Figure 4-8 Design and simulation of the star-shaped re-entrant lattice. (a) Design of the star-shaped re-entrant lattice: p is the periodicity, a is the distance between the vertices of the isotoxal squares, θ is the angle between the outer edges of the isotoxal square stars and the vertical normal. (b) Normalized band structure along the different directions of the IBZ and numerically calculated elastic wave transmission (dB) through the 3-3-3 lattice. The shaded grey regions indicate the band gaps. Here the design has a p = 8 mm, θ=20◦, a = 0.8p, and d=0.1p.

4.4.2 Fabrication and testing of the star-shaped lattice

To print such a re-entrant lattice, micropillar dissolvable materials were added to connect the nodes of re-entrant struts to support the overhanging edge of each unit cell. Such a design facilitates a

shorter fabrication time, and the dissolvable materials are instantly disassociated during post-processing within several minutes. Fig. 4-9a(ii) and (iii) show the printed re-entrant micro-lattice with an overall length of 15 mm and a strut radius of 0.2 mm. The existence of two complete bandgaps is first seen in the numerically calculated bandstructure along the different regions of the irreducible Brillouin zone, shown by regions in shaded grey (Fig. 4-9c).

To experimentally characterize the dispersion of elastic waves, a measurement platform is built, as shown in Fig. 4-9b, where the lattice is excited by a piezo actuator, and a sensor is placed above the top plate to capture the output displacement amplitude. The lattice in Fig. 4-9b shows the normalized displacement field map from numerical simulations that the frequency of excitation of the base (here, piezo actuator) lies within the bandgap region. As can be seen here, when an elastic wave at 6 kHz is excited at the bottom plate of the sample, the lattice completely reflects the incident wave; hence, the mechanical vibration does not propagate through more than half a unit cell, leading to high wave attenuation. Fig. 4-9c shows the calculated bandstructure associated with the lattice and the experimentally measured elastic wave transmission through the sample in the frequency range between 0 and 10 kHz. The experimental curve undergoes sharp decays in transmission for frequencies between 1.90 kHz and 2.25 kHz and from 3.82 kHz to 7.97 kHz, denoting complete wave attenuation in these regions and confirming the existence of the two bandgaps that are observed in the numerically calculated bandstructure shown on the left (shaded grey regions). The presented experimental results agree well with the numerical simulations, demonstrating two complete bandgaps at low frequencies. A slight shift of the bandgaps in the experimental results can be attributed to minor deviations in the intrinsic material's stiffness and the measurement equipment's performance limitations, and this is consistent with the previously

observed bandgaps in the case of a larger sample [81]. Furthermore, via tailoring Young's modulus and feature size of the ligament, a wide frequency range can be achieved, as shown in Fig. 4-9d.

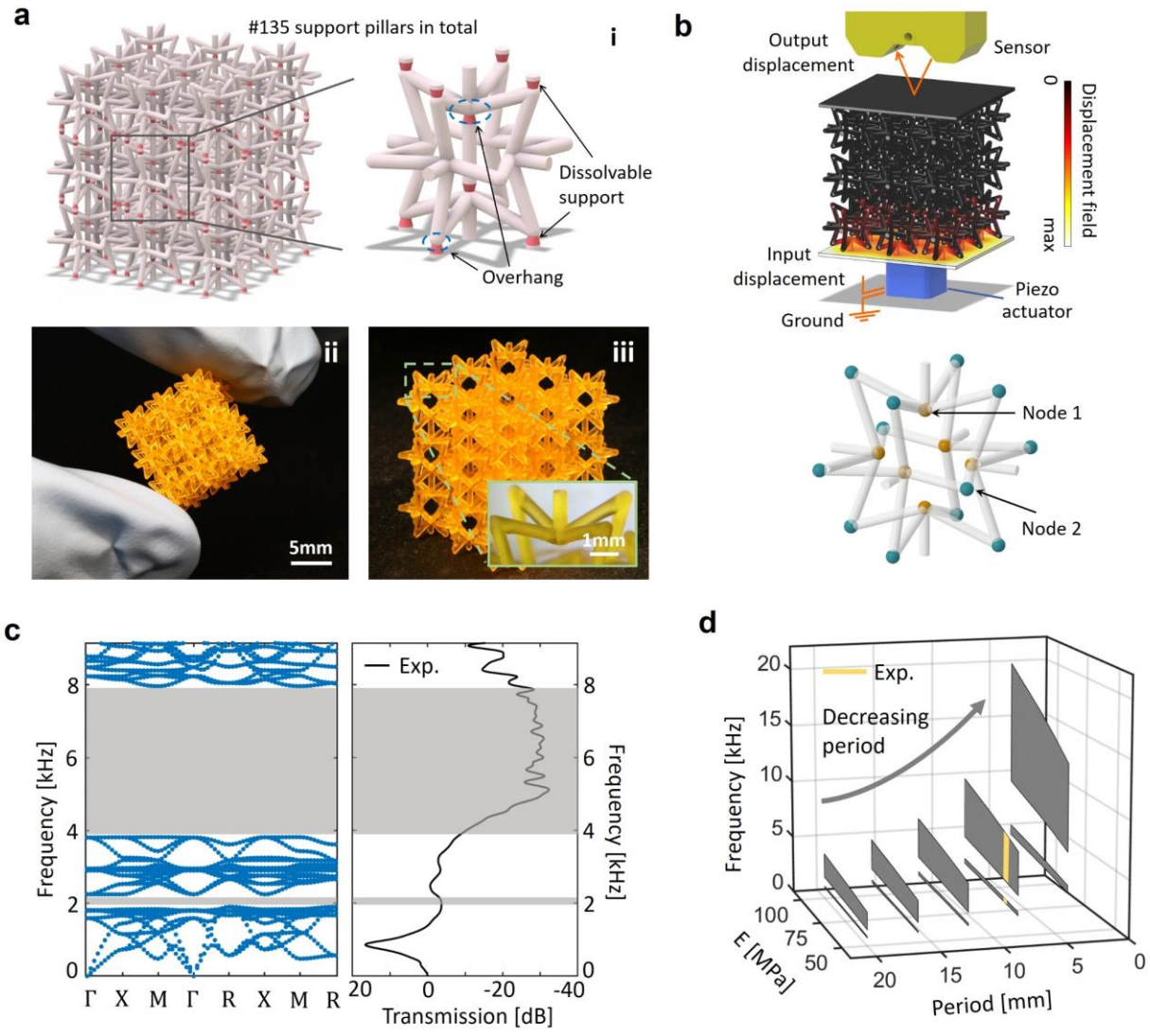

Figure 4-9 Printing and testing of the star-shaped re-entrant lattice. (a) The star-shaped re-entrant lattice: (i) Designed lattice with 135 internal support pillars, where the circled areas are the overhanging section that needs support, and the pink sections refer to the dissolvable material. (ii)(iii) 3D printed re-entrant lattice (made of BPAEDA-TMTPA) after removal of supports. (b) Schematic of the measurement platform and two different nodes of the star-shaped unit cell. The test sample was printed with side plates using the same material for the testing amenity. The lattice shows the numerical results of the normalized displacement field at a frequency of 6 kHz. (c)

Bandstructure of the lattice (left figure) and experimentally measured elastic wave transmission (right figure) through the lattice. The shaded grey regions indicate the bandgaps. (d) Accessing bandgaps that occur at larger frequency ranges by decreasing the structure's period and changing the base materials' stiffness. Period = 8 mm and E = 62 MPa for the tested sample.

4.5 Actively tunable magnetic metamaterial

4.5.1 Design of the magnetic metamaterial

The mSLAD can also be applied to soft multi-functional materials. Here we leverage our fabrication approach to conceive and illustrate magnetically tunable morphing actuators. We design metamaterials that display a negative stiffness behavior under external axial forces caused by sequential snap-through instabilities [13, 14]. The designed NS structure can exhibit significant shape changes under a remote magnetic field and recover to its original shape upon removing the applied magnetic field. As shown in Fig. 4-10a, the NS unit cell comprises a cuboid frame and 8 connecting beams with an inclination angle of α. By tuning the beam aspect ratio $\lambda=L/h$ and inclination angle, the snap-through response can be tailored accordingly.

The slenderness ratio and the inclination angle of the lattice were selected based on the intrinsic material property of such elastomer so that the beams can have a snap-through behavior under compression force and recover their original shape upon release.

To reveal the snap-through behavior, we performed a uni-directional compression test on a unit cell of the negative stiffness design. Fig. 4-10b shows the effective stress-strain curve. When the strain is small (< 0.15), the displacement induces monotonically increasing positive stress and positive stiffness. However, when the stress is close to the buckling stress of the bottom beams,

the effective stress increases slightly and decreases monotonically until the beams fold and the frame touches the ground. Then the effective stress increases again until the upper beams buckle, resulting in the second dip, giving rise to a snap-through response.

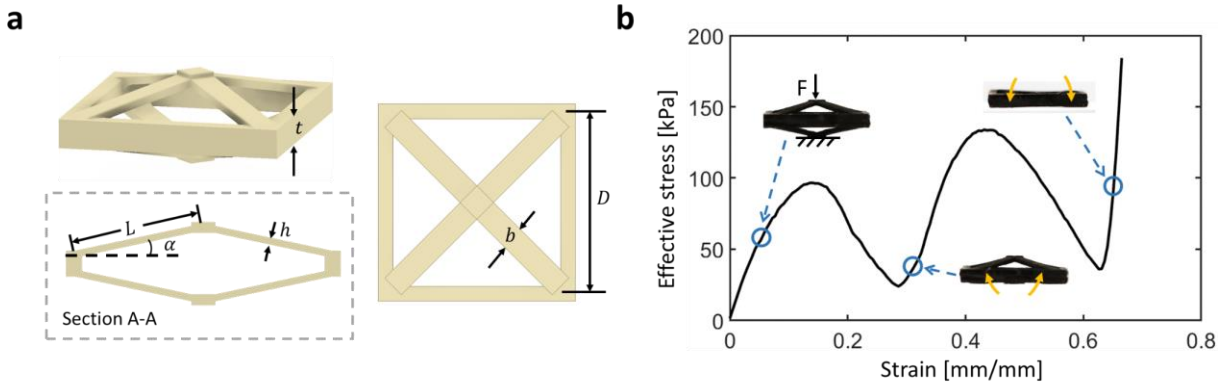

Figure 4-10 Design and testing of the negative stiffness structure unit cell. (a) Design of the negative stiffness unit cell: D = 12 mm, L = 7.374 mm, α = 12.5°, h = 0.42 mm, b = 1.44 mm, t = 1.56 mm. (b) Effective stress vs. strain of the negative stiffness unit cell under compression.

4.5.2 Experimental setup of the magneto actuation

A magnetic field was applied to the lattice using two permanent Neodymium Block magnets (N52) positioned on the bottom of a glass plate. The magnetic field was measured with a Gaussmeter (WT10A, Weith Magnetic Technology). The magnetic fields from the permanent were modulated by varying the distance between the magnet and the lattices (Fig. 4-11, Fig. 4-12). The magnetic field around the bottom center of the lattice was denoted as the applied magnetic field.

The lattice strain was calculated as $\varepsilon = 1 - h/h_0$, where h and h_0 are the undeformed and deformed lattice heights, respectively. A camera captured the deformation process, and ImageJ was used to extract the height of the lattice.

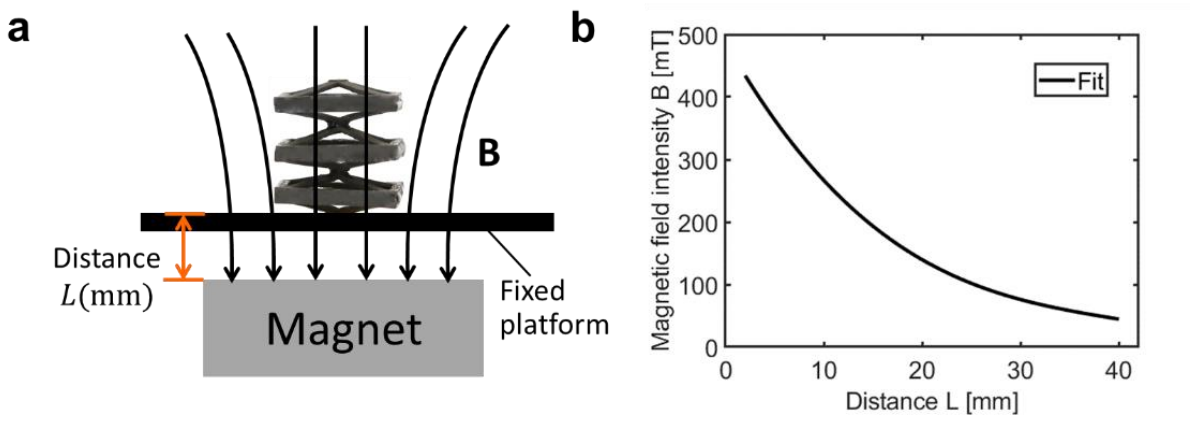

Figure 4-11 Setup of the actuation testing and magnetic field measurement. (a) Schematic of the setup of the magneto actuation experimental testing. (b) The magnetic field intensity at the center area above the permanent magnet. The curve was fitted in MATLAB.

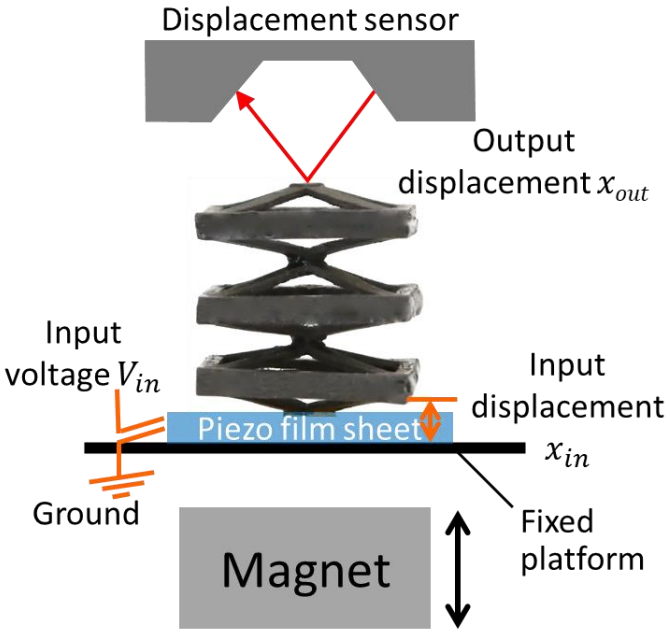

Figure 4-12 Setup of the displacement measurement for magneto actuation. (a) Schematic of the vibration transmission testing fixture for the magnetoactive lattice. The magnetic field intensity was controlled by moving the magnet.

4.5.3 Fabrication and testing of the magnetic metamaterial

To enable the fabrication, we first developed a UV-curable magnetic resin that comprises a mix of soft elastomer and ferrimagnetic particles (see previous section). The cured soft magnetic composite has a stiffness of 6.5 MPa and a yield stress of 0.35 MPa, which will generate significant deformation and fracture due to large deflection as a result of the low Young's modulus, large inclination angle (77.5°) and high aspect ratio in excess of $\lambda = 17$. Due to the shadowing/blockage of internal areas by the external frames and beams, removing the inner support structures is not feasible with direct PSL. Fig. 4-13a shows successfully printed magnetic architectures featuring negative stiffness via the snap-through effect.

To enable magnetically actuated structural buckling, we apply a controlled magnetic field B through the lattice. Fig. 4-13b demonstrates how the shape of an NS lattice changes with an increasing magnetic field. Unlike a force-induced deformation, Initially, the lattice deforms slightly with the increase of the magnetic field. When the magnetic field is close to the critical buckling magnetic field (B = 70 mT), a small incremental magnetic force triggers snap-through instability -- the first layer of beams within the lattice snap and are subsequently locked in a new shape. As the magnetic field continues to ramp up, the lattice continues to fold as new layers of architecture reach their critical snap-through thresholds. As a result, the displacement undergoes multiple displacement jumps from one state to another (displaying multiple self-locked shapes, Fig. 4-13c). Upon switching the magnetic flux to a lower level, the metamaterial will accordingly reverse and lock into its previous state. Reversing the field to zero allows the structure to

completely recover to its original unfolded state. As we apply a cyclic magnetic field with a period of 2 s, the lattice morphs back and forth based on the magnetic field amplitude.

These magnetically triggered shape transformations and self-locking can be harnessed to enable controlled elastic wave transmission within designed frequency regimes. We tested the wave transmission properties by exciting the bottom of the lattice with a piezoelectric film sheet with sweep frequencies (0 – 2.5 kHz) and measured their transmission ratio with a laser displacement sensor while the lattice shapes being locked by the magnetic field at the snap-through threshold. The curves in Fig. 4-13d denote the transmitted wave as a function of frequency for each locked shape. These results clearly illustrate that the system enables field-controlled elastic wave transmission. It can be seen that increasing the magnetic field increases the frequency at which the highest transmission occurs, indicated by the different transmission curves corresponding to the magnetic field-triggered lattice shapes. Here, the lattice can be considered as a combination of the spring-mass models, where the 8 connecting beams refer to the spring, and the center cuboid refers to the mass. Each self-locked lattice shapes refer to specific oscillators (spring-mass system). For instance, shape 1 is equivalent to 3 masses coupled with 4 springs, while shape 3 represents 1 mass coupled with 2 springs. Therefore, such field-responsive metamaterial would possess multiple different transmission frequencies to be selected from a remote magnetic field, which could enable helmets or wearables where desired frequencies are judiciously selected. For example, wave transmissions can be switched “ON” via a discrete set of frequencies or suppressed (“OFF”) via other frequencies, shown in the displacement field maps in Fig. 4-13b.

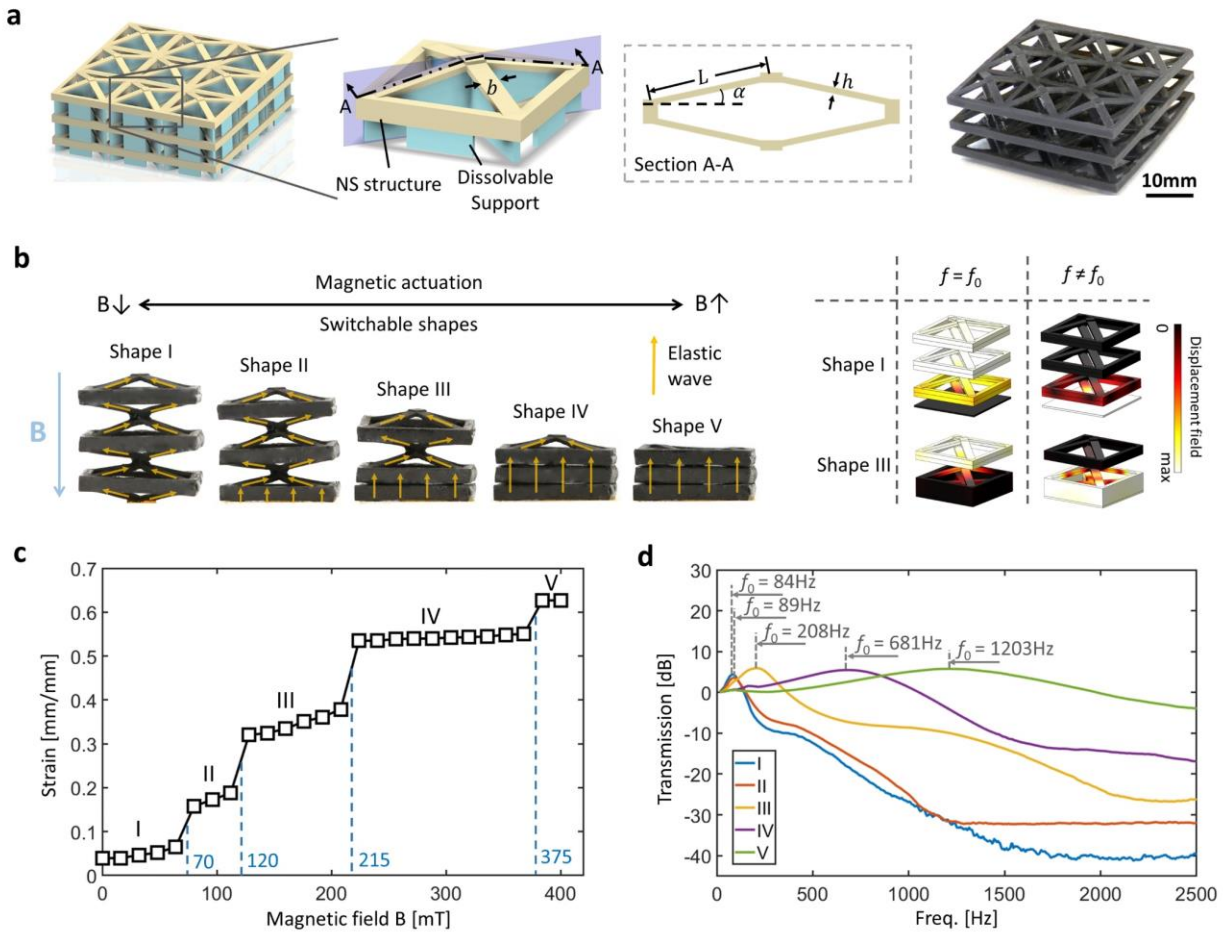

Figure 4-13 Printing and testing results of the magneto actuator. (a) Negative stiffness magnetic lattice design and printing. (b) The architected negative stiffness structure has configurable shapes under different magnetic fields, resulting in different transmission ratios. Yellow arrow: elastic wave propagation across the structure. The schematics are simulation results of the normalized displacement field for shape 1 and shape 3 at its "ON" ($f = f_0$) and "OFF" ($f \neq f_0$) status. (c) The effective strain of the lattice as a function of the magnetic field. (d) The measured transmission of elastic waves of the lattice with different shapes. The resonance frequency of the lattice shifts from 84 Hz to 1203 Hz (from shape 1 to shape 5).

4.6 Discussion and conclusion

Comparing the resolution of mSLAD to other multi-material or support-free AM methods compatible with internal support removal and suspended features (Fig. 4-14), such as FDM [82-

84], SLS [85-88], and material jetting [89-92], our selective dissolution method enables the fabrication of complex architectures with suspended features at the scale < 100 μm. Additionally, the reported method allows for direct 3D printing of branch-like features and structures with a material Young's Modulus of less than 10 MPa, which is not possible with current SLA approaches [93, 94], where the soft materials and overhanging features experience large deflections and are detached from the substrate.

Moving forward, we recognize the limitations of our presented work with respect to scale and printing speed. Specifically, for PSL, the feature scale is limited to the trade-off between the resolution and building area of the light engine. Several strategies can be employed to increase the build area while maintaining resolution, such as moving the translation stage or optics or employing light engines with large pixel numbers. For example, Zheng et al. proposed to use galvanometric mirrors and customized scanning lenses to project the light pattern across a large printing area, enabling microscale features fabricated within a feature size span over four orders of magnitude [46]. Such a technique can be integrated with the mSLAD to increase the build area while keeping a high resolution.

The mSLAD methodology reported herein can also be applied to other multi-material stereolithography techniques. Despite the efficient synchronization between motion stages, pumps, and image projection sequences, the printing time of the current system can be prolonged to hours when many material exchange processes are involved as a result of the cleansing procedure between a material exchange. Han et al. proposed a multi-material printing system using dynamic fluidic control, which could efficiently switch the printing material and significantly reduce the

printing time [49]. This method is also compatible with dissolvable material and other regular polymers developed for mSLAD.

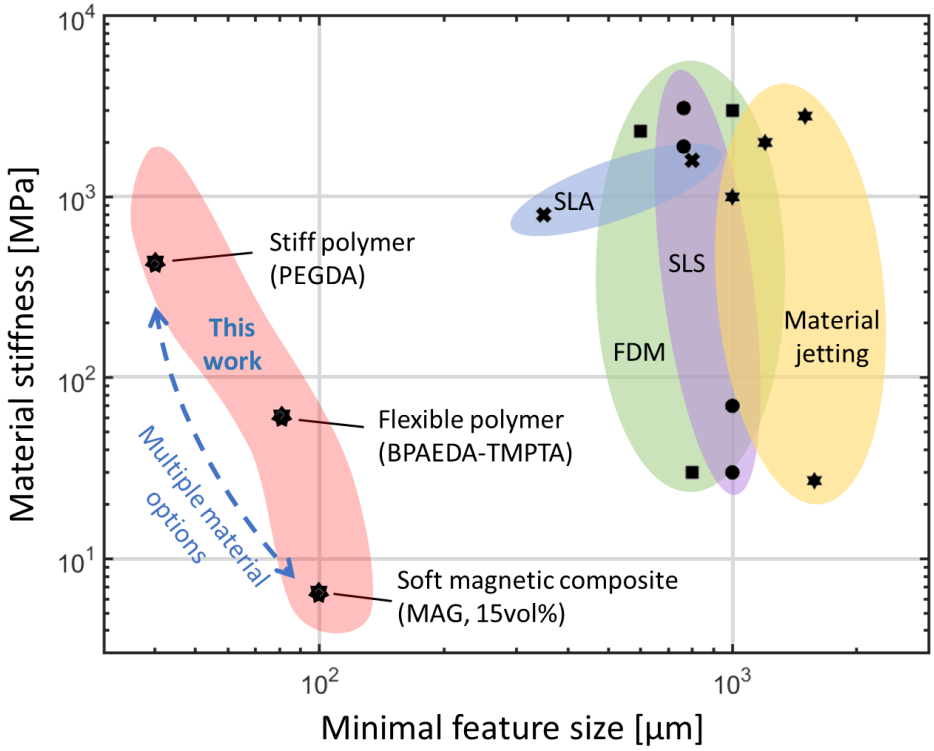

Figure 4-14 The accessible feature sizes and range of stiffness enabled by this work and other reported 3D printing techniques capable of printing internal suspended features. mSLAD enables suspended micro-architectures with microscale resolutions and various materials.

In this chapter, we developed an AM process to create 3D micro-architectures with a large number of free-standing embedded features via dissolving a second-phase photopolymer. Using this process, we fabricated complex structures, metamaterials, and soft multi-functional materials with a large array of fly-like features, large overhangs, and high aspect ratio struts in excess of 40 that are inaccessible by the current SLA approach. The resolution of this method allows printing

features an order of magnitude smaller than techniques including powder bed process, material jetting, and fused deposition modeling. The material process is not limited to polymer; a variety of multi-functional materials, conducting, and ceramics can be incorporated herein. It will have direct implications for the streamlined production of jewelry and dental products, metamaterials, bio-scaffold, 3D battery architectures, and micro-antennas with arbitrary features and complexity free from manufacturing-imposed topology constraints.

Chapter 5 Development of a large-scale high-resolution scanning projection stereolithography system

This chapter focuses on developing a scanning projection stereolithography (SPSL) system that integrates an optical scanning system to expand the printing scale to over 50 cm while reducing printing time through optimized scan paths and motion speeds. This system provides concurrent ability to print unprecedented large-scale parts with a minimal feature size of 50 μm, which enables the fabrication of architecture materials with features spanning over four orders of magnitude for many applications. We discuss the design and optimization of the SPSL system, as well as the fabrication of lightweight architected lattice materials of various sizes using CFRP. The fabricated materials exhibit mechanical properties that can be precisely controlled by their internal geometries. The SPSL system presented in this chapter represents a major step forward in the development of large-scale high-resolution AM of architected materials and opens up new avenues for research and innovation in this exciting field. This system can be further enhanced by integrating multi-extrusion nozzles to achieve precise control over fiber orientations and enabling multi-material 3D printing.

5.1 System design and methodology

5.1.1 Hardware setup

This study employs the bottom-up approach of PSL due to its ability to fabricate large parts with less resin [95]. The designed large-scale high-resolution SPSL printer, as illustrated in Fig. 5-1a,

follows a typical configuration with the projection system located beneath a resin tank, projecting images below to solidify resin on the printing platform. The resin tank's bottom is made of transparent, non-stick Teflon film (FEP), which is attached to a UV-grade fused silica window with a thickness of 2 mm to provide a rigid structure. The build plate with a size of 22 cm×35 cm is mounted on an aluminum extrusion connected to translation stages (Fig. 5-1b). To counteract the large separation force generated when printing large-area patterns, two motion stages capable of sustaining a maximum load of 150 N are placed at each end of the aluminum extrusion, improving the load capacity and balance of the entire mechanical system.

To achieve both large-scale and high-resolution 3D printing, we developed a projection system capable of translating the projection images across the horizontal plane. This projection system consists of a light engine, three lenses, two reflection mirrors, and two motorized linear translation stages. The fundamental working principle of the system is based on the infinity-corrected optical design [96], as shown in Fig. 5-1c. Here, light rays emitted from the light engine, which is equipped with a DMD chip, pass through a collimating lens and enter as an infinity parallel beam in the focusing lens, forming an intermediate image. The intermediate image is subsequently relayed through a projection lens and formed into the final image. In contrast to the conventional projection system in PSL printing technology, where the focused image will be out of focus as soon as the lens moves, our infinity-corrected projection system allows the translation of the projection image over a large distance while keeping the focus and intensity -- the image size stays constant even if the distance between the collimating lens and the focusing lens is changed. Thus, the projection images can be translated via a high-speed motion axis. As shown in Fig. 5-1d, the light engine is fixed on the ground, and the scanning optics move along the x-y directions, sequentially projecting

images onto the resin vat. The reflection mirrors, focusing, and projection lenses are all mounted onto the motion stages, allowing fast and precise scanning.

The infinity-corrected design allows for easy adjustment of the projection area and resolution by tuning the position of the projection lens and projection plane. This is possible because the overall magnification ratio can be adjusted by changing the distance between the projection lens and the intermediate image (d_o), and the effective focal length of the optics (f_c, f_f and f_p). Specifically, the overall magnification ratio M can be calculated as $M = \frac{f_f}{f_c}\frac{f_p}{d_o - f_p}$. This flexibility in magnification ratio makes it possible to adapt the printer to different 3D printing tasks with varying feature size requirements.

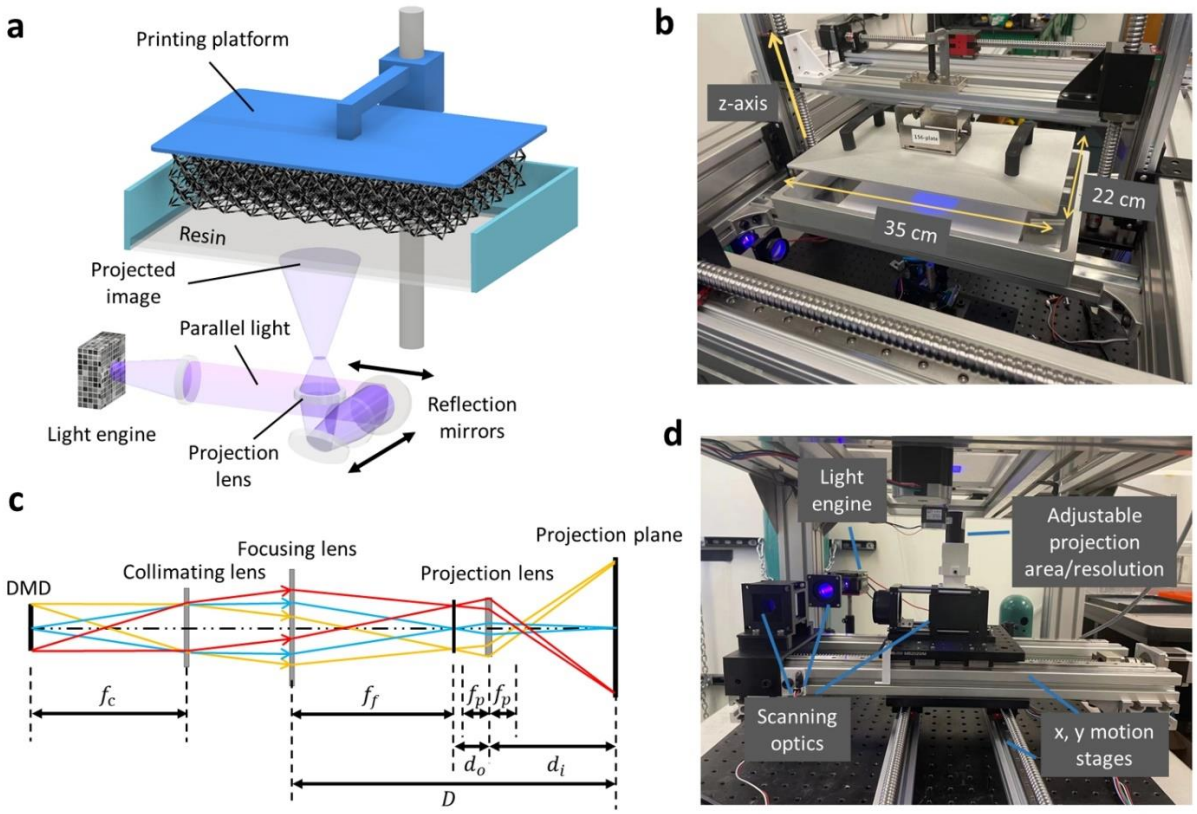

Figure 5-1 Large-scale high-resolution PSL system setup. (a) Schematic of the large-scale high-resolution scanning projection stereolithography system. (b) The system is equipped with a large format printing vat and two powerful motion stages. (c) The optical path diagram of the infinity-corrected projection design. (d) Adjustable scanning optical system mounted onto two precision translation stages.

5.1.2 Optical design and evaluation

When designing the projection system, it is essential to properly understand the role of each optical element in order to ensure optimal illumination. Fig. 5-2a shows the designed optical system in Zemax. The system consists of an illumination source (the DMD chip), collimating and focusing lenses, projection lenses, and two reflection mirrors. A light engine (Wintech, Inc) equipped with a DMD chip of 1140×912 pixels (9.855×6.1614 mm) is used in this work. Only the light rays

emitted from the DMD chip are considered since they are the ones that contribute to the projection. The incident angle of light from the surface of the DMD is measured to be approximately 11°. To ensure optimal optical coupling efficiency, it is important to use a collimating lens with a relative aperture (NA $\cong \frac{D}{2f_c}$, where D is the diameter, and f_c is the working distance/focal length of the lens) that is greater than or equal to the sine value of the incident angle (0.191). A doublet-convex lens with a diameter of 50 mm and an effective focal length of 100 mm could be selected as the collimating lens. A tube lens (Thorlabs Inc.) was employed as the focusing lens to form an intermediate image. The size of the intermediate image depends on the size of the DMD chip and the focal length ratio between the focusing and collimating lenses (f_f/f_c). To ensure the projected image's integrity, the projection lens's entrance pupil must be larger than the size of the intermediate image. The last projection lens plays a crucial role in magnifying the projected image to a specified size, and in this work, we utilized a commercial lens from Wintech Inc.

In theory, collimated light should maintain a consistent diameter from the lens to infinity. However, in practice, no physically collimated beam can maintain an exact diameter as it travels. The divergence of the beam, which is the rate at which its diameter changes, is influenced by the characteristics of both the light source and the collimator [97]. This restricted the working distance of the setup to within 50 cm in this work. To assess the performance of the system, we used Zemax simulation software with a wavelength of 405 nm based on the final design. Two standard analysis tools were employed here. The first analysis tool used was “Field Curvature and Distortion” to assess astigmatism and distortion of the optical system. Fig. 5-2b displays the results of the analysis, where the vertical axis on the left graph represents the field of view, the solid line represents the

field curvature of tangential planes, and the dotted line represents the field curvature of the sagittal plane. The difference in the horizontal distance between these two curves is the value of astigmatism. The right graph shows the distortion of the optical system in different fields of view. We observed a maximum astigmatism of 20 μm and a maximum distortion of less than 0.002% at the edge of the image plane. Another analysis tool used to evaluate the system's performance is the spot diagram, which plots the intercepts of rays on the image plane. The root mean square (RMS) of the radial size is a parameter used to evaluate the spot size on the spot diagram, and it gives a rough estimate of the spread extent of light. Fig. 5-2c shows the spot diagram of the system at the center and the corner of the projection area. The spot sizes of the given plots were found to be less than 20 μm, indicating good performance.

It is worth noting that the simulation was carried out at a working distance of 100 mm, which is the distance between the collimating and focusing lens. Although changes in working distance can lead to slight differences in aberrations, all aberrations observed in the simulation fall within acceptable ranges. To demonstrate the resolution of the projection system, we set the projection area to be 20×16 mm^2 and fabricated a tiny pyramidal array using the developed CFRP composite, as shown in Fig. 5-2d. The printed part exhibited sharp edges at a scale of less than 50 μm, which is a testament to the excellent performance of the optical system.

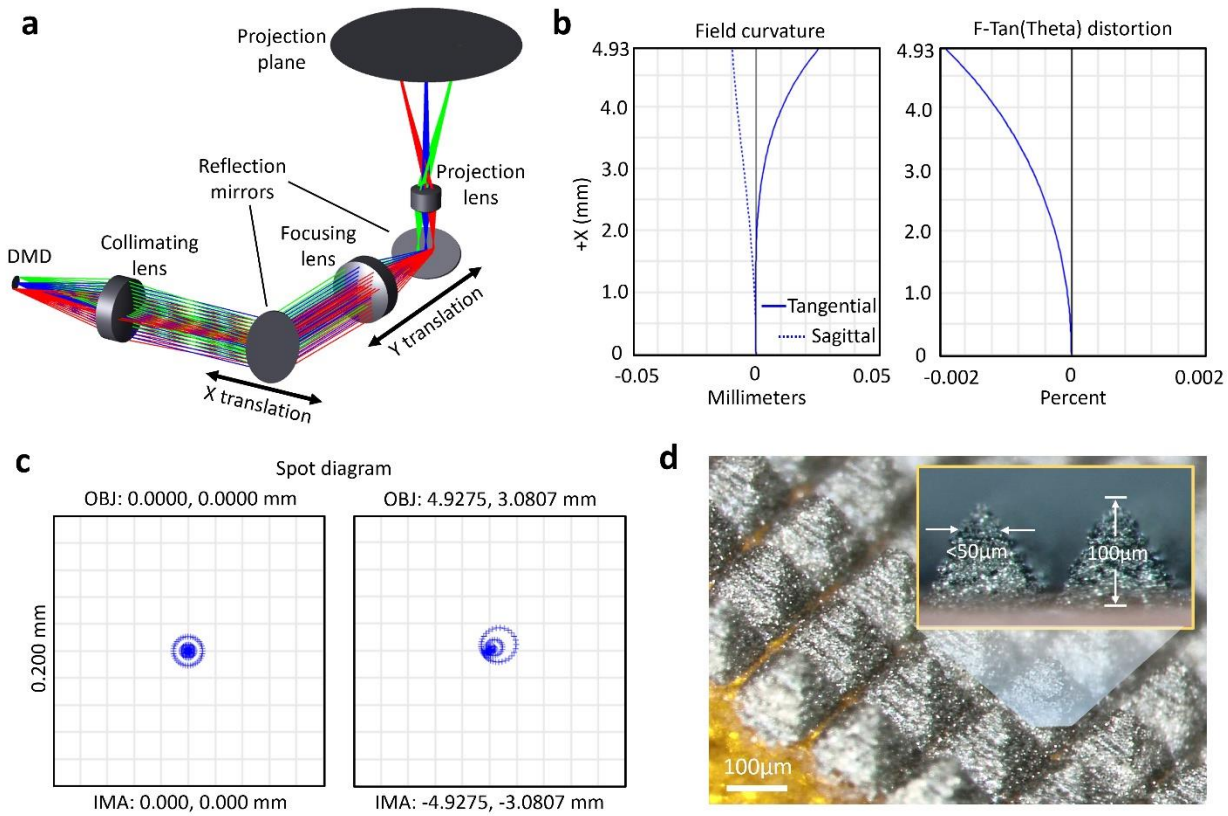

Figure 5-2 Optical simulations of the infinity-corrected projection system. (a) Ray-trace simulation for the infinity-corrected projection design. (b) Field curvature and distortion map of the projection system. (c) Spot diagram of the projection system. (d) As-fabricated pyramid microstructure array at a projection size of 20×16mm^2.

5.1.3 Control system design

Fig. 5-3 depicts the processing and control schematic of the printing system. The process begins with a 3D model, which is used to generate 2D images for curing using software such as Netfabb or nTopology. The sliced images and 3D model are then processed in MATLAB to generate a scanning G-code file and segmented sub-images. An optimization tool for scanning paths is employed to identify void sub-images in each layer, resulting in optimized scanning paths that

control the scanning axes' movement. The scanning file is incorporated into LabVIEW for execution.

The lower computer system consists of a Duet 2 board and an Arduino board, both of which are connected to a PC and controlled by the LabVIEW program via USB. The Arduino board controls a shutter that blocks background light when exposure is absent, while the Duet 2 board controls the motion stages of the optical system and receives signals from limit switches. The LabVIEW program directly controls the projector.

The diagram's color-coded lines represent different types of controlling and processing signals. Specifically, blue lines denote file processing, red lines denote the 24V power circuit, green lines denote analog or digital signals, and yellow lines denote power circuits for motors.

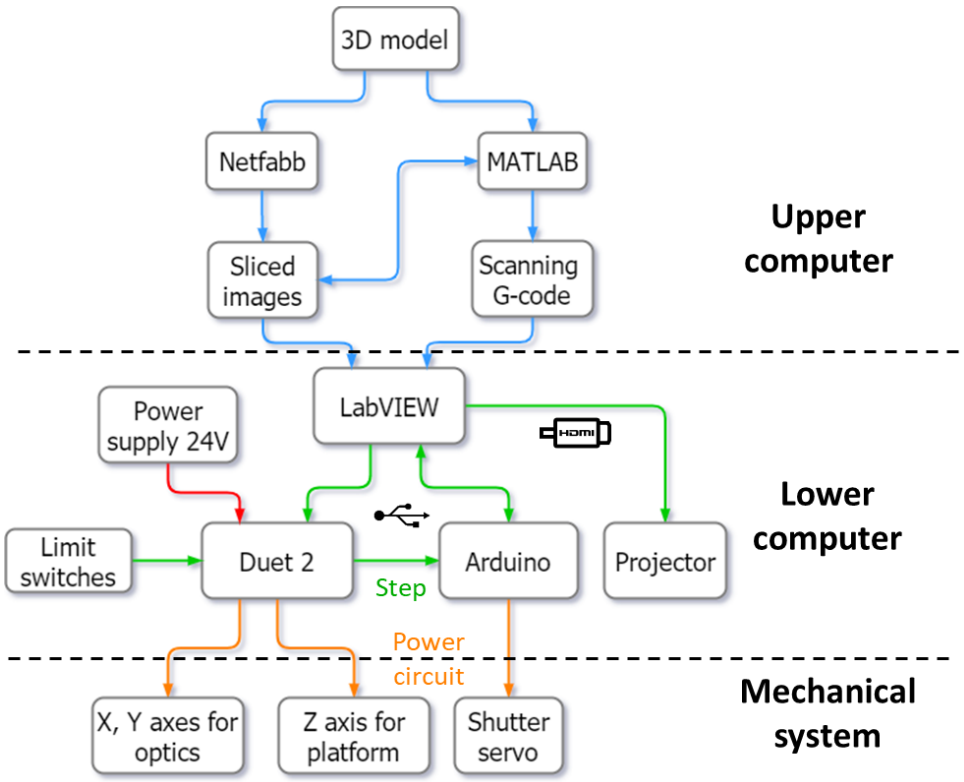

Figure 5-3 The processing and control schematic of the printing system.

5.2 Fabrication process

5.2.1 Lattice design and slicing process

Commercial software, Autodesk Inventor and nTopology, are used to design the Voronoi vase. Firstly, a solid vase 3d model is created in Inventor and imported into nTopology as the volume to fill. Then, a randomized list of points with gradient spacing within the body is generated. The interval between points gradually decreases from two ends (10 mm) to the neck (1 mm). The Voronoi lattice is created by connecting the generated points, followed by thickening each beam with variable thickness. Gradient thickness across the vase is applied to accommodate small spacing around the neck section. The minimum thickness of the struts is set to 50 μm, and the maximum is set to 2 mm. Usually, a mesh file (.stl file) is needed for slicing to obtain images to be used for exposure. However, the vase presents a challenge due to its intricate structure consisting of numerous unit cells, resulting in an excessively large file size of over 10 GB, making it challenging to convert to a mesh file. To address this issue, we utilized a function in nTopology that enables direct slicing of the "implicit body" into images. We opted for a layer thickness of 50 μm and set the pixel count of each image to 5700×6384 to meet the printing resolution and area requirements. Next, we utilized MATLAB to split each sliced image into 5×7 sub-images, with each sub-image containing 1140×912 pixels, and prepared them for transmission to the light engine.

It's worth noting that the projection area size of each exposure can be adjusted based on the target model's resolution and size specifications. For instance, when high printing accuracy isn't required, increasing the projected area of each sub-image can reduce the number of movements required during the printing process. To illustrate, in the design of the energy absorber with a wall thickness of 1 mm, each sliced layer comprises 3×5 sub-images with an overall projection area of 22.4×28 cm^2. Our code is versatile enough to support different image sizes and segment them into pre-defined sub-sections.

5.2.2 Scan path optimization

To showcase large-scale high-resolution printing capabilities, we designed a vase using nTopology software. The vase has a volume of 20×20×50 cm^3 and features a minimal strut thickness of 50 μm. To begin the printing process for the vase, the 3D model is first sliced into 2-dimensional images with predefined pixels, as illustrated in Fig. 5-4a. Each layer is then segmented into a set of sub-images, which are projected sequentially onto the vat as the stage moves along the x-y directions. Each sub-image represents a specific projection area, and the projected UV images initiate the polymerization of the resin, resulting in a solid single-layer part. To ensure a strong bond between neighboring sections, a small overlap area (usually several pixels) is introduced between sub-images.

For the vase, each sliced image is divided into 35 sections ($mn = 5 \times 7$), as described in the materials and methods section. Traditionally, an S-shape scan path is applied to cover the entire area. However, for a hollowed or more complex structure, scanning the black sections is unnecessary and a waste of time. Therefore, a scan path that minimizes movement time is desired.

While it is possible to find the shortest scan time path by an exhaustive method for the case in Fig. 5-4b, it becomes extremely challenging when k=20 (where k refers to the number of sub-images with patterns in one layer) for the case in Fig. 5-4a. This problem corresponds to the classical optimization problem known as the "Traveling Salesman Problem" (TSP), for which no general solution exists. To solve the problem, we developed a MATLAB code based on a genetic algorithm [98] to intelligently plan the scan path for each layer. The code identifies sub-images with projection patterns and generates a scanning route file for the stage motion control.

As depicted in Fig. 5-4b, the blue dotted lines represent the conventional S-shaped scanning route, while the highlighted yellow line represents the shortest scan time path among all possible routes that pass through the necessary projection areas. It should be noted that we assume two motion stages move simultaneously when moving from one location to another, and the slower stage is used to quantify the time cost. The optimized path may differ depending on the speed of the linear stages. It is worth noting that, unlike conventional TSP where the optimized path needs to be connected at both the beginning and end, our scanning method has a fixed starting point and an open endpoint. As shown in Fig. 5-4b, for layer n, the scanning begins at the green point and ends at the red dot. Then, the endpoint of layer n becomes the starting point for layer n+1, and so on. This approach further reduces unnecessary scan movements during layer changes. Fig. 5-4c compares the time cost of our TSP scanning method with the conventional S-shaped scanning method. Specifically, when k=20 (one layer of the vase), the scanning speed can be improved by a factor of 1.75. For the case in Fig. 5-4b (k=6), the printing speed is 3 times faster than the S-shaped method. This methodology highlights the printer's capability to rapidly produce large-scale, high-resolution, hollow structures.

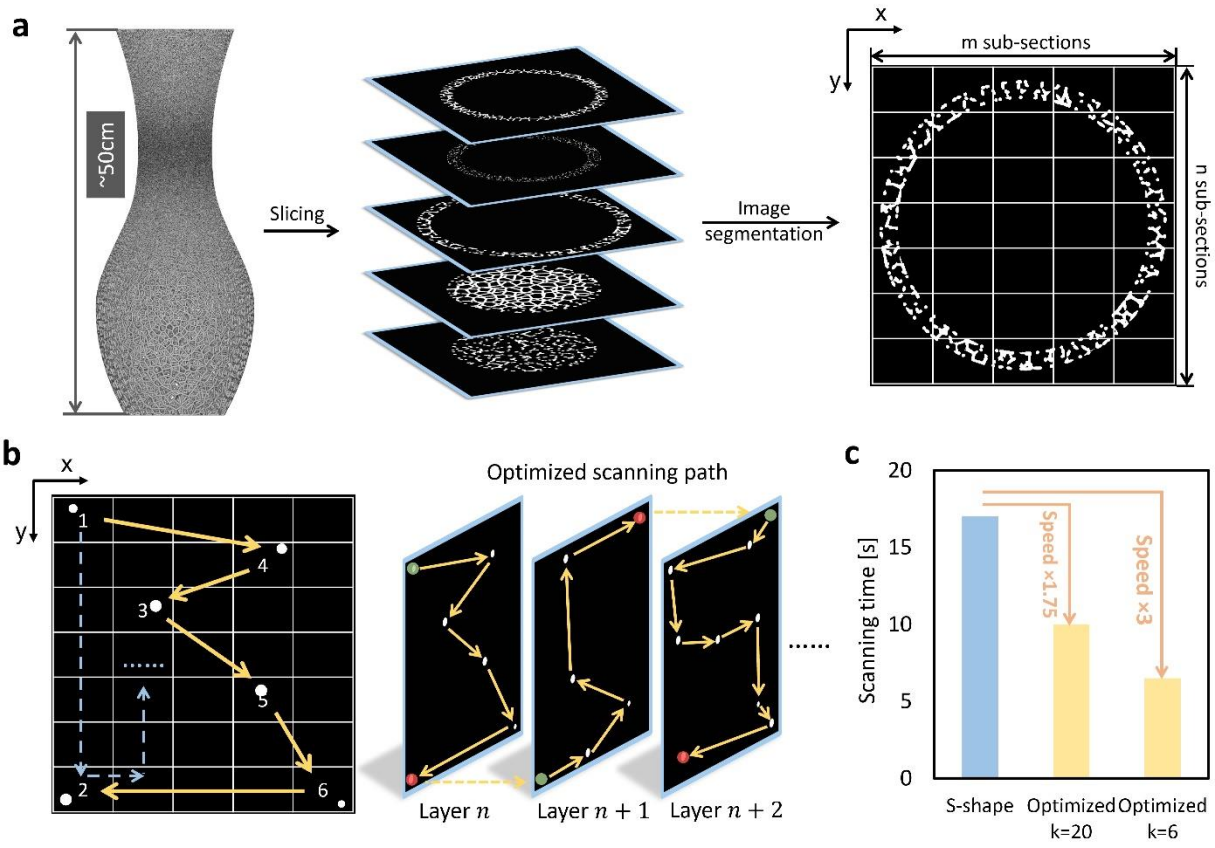

Figure 5-4 Scan path optimization process for the system. (a) A large-scale (50 cm), high-resolution (50 μm) vase is designed in nTopology and is sliced into layers. Each layer is split into 5×7 sub-sections. (b) An illustration outlining the optimization of the scan path. The dotted blue lines refer to the conventional S-shape scanning method, and the solid yellow lines refer to the optimized scan path using the TSP solver. For layer n, the scanning starts at the green dot and ends at the red dot. For layer n+1, the scanning starts from the endpoint of the previous layer, and so on. (c) The scanning time cost between the conventional and optimized paths is compared, with k=20 indicating the number of valid images in a single layer of the vase slice and k=6 indicating a general slice image in Fig. 5-4b. The optimized scan path greatly reduces the scanning time required to produce the large-volume structure with a hollow interior.

5.2.3 Fabrication of large-scale high-resolution CFRP lattice structures

Printing large-scale structures using a bottom-up system poses a significant challenge in controlling the separation force between the newly cured layer and the surface of the film. This

separation process is akin to a vacuum, which can cause the resin to fill the gap. The pulling force has significant impacts on several aspects of the printing process, including the printing time, the lifespan of the separation window, and the available material choices. Numerous research studies have been conducted to investigate the correlations between various process parameters, and it has been concluded that the separation force is strongly influenced by factors such as the contact area, resin viscosity, exposure energy, and separation speed [55, 99-102]. For this study, the separation speed during the initial peeling process was intentionally set to a low value of 0.2 mm/s to ensure proper detachment, and two powerful linear stages were utilized to provide enough lift force for the process.

With the developed printer, we have managed to print lattices with CFRP with an overall size of 10-50 cm, as shown in Fig. 5-5. Fig. 5-5a features a group of hierarchical CFRP lattice material, which is comprised of the octet of octahedra trusses. The sample has an overall size of 18 cm, with strut radii as thin as 150 μm. Such a group of materials exhibits nearly isotropic properties and has high structural connectivity within stretch-dominated architectures. Fig. 5-5b demonstrates the 3D printing of a group of plate-lattice materials using CFRP, which features a more efficient architecture with higher energy absorption capability compared to truss-lattices. In Fig. 5-5c, we present the fabricated Voronoi vase, measuring up to 50 cm in length and with a minimal strut thickness of 50 μm, demonstrating our printer's ability to produce large-scale high-resolution objects.

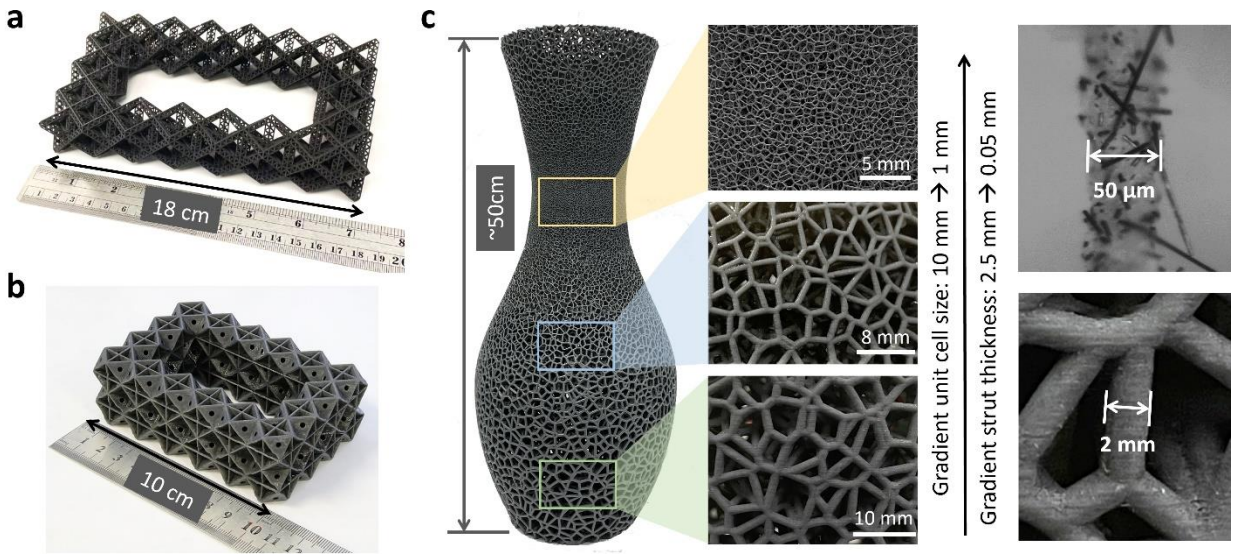

Figure 5-5 Fabricated samples using the large-scale high-resolution PSL system. (a) As-fabricated large-scale hierarchical CFRP truss-lattice materials (strut radius=150 µm). (b) As-fabricated CFRP plate-lattice materials. (c) As-fabricated large-size high-resolution Voronoi vase made of CFRP. The vase is designed to have gradient unit cell size and strut thickness along its height direction.

5.3 Design and manufacturing of a bio-inspired lightweight car bumper energy absorber

5.3.1 Design of the energy absorber

Traditionally, reducing the mass of structural systems and enhancing the energy dissipation of materials have been the subjects of the automotive industry over the years [103]. CFRP is known for its high stiffness-to-weight ratio and hence is of interest in extensive research and industrial uses. Incorporating CFRP in AM provides further opportunities for significant weight reduction [104]. Benefiting from the advantages of AM for free-forming, it is possible to manufacture

components with complex internal structures to meet specific energy absorption requirements [105].

To further demonstrate the capability of the developed system, we designed and manufactured a lightweight car bumper energy absorber, as illustrated in Fig. 5-6. The design of the energy absorber was inspired by the intricate structure of cortical tissues of maize stems, where the thickness and size of cells vary at different locations of the tissues, resulting in efficient energy absorption (Fig. 5-6a). By utilizing the free-forming capability of AM, we were able to replicate this structure in the design of the energy absorber for the vehicle application. The absorber consists of two layers of a stair-like structure with a length of approximately 110 cm.

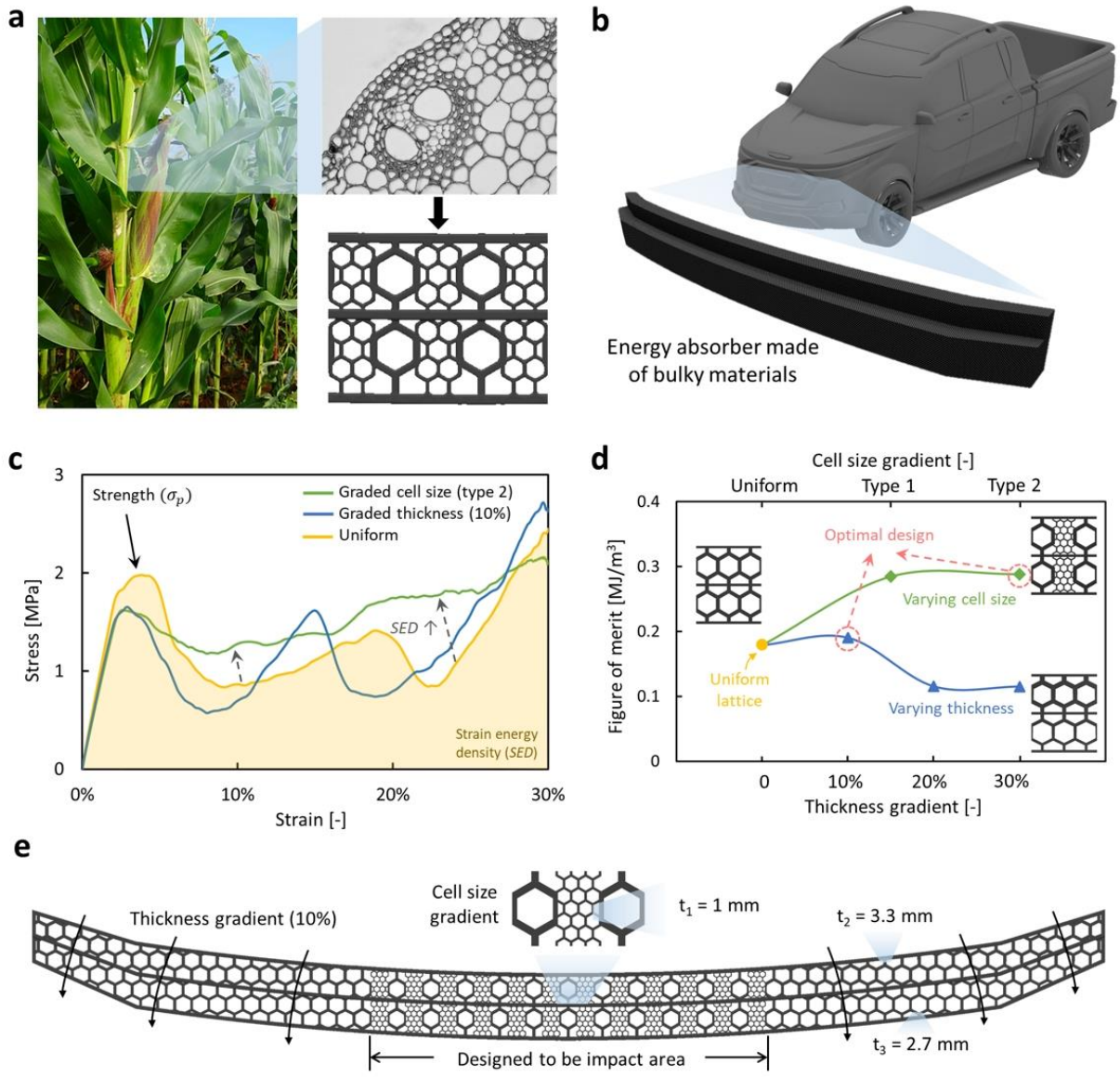

Figure 5-6 Design of the car bumper energy absorber. (a) Maize stem and its single-layered cortical tissues under the microscope. The structure shows that the tissue is composed of graded cells with varying wall thicknesses and cell sizes. (b) Schematic of a conventional car bumper energy absorber made of bulky materials. (c) Quasi-static stress-strain response of the representative honeycomb design under compression obtained through simulations. (d) The figure of merit for the honeycomb structure with graded thickness and unit cell size is displayed, highlighting the optimal design. (e) Designed lightweight bumper energy absorber that features gradient wall thickness and unit cell sizes.

We incorporated hexagonal honeycomb structures, which are well-studied for their energy absorption properties, as the inner filler, while retaining the outer shell to effectively distribute the load (outer shell dimension provided by Ford Inc.). To further enhance its performance, we introduced two topological gradients to the honeycomb structure: thickness gradient and unit cell size gradient. The effect of these two gradients was studied in numerical simulation in Abaqus. Fig. 5-7 presents the stress-strain curve of the CFRP composite that was utilized for the bumper energy absorber. In the simulation, we adopted an elastic-plastic model as the base material property. The material was tested to be isotropic, and its Poisson's ratio is 0.3.

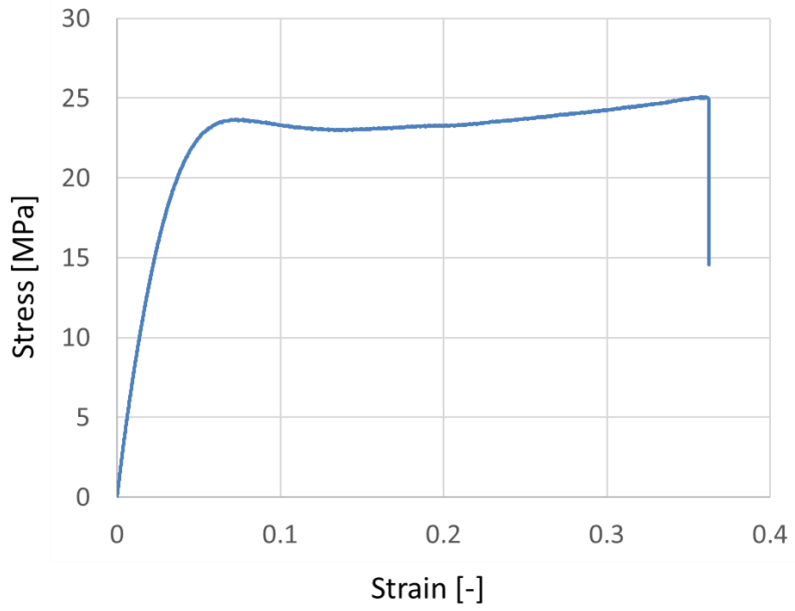

Figure 5-7 The stress-strain curve of the CFRP composite used for energy absorber.

Fig. 5-6c shows the stress-strain curves of three representative honeycomb lattice configurations, where the yellow line corresponds to the baseline design with uniform thickness and cell size. Here,

we investigated two critical parameters: peak stress (strength σ_p) and strain energy density (*SED*), which was calculated as the enclosed area of the stress-strain curve and had a unit of MJ/m^3. Notably, the uniform lattice exhibited global buckling, with two layers buckling simultaneously. After the first peak, a prolonged plateau was observed, followed by a drop, signifying the collapse of one layer.

By introducing thickness gradients with an offset of 10% (varying from 90% to 110%), we were able to obtain the blue stress-strain curve shown in Fig. 5-6c. As a result, the peak stress of the graded lattice was lowered by 17%, from 1.98 MPa to 1.65 MPa, compared to that of the uniform lattice. Moreover, we observed a higher second peak stress in the stress-strain curve, which resulted in an increase in the volumetric energy absorption at approximately 15% strain. This was because the top layer had lower strength, which buckled first before the buckling of the second layer with a thicker wall. This sequential buckling mechanism differed from the uniform lattice buckling and contributed to enhanced energy absorption.

The green line in Fig. 5-6c illustrates the stress-strain curve of the lattice with graded cell size, which exhibits an even higher strain energy density. This improvement is attributed to the local buckling of the small unit cell members of the lattice. Specifically, the small cells gradually buckle and collapse until the larger cells fail. This local buckling provides a more steady stress level after the peak stress, resulting in a higher average plateau stress level and thus providing additional energy absorption capacity.

It is worth noting that even though the designs in Fig. 5-6c have different geometries, they all have the same relative density. Therefore, a fair comparison can be made between them based on the

plotted stress-strain curves. It is evident that higher energy absorption is always desirable, while lower peak stress is preferred as the stress will ultimately be transferred to the vehicle body or the object that was impacted. To further evaluate the performance of each design, we defined a figure of merit that accounts for both *SED* and peak stress using the equation: $FOM = SED - w_i\sigma_p$, where σ_p is the strength of the structure, w_i is a weight factor. In this study, we set w_i to 10% and utilized this equation to identify the optimal design for the specific application scenario. A higher *FOM* value indicates better performance for a given design.

As shown in Fig. 5-6d, we further evaluated multiple designs with different configurations by manipulating the gradient value and plotted their corresponding figure of merit values. Our findings indicate that introducing either a thickness gradient of 10% or varying cell sizes can improve the *FOM*. Based on these results, we identified the optimal design that maximized the *FOM* and generated the final design by superimposing these two gradients into a single design volume. As depicted in Fig. 5-6e, we specifically designated the middle section of the absorber to serve as the impact area, which was filled with graded unit cell sizes to enhance its energy absorption capabilities. In addition, we applied a thickness gradient of 10% along the width direction to induce sequential buckling in the remaining areas of the absorber. The absorber spans roughly 110 cm in length and stands 13.3 cm wide and 10.2 cm tall, with the thinnest plate measuring only about 1 mm thick.

5.3.2 Fabrication of the energy absorber

To accommodate the size of the vat, the entire absorber was divided into four parts, and we printed two parts simultaneously, as illustrated in Fig. 5-8a. Each sliced layer consisted of 3×5 sub-images.

In Fig. 5-8b, the absorber is shown to be printed using CFRP resin. The small honeycomb lattices in the zoomed-in photo demonstrate a satisfactory alignment between two bridging sub-sections. After the printing, the support structure was removed, and the absorber was post-cured. The four parts were then assembled using J-B Weld ClearWeld glue, as shown in Fig. 5-8c. The printing resin is formulated with 1wt% loading of short carbon fibers, which contributes to its excellent stiffness and toughness during tensile testing. Such an absorber has a relative density of only ~40%, while it has optimized energy absorption capability. The bumper energy absorber designed and printed has an exceptional property of efficiently absorbing significant amounts of energy while maintaining a relatively lightweight structure. This property provides a crucial advantage in the automotive industry, where utilizing lightweight materials can enhance fuel efficiency and minimize emissions.

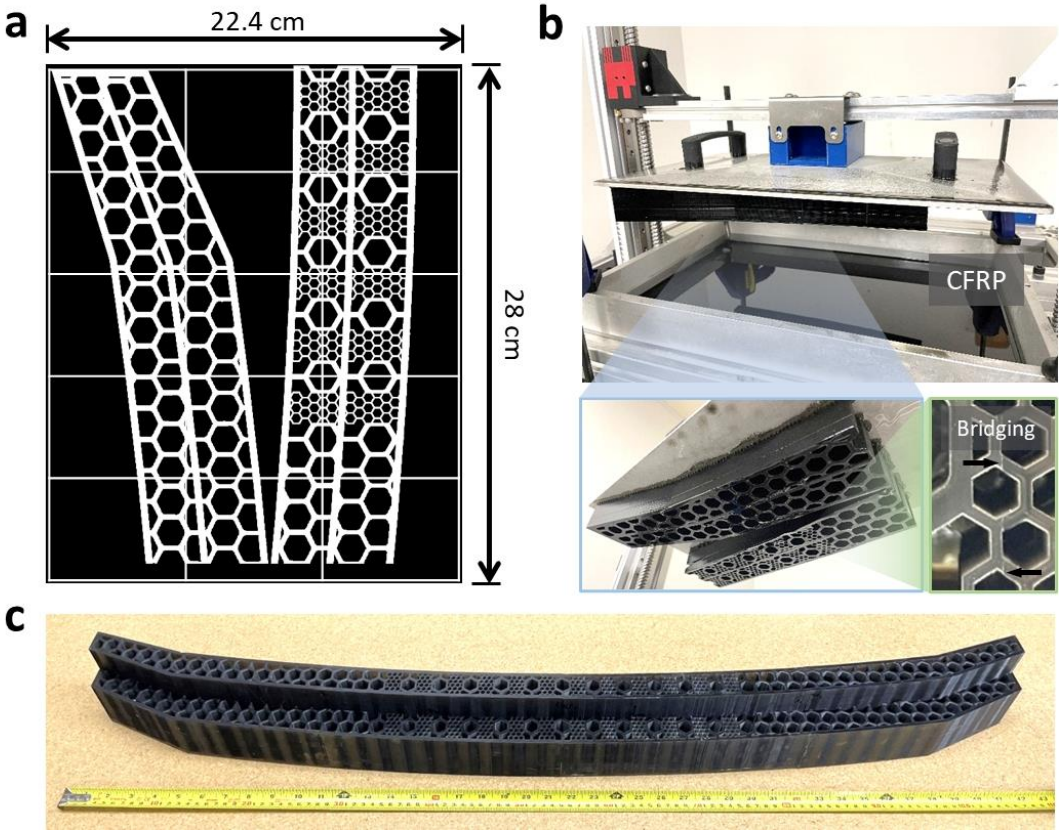

Figure 5-8 Fabricated car bumper energy absorber. (a) The printing area is divided into 3×5 sub-sections, with a total size of 22.4×28 cm².(b) Two parts of the energy absorber are being printed simultaneously in one batch. (c) As-fabricated large-scale car bumper energy absorber with a length of 110 cm, width of 13.3 cm wide, and height of 10.2 cm.

5.4 Design, printing, and testing of high-strength CFRP plate-lattices

In chapter 3, the author presented a scalable multi-material stereolithography process, which enabled us to manufacture a group of three-dimensional truss-lattice that simultaneously exhibits high stiffness and damping. However, such a structure is incapable of achieving the theoretical upper bound. In this section, we introduce an isotropic cubic+octet plate-lattice design, as shown in Fig. 5-9a. Such a design has higher stiffness per unit weight than truss-based lattices, resulting

in better mechanical performance. The plate is designed with small holes to remove the resin trapped in the compartment. The designed plate lattices were then fabricated using the large-scale high-resolution system. As shown in Fig. 5-9b, the 4×4×2 lattice weighs only 20g, while it can withstand the weight of an adult, which is ~4,000 times its weight. Through calculation, the specific strength of such a lattice is larger than 1.2 kPa/(kg/m^3), with a density of only 185 kg/m^3.

Structures with a range of relative densities with a side length of 2 cm are fabricated to experimentally characterize the lattices' mechanical performance (Fig. 5-9c). Unidirectional compression tests were performed to obtain the stress-strain curves of the samples, and Young's Modulus was determined accordingly. We observed that the stiffness of the printed plate-lattice structures increased monotonically with an increase in relative density. In fact, when compared to their previous study on octet-truss structures, the plate lattices exhibited a dramatically higher normalized stiffness at a given relative density (as shown in Fig. 5-9d).

In order to verify the experimentally measured results and understand the underlying fracture mechanisms enabled by the unique design, numerical simulations were implemented in commercial finite element software (Abaqus). Compressive stress-strain curves of the CFRP cubic+octet plate-lattices, obtained from the simulations (see the detailed material models and boundary conditions in our JMR paper), for relative densities of 10, 20, 30% are shown in Fig. 5-9e. Then, we captured the ultimate strength of the stress-strain curve until fracture. It is found that the ultimate strength increases with the increase of relative density while the fracture strain remains the same. In Fig. 5-9f, we normalize the ultimate strength with the lattice density, and the results show that such a group of plate-lattice have a specific strength of ~6.2 kPa/(kg/m^3) with a density

of less than 400 kg/m^3, making them an excellent candidate for a strong, lightweight material for impact isolation and energy dissipation.

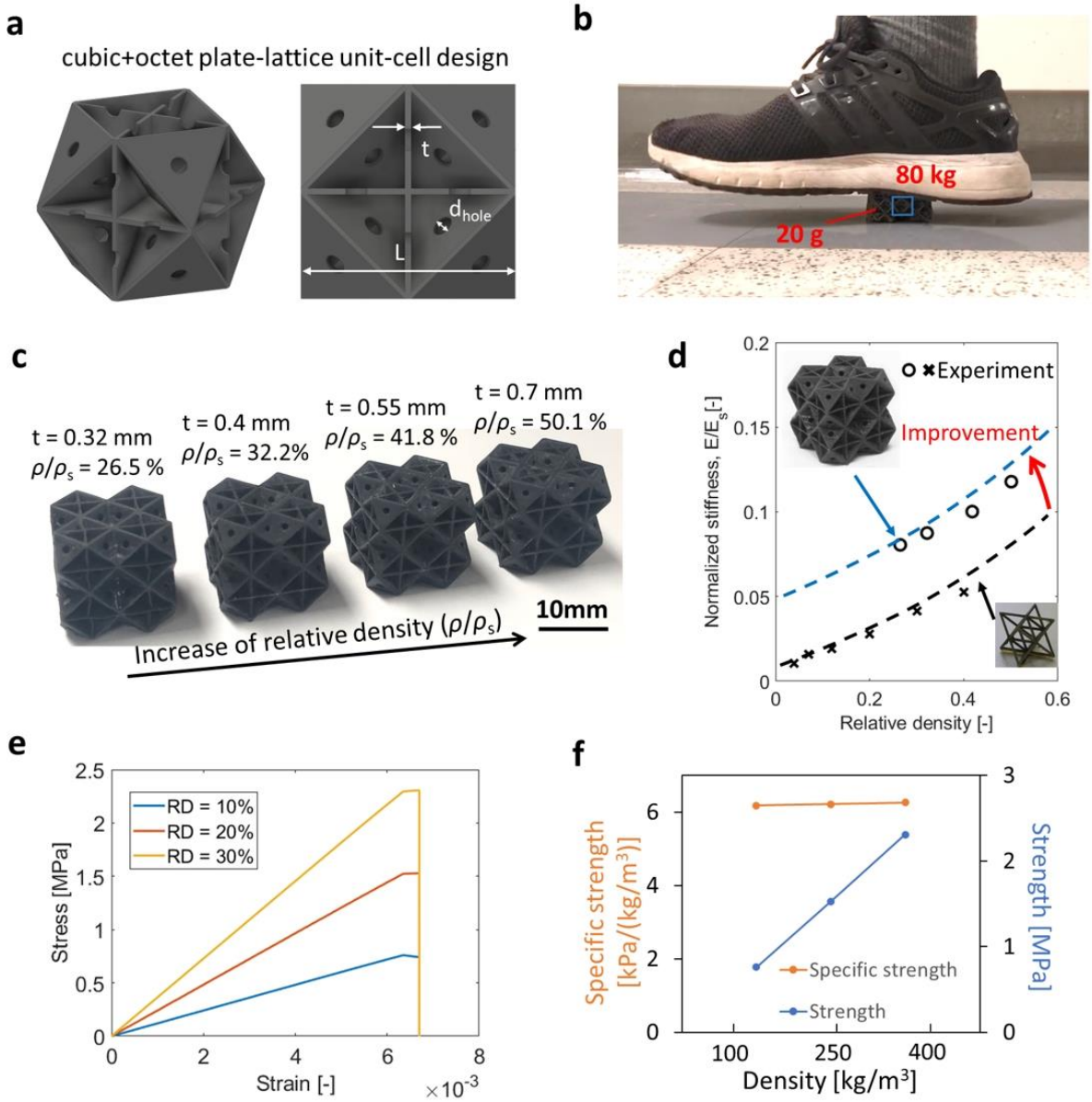

Figure 5-9 Design, printing, and testing of high-strength CFRP plate-lattices. (a) Unit-cell design of plate-lattice. (b) Demonstration of the high strength of the cubic+octet plate-lattice (4×4×2). The lattice weighs only 20g, and it can withstand the weight of an adult. (c) As-fabricated plate-lattices with a range of relative densities. (d) Comparison of the normalized stiffness between

plate-lattices and octet-truss lattices with different relative densities. (e) Simulated compressive stress-strain curves of the cubic+octet plate-lattices for different relative densities, $\bar{\rho}$=10, 20, 30%. (f) Ultimate compressive strength and specific strength of the plate-lattices (The data points correspond to the simulated cases in figure e).

5.5 Integrate multi-extrusion nozzles for multi-material printing and its potential application

5.5.1 Integrate multi-extrusion nozzles to the large-scale high-resolution PSL system

There have been significant efforts in the scientific community to fabricate multi-material architectures through PSL [49, 106]. The potentials of these multi-material AM technologies allow for extending the design space beyond the complex geometries of a single material. However, most of the reported techniques are limited to a small printing area (<40 mm) due to the trade-off between resolution and printing size. In this section, based on the system proposed above, we developed a material exchanging system for large-scale multi-material printing for CFRP composite with high resolution and multi-material compositions.

Fig. 5-10a and 5-10b illustrate the custom multi-material channels that were designed to enable the switch of resins and ethanol during the printing process. Peristaltic pumps, pipes, and nozzles were utilized to extrude multiple resins, with the locking gate lifting to allow for the flow of new material into the recycling vat. To prevent contamination between resins, ethanol was utilized to clean uncured resins from the solidified parts and printing vat, followed by air blowing to dry any residual ethanol. The process was repeated layer by layer, combining multiple materials into a 3D structure. While peristaltic pumps provided sufficient pressure for resins with high fluidity,

clogging or insufficient pressure could occur when processing highly viscous resins mixed with carbon fibers. As a solution, a ram extruder kit (Fig. 5-10c) was integrated into the system to provide higher extrusion pressure. Additionally, different nozzle geometries were printed and tested for the optimization of different materials. Fig. 5-10d showcases an as-fabricated large multi-functional material sample, selectively deposited with a copper layer based on CAD design, serving as a transmitarray (3D antenna).

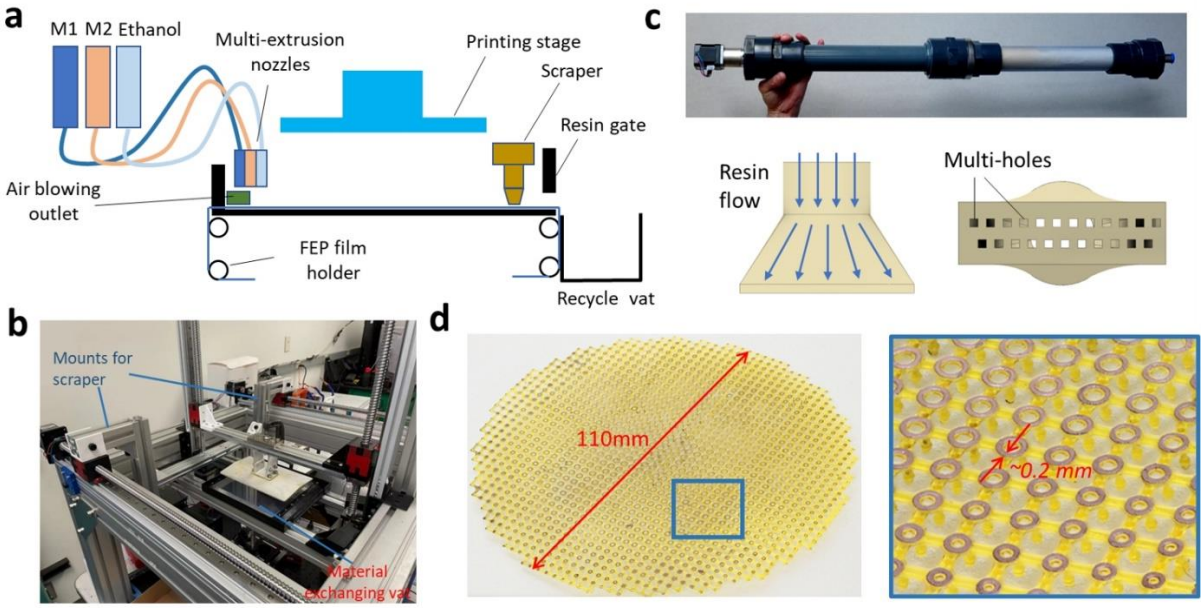

Figure 5-10 Integrate multi-extrusion nozzles to the large-scale high-resolution PSL system. (a) Schematic of the multi-material exchanging system, cleaning system, and resin recycling system. (b) The overall system setup. (c) Ram extruder and custom extrusion nozzles with multi-outlets. (d) A large antenna array made of two different resins and copper was deposited onto the charged resin.

5.5.2 Design, fabrication, and evaluation of stiff, strong, and lightweight bi-material sandwich plate lattices with enhanced energy absorption

3D-printed CFRP lattices are known for their high stiffness-to-weight ratio. However, achieving high stiffness, strength, and energy absorption simultaneously in single-material lattices is challenging because even the most mechanically efficient topological designs (stretching-dominated, with the highest possible Young's modulus and strength [107]) would fail prematurely at small strain through fractures or post-yield softening. Although interpenetrating phase composites [108-110] (with stiff and soft material phases) have shown to be effective in improving energy absorption while maintaining stiffness and strength, they typically come with a significant increase in mass, which can be a disadvantage in weight-sensitive applications.

Based on the previous work, we designed a novel isotropic cubic+octet plate-lattice by applying the two material phases (CFRP and soft phases) directly into the lattice topology via a sandwich plate configuration [68, 111-113] (CFRP-soft-CFRP plies), hence improving the energy absorption and maintaining the stiffness and strength with almost no change in its mass (Fig. 5-11a). Such a configuration allows both stiff and soft material phases to exploit the stretching-dominated lattice topology while potentially enhancing the energy absorption from the unique synergy of the constituent materials.

We evaluated the energy absorption (area under the stress-strain curve) of the designed bi-material isotropic cubic+octet plate lattice as a function of the volume fraction of the soft phase via finite element simulations. Fig. 5-11c shows the local maxima of the absorbed energy at specific volume fractions of the soft phase for different relative densities. We found that the maximum absorbed

energy obtained from all modeled relative densities was improved by approximately a factor of 2.5 compared to plate lattices entirely made of the CFRP phase. We also evaluated our plate lattices against previously reported, carbon-based architected materials to assess their energy performance (Fig. 5-11d). Our bi-material plate-lattices show favorable strength-energy absorption characteristics against recently reported two-phase CF octet-truss (in $(U/E_s)/\bar{\rho}$ of 190% and in $(\sigma_{peak}/\sigma_{ys})/\bar{\rho}$ of 140%), making them an excellent candidate for a stiff, lightweight material for impact isolation and energy dissipation.

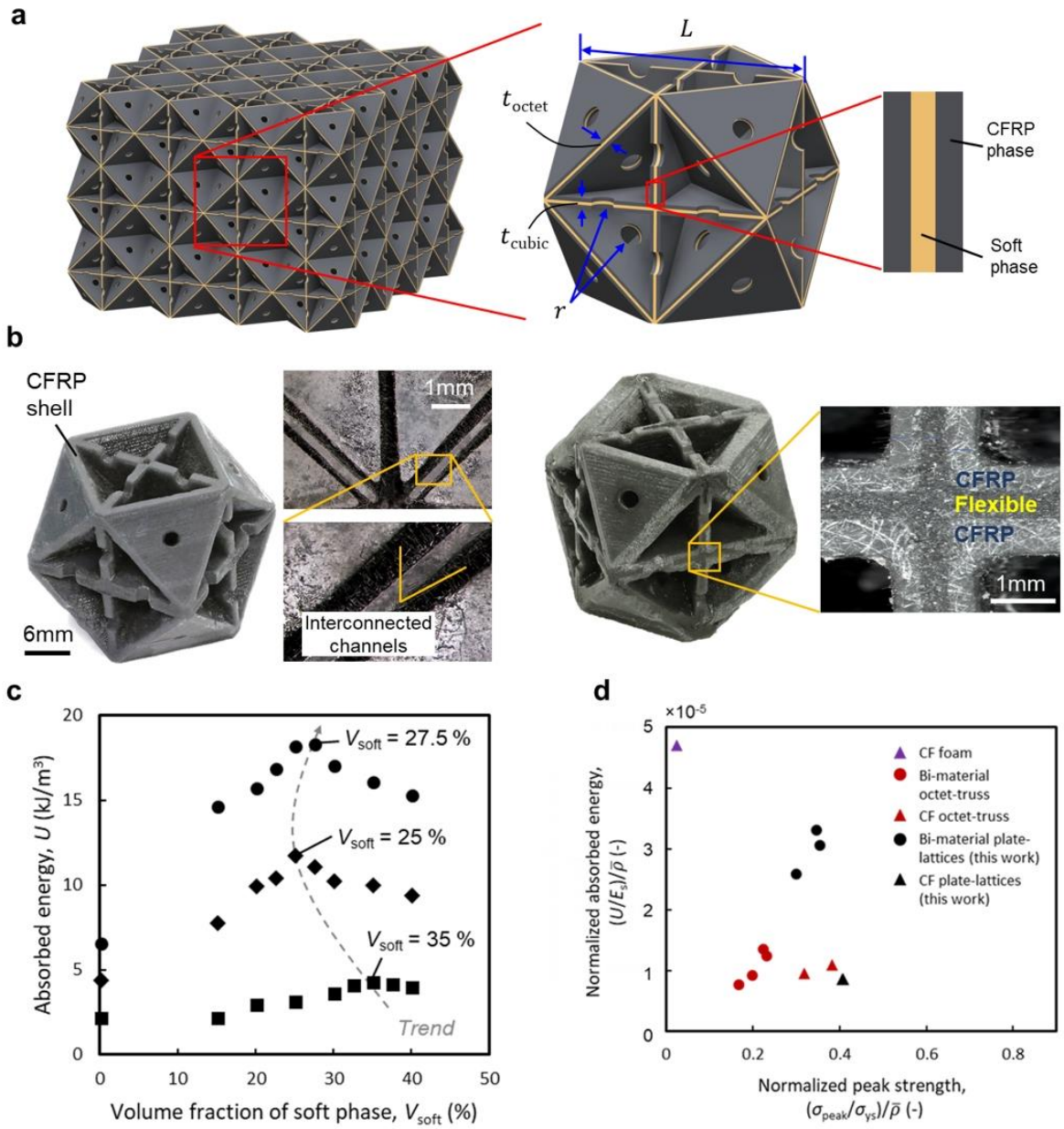

Figure 5-11 Design, fabrication, and evaluation of bi-material isotropic octet+cubic plate-lattice. (a) Each plate is designed as a sandwich plate (CFRP-soft-CFRP). (b) Post-thermal curing fused the soft-stiff phase. The unit cell has a relative density of 30%. (c) The absorbed energy, U, under compression of bi-material isotropic cubic+octet plate-lattices having different volume fractions of the soft phase for several relative densities. (d) Assessment of energy absorption performance against previously reported materials. CF and bi-material octet-truss adopted from Ref. [1]. Carbon foam adopted from Ref. [114].

5.6 Integrate material dispensing system to control fiber alignment

Incorporating fiber alignment can further enhance the properties of the CFRP composite. Therefore, the author proposes combining the large-scale high-resolution SPSL system with a fiber dispensing system to achieve controlled carbon fiber orientations and micro-scale critical feature sizes beyond current 3D printing techniques.

5.6.1 Material preparation and alignment mechanism

To fabricate composites with controlled fiber orientation, we first create printing inks that embody the essential rheological properties required for our 3D printing method. Specifically, we formulate the printing ink using a commercial UV-curable resin Rigid 10k, short carbon fibers, and silica nanoparticles. The high aspect ratio carbon fibers align under the shear and extensional flow field that develops within the nozzle during the printing, resulting in enhanced stiffening in the cured composite along the printing direction. The silica nanoparticles primarily serve as a rheology modifier that imparts shear-thinning behavior and shear yield stress to the ink [115].

The printing resins are prepared by mixing a UV curable matrix (Rigid 10k, Formlabs, Inc.) with appropriate amounts of milled short carbon fibers (7 μm in diameter, ~70/315 μm mean length, E&L Enterprises, Inc.) and silica nanoparticles (TS 720, Cabot, Inc.).

Batches started with 100 g of Rigid 10k resin. Milled carbon fibers are added in 2.5, 5, 10, or 15 g increments, followed by 1 hour of mixing on a roller (Fisher Development, Inc.). Next, 3.5 g of silica nanoparticles are added, followed by manually mixing in a container. Finally, the resin is thoroughly mixed using the roller for 24 hours.

The rheological behavior of inks of varying compositions was measured using an AR-G2 rheometer. A parallel plate fixture (diameter: 25 mm) was used with a test gap of 500 μm and a shear rate of 1 rad/s - 100 rad/s. The pure matrix resin exhibits a complex viscosity (η) of ~1.8 Pa·s that is almost independent of the shear rate. As a result, the resin flows easily through the nozzle at moderate application pressure and immediately wets and spreads as it leaves the nozzle, unable to support itself. In contrast, the resin becomes a shear-thinning fluid with the addition of carbon fibers and nanoparticles. The resulting resin has a low viscosity at high shear rates and high viscosity at low shear rates, making it flow only when extruded. Besides, given their solid-like nature in the quiescent state, the filler within the inks undergoes minimal aggregation or sedimentation, making them ideal for 3D printing that lasts for weeks [115].

5.6.2 Fiber alignment evaluation

Fiber alignment properties were studied by analyzing the captured images using the open-source software ImageJ. Firstly, an "Auto Local Threshold" plugin was used to highlight the fibers, followed by filtering background noise via a "Trainable Weka Segmentation" plugin. The processed image contains most of the useless information removed except for the fibers. Then, the image was analyzed by the "Directionally" plugin based on the Fourier spectrum. Fiber orientation information can be extracted from the software accordingly. A parameter, Herman's orientation parameter f_p, that quantifies the orientation quality could be calculated from the extracted data via the equation: $f_p = 2\int_{-\pi/2}^{\pi/2} cos^2\phi n(\phi) d\phi - 1$, where $n(\phi)$ is the orientation distribution function [116, 117].

5.6.3 System setup

Our 3D printing method combines the advantage of direct ink writing (DIW) and PSL. As shown in Fig. 5-12a, the nozzle extrudes resin in the vat with predefined toolpaths, enabling localized 2D fiber alignment. Unlike regular DIW, which uses extruded beads to compose the structure directly, our approach is to solidify the extruded resin onto the printing platform through moving optics. Therefore, the resolution of the printed feature depends on the optical system involved rather than the nozzle size, which makes the smallest printable feature size less than 50 μm (the optical system is the same one used above) [1, 96]. Fig. 5-12b shows an actual photo of the printing system integrated with the extruder and its motion system. The extrusion system consists of a plunger extruder providing external pressure using a motorized piston and an auger extruder that assists in extrusion (StoneFlower 3D, Inc.). The motion axes carry the augur extruder to deliver the resin across the vat.

The diagram (Fig. 5-12c) shows the processing and control schematic of the printing system. The process starts with a 3D model. Using a regular FDM printer slicer, the toolpath Gcode for extruder movement and dispensing was generated, while using Netfabb and Matlab, 2D images and Gcode for curing were created. The extrusion g-code is saved into an SD card and will be read by micro-controller Duet 2 directly, while the sliced images and scanning g-code will be entered into the LabVIEW program. The LabVIEW program sends commands to the microcontroller boards via USB to control all the motors. The different color of the lines indicates various controlling/processing signals. Blue line: File processing; Red line: 24V power circuit; Green line:

Analog or digital signals; Yellow line: Power circuit for motors. A custom LabVIEW program was developed to integrate all the functions into one system.

The printing process begins with the delivery of printing ink over the entire printing area, allowing for localized fiber orientations. Then, the platform moves down, sandwiching the resin between the printing platform and the vat bottom, followed by optical system movement. The optical system cures resin onto the printing platform with specific patterns. Finally, the platform moves up, and the extruder delivers the resin for the next layer. The process was repeated layer by layer, combining them into a 3D structure.

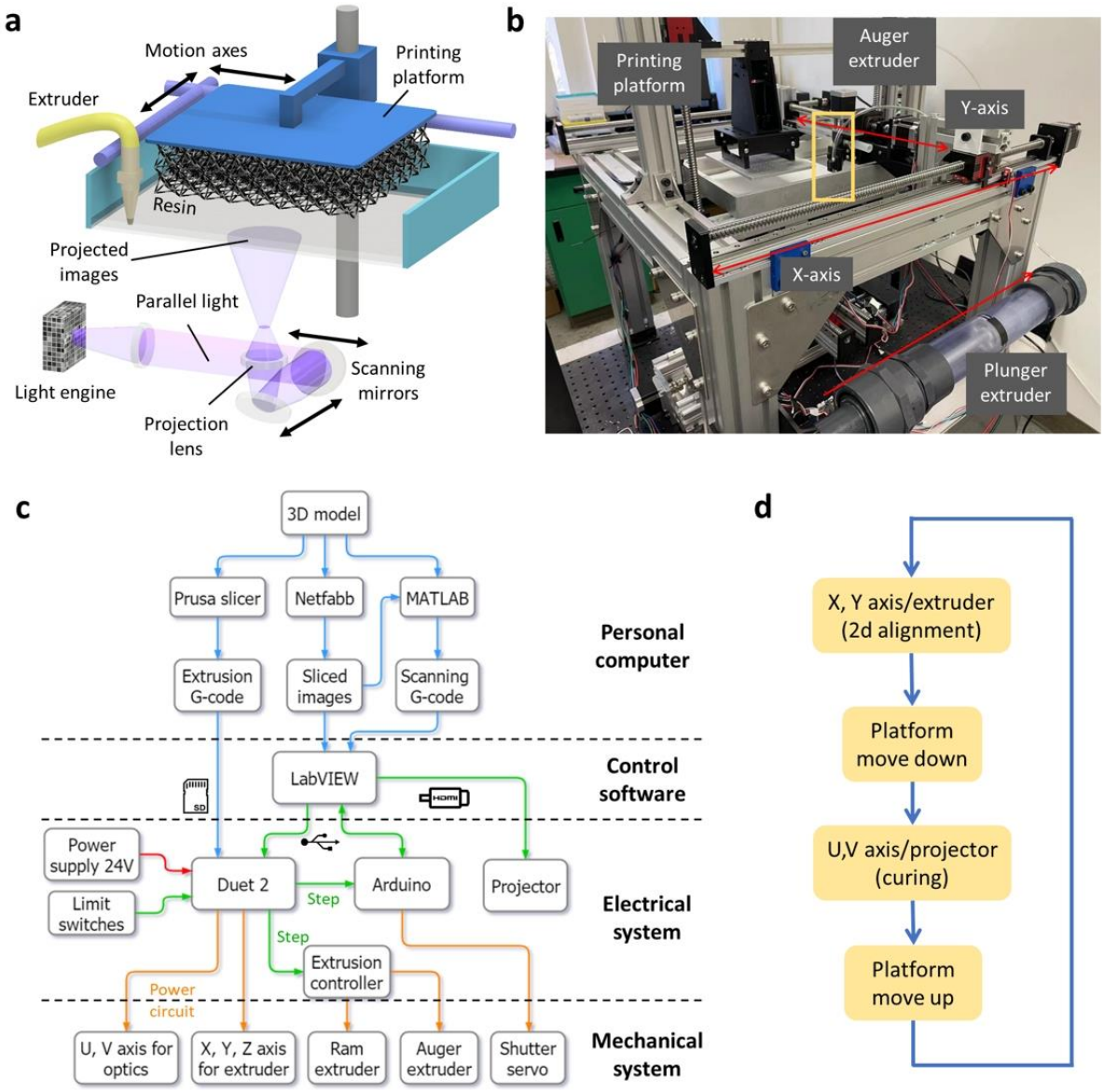

Figure 5-12 Schematic of the printing system and controlling diagram. (a) Schematic of the printing system integrated with scanning optical and material delivery systems. (b) Photo of the printing system. (c) Block diagram of the processing and control schematic. (d) Diagram of the printing process.

5.6.4 Mechanism of fiber alignment

Plenty of literature has studied the fiber alignment mechanism in a nozzle. Different from other works, the extruded beads maintain their shape after extrusion; our method incorporates an additional compression process upon beads before curing. During this process, the beads are sandwiched between the vat and build platform, causing the resin to deform slightly and spread the bead out along its lateral side. However, this could potentially affect the alignment of the fiber. To strictly control the spreading process and minimize dislocation of the fibers, the bead's shape shall match the layer thickness (t, the distance between the vat and the platform), as shown in Fig. 5-13b. In this work, flat beads are preferred over oval beads because of less deformation upon compression. The extruded bead's shape can be controlled by adjusting the flow rate and the gap (d, Fig. 5-13a) between the nozzle and vat. A compression speed of 0.5 mm/s and a layer thickness of 0.1 mm was applied during printing. Slow speed ensures the resin deforms at a low shear rate, keeping the fiber orientation constant during resin spreading. Selected small layer thickness ensures UV light penetrates the resin to be cured onto the platform.

Fig. 5-13c compares the fiber alignment quality with and without the compression process. The photos are captured using a regular optical microscope and processed using ImageJ. Herman's orientation parameter of the two cases was calculated accordingly. We found the fiber orientation quality slightly deteriorate after compression due to lateral shear flow, but the difference is not significant (f_p = 0.54 vs. f_p = 0.44, without and with compression). Using the system, we printed part of a hollowed car bumper energy absorber design, as shown in Fig. 5-13d.

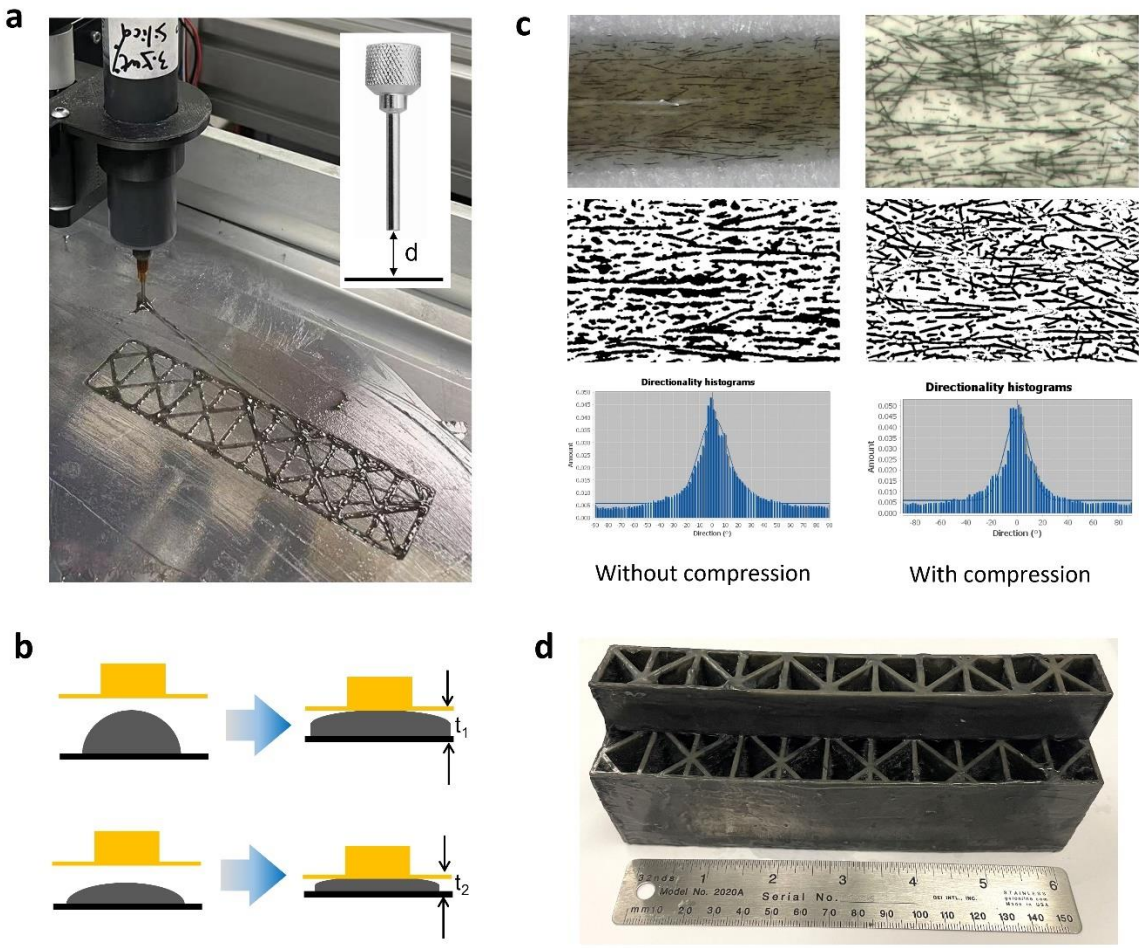

Figure 5-13 Testing and evaluation of fiber alignment of extruded CFRP beads. (a) Extruded pattern with programmed fiber orientations. (b) Schematic of the compression process of beads with an oval and flat shape. (c) Captured images from cured beads before and after compression. The histogram shows the fibers' orientation distribution. (d) Printed hollowed car bumper energy absorber with localized fiber orientation.

5.6.5 Characterization of the material property

Dog bones with a range of fiber loading and fiber length are fabricated to experimentally characterize the base material's mechanical performance. Unidirectional tensile tests were performed to capture the stress-strain curves of the samples, and their stiffness was measured

accordingly, as shown in Fig. 5-14a. We observed that the measured stiffness increases monotonically with an increase in fiber loading. Compared to the 70 μm, 315 μm length fiber provides more reinforcement to the composite. Fibers within CFRP resin that contain over 10 wt% 315 μm fibers tend to aggregate, making the resin extremely viscous so that it cannot be extruded. Therefore, there is no testing data for resins having fiber loading greater than 10 wt% with 315 μm fiber length. Moreover, the material exhibits higher stiffness and strength when there is fiber alignment. Specifically, with aligned 315 μm fiber, the CFRP achieves a stiffness of 6.6 GPa, which is superior to other reported fiber-reinforced composites printed by PSL shown in Fig. 5-14b [118-121]. The stiffness was achieved not only by the nature property of the matrix material but also by the reinforcement of the fibers. Literature reports 3D printed CFRPs with stiffness larger than 10 GPa, while those lattices usually have a low resolution (> 0.4 mm), depending on the nozzle size [115, 122]. Theoretically, the method proposed in this work can achieve a printing feature size of less than 50 μm.

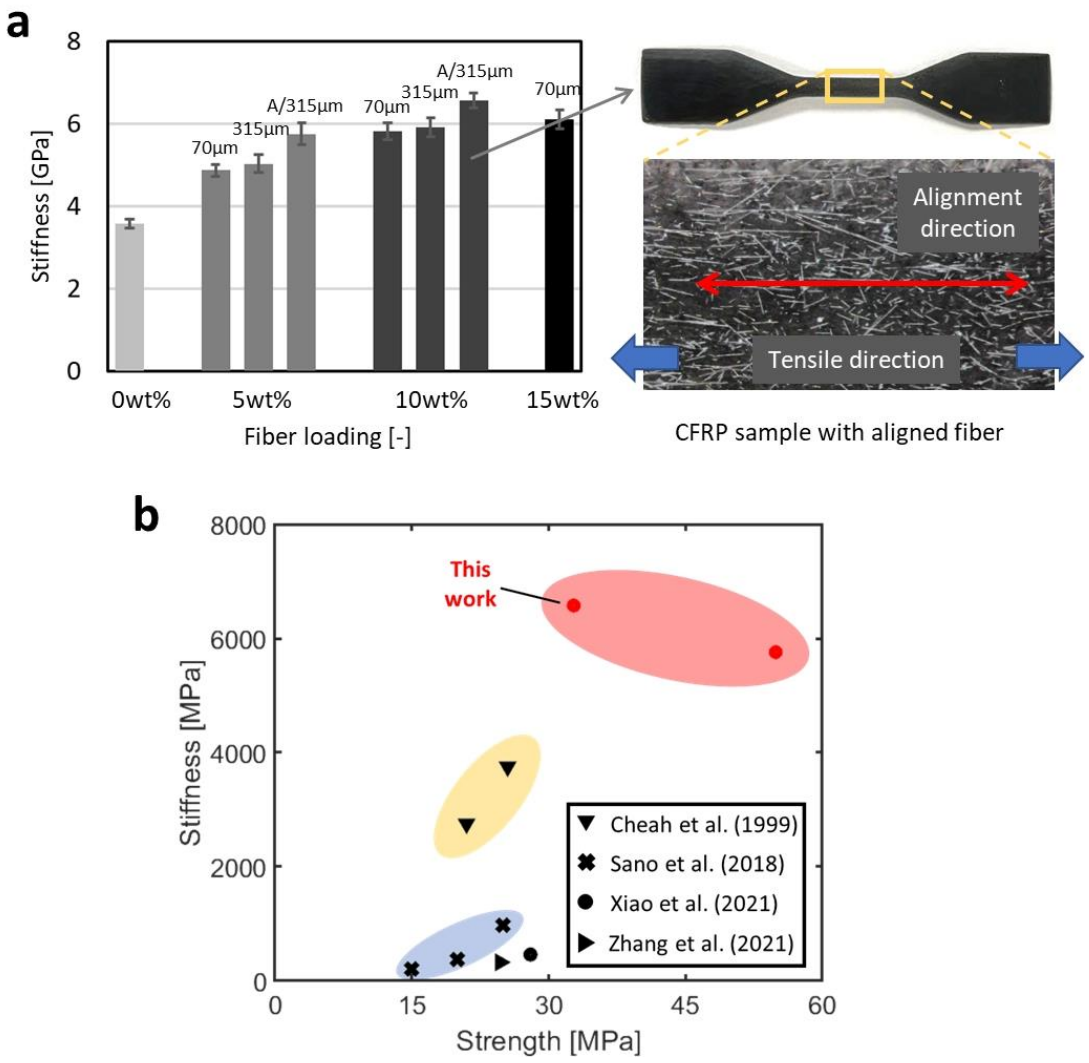

Figure 5-14 Mechanical properties of the CFRP composites with and without fiber alignment. (a) Measured Young's Modulus of printed CFRPs with varying fiber loading and lengths. (b) Mechanical property map of fiber-reinforced composites printed via PSL [118-121].

5.7 Discussion and conclusion

When comparing the resolution of the printer developed in this work to other popular AM methods [123], such as fused deposition modeling [124-126], material jetting [127-129], and SLS [130,

131], it's worth noting that our system boasts a high printing resolution of 50 μm (Fig. 5-15). While other projection-based stereolithography systems can achieve higher resolutions in the range of 5-100 μm [58, 132-134], the printing resolution of our system at 50 μm is still competitive with most other SLA systems. Although two-photon polymerization (TPP) can achieve even higher resolutions at a scale of 100 nm compared to other AM techniques, its limited building area makes it challenging to implement in real-world applications [135-137]. Another significant advantage of our printer is its ability to produce large objects, with printing sizes reaching up to tens of centimeters. This is a notable improvement compared to many other AM methods that have limitations on the size of the objects that can be produced, often due to the size of the build chamber or limitations of the printing process itself. In summary, our printer offers a high printing resolution of 50 μm while also enabling the production of larger objects, making it a competitive option among other popular AM methods.

As we look towards future improvements, it's important to acknowledge the limitations of the printer developed in this work, particularly in regard to printing speed. While we optimized the scanning paths to improve efficiency, the printing process could still take several days if every single layer is filled with patterns requiring optics to scan the entire layer. One potential solution to this issue could be the incorporation of parallel projectors, which could significantly boost printing speed by allowing multiple areas to be cured simultaneously. Additionally, other strategies, such as optimizing the resin properties, adjusting the exposure time, and improving the motion control system, can also contribute to improving the printing speed without sacrificing the quality of the final product.

Overall, while our current system has limitations in terms of printing speed, we believe that there is significant potential for future improvements and developments that will allow us to overcome these challenges and further enhance the capabilities of our printer.

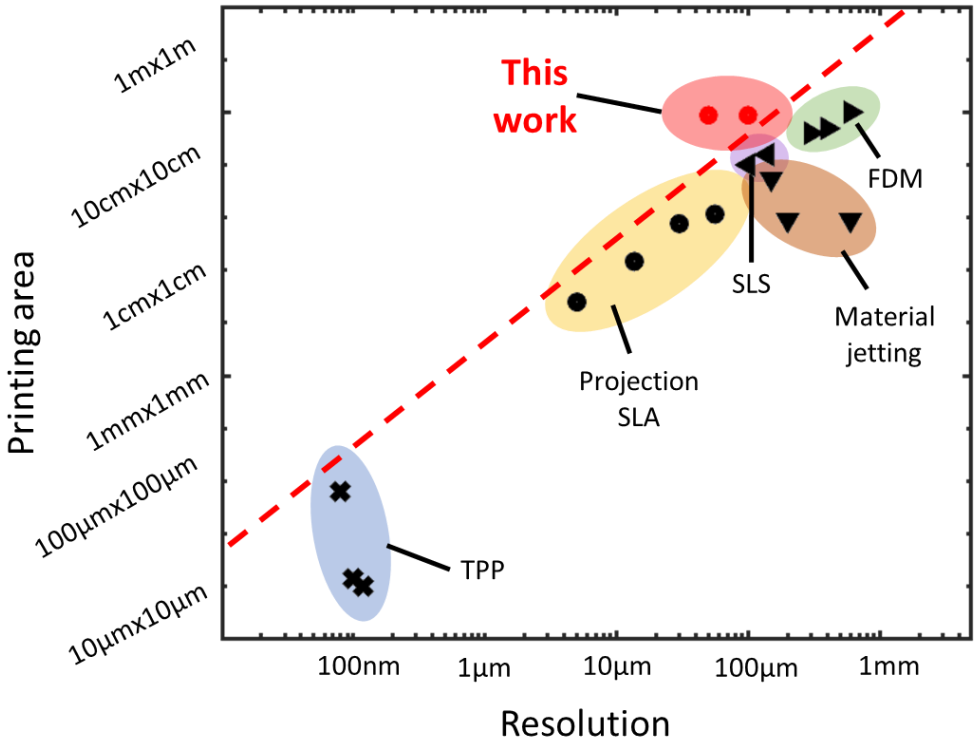

Figure 5-15 The diagram summarizes the printing resolution and printing area relation of various AM techniques, including TPP, projection SLA, SLS, material jetting, and FDM.

In this chapter, we present a significant advancement in the field of 3D printing by developing a large-scale, high-resolution projection stereolithography printer. The integration of moving optics allows for printing large-scale structural materials and devices while maintaining a high resolution of 50 μm. Our optical scanning strategy is the key to achieving this breakthrough, enabling the printer to enlarge the printing area without sacrificing resolution. We showcase our system's capabilities by demonstrating the printing of large lattice material made of CFRP with a size of up

to 50 cm, which was previously unattainable with such high resolution. Furthermore, we demonstrate the potential of our technology by producing a novel car bumper energy absorber. This lightweight and energy-dissipating material can be deployed in automotive parts that require both safety and efficiency. Our technology presents new opportunities for the vehicle industry to manufacture large-sized components with complex structures that were previously impossible to achieve with conventional manufacturing methods. Overall, this work represents a significant step towards revolutionizing the field of 3D printing, and we believe that it has a profound impact not only on the industry but also on other research works.

Chapter 6 Conclusion and future work

6.1 Conclusion and answering the research questions

This dissertation presents the development of several innovative additive manufacturing processes for PSL. These new processes mainly solved acute problems that hindered the development of PSL in various application fields.

One of the major challenges faced in PSL is the limited range of materials that can be used, particularly high-viscosity resins. High-viscosity resins have the potential to produce materials with enhanced mechanical and physical properties, which are essential for many applications. However, the slow recoating process for these materials makes it challenging to print them with PSL. To overcome this limitation, the author developed a process that enables the fast recoating process for high-viscosity resins, thereby enabling the printing of high-viscosity composites. The author used the system to fabricate carbon fiber reinforced polymer composites, demonstrating superior mechanical performance.

In PSL, printing micro-architectures with many inner overhangs at the micro-scale can be a challenging task. These overhangs can cause deformations in the structure and lead to errors in the printed product. To address this issue, the author developed a selective dissolution methodology. The selective dissolution methodology involves printing the desired structure with a support structure made of a different material that is easily dissolved. After printing, the structure is immersed in a selective solvent that only dissolves the support material while leaving the printed structure intact. This process allows for the removal of the support material without affecting the

printed structure's integrity, thereby enabling the printing of micro-architectures with many inner overhangs at the micro-scale. The selective dissolution methodology developed by the author has broad implications for the development of micro-structures with complex geometries. This process enables the printing of structures that were previously impossible to manufacture with PSL. It also allows for the printing of structures with intricate inner overhangs, such as some variation attenuation structures, which are essential for many acoustic applications. The selective dissolution methodology can be further optimized to increase its efficiency and versatility. By using different types of support materials and selective solvents, the process can be adapted to different kinds of structures and applications.

PSL is an excellent method for the fabrication of complex micro-structures, but the limited build volume of the printing platform can be a challenge for the manufacturing of large-scale structures. Moreover, increasing the build volume can lead to a decrease in printing resolution, which can compromise the final product's quality. To overcome this challenge, the author developed a process that allows large-scale structures to be produced without sacrificing resolution. The developed process employs a scanning projection system to project the light onto the printing platform via two translation stages, which allows for the printing of large-scale structures while maintaining high resolution. This process enables the printing of large-scale structures with high resolution, allowing for the manufacturing of structures that require both large size and small features.

RQ 1 How to enable the printing of highly viscous composites for use in projection stereolithography?

Printing highly viscous composites for use in PSL can be a challenging task, but there are several approaches that can be used to enable successful printing:

1. Integrate tape-casting fixture for recoating: The author introduced a novel tape-casting fixture that is specifically designed for high-viscosity CFRP resins. The presented CFRP resin exhibits a shear-thinning effect, meaning that its viscosity decreases as the shear rate increases, allowing it to flow under pressure. Consequently, this method eliminates the need for gravitational settling of the resin, making it ideal for highly viscous materials.
2. Adjust the viscosity: One of the most effective ways to enable the printing of highly viscous composites is to adjust their viscosity. This can be done by adding solvents or other liquids to the composite. Alternatively, it may be possible to select a different resin with a lower viscosity that still meets the required material properties. This study employed PEGDA, a low-viscosity polymer with a viscosity of approximately 0.025 Pa·s, as the diluter. The results demonstrated that incorporating 25 wt% PEGDA into the resin considerably decreased its viscosity, making the recoating process significantly easier. The selection of PEGDA as a diluter was based on its desirable mechanical properties in addition to its low viscosity. The final printed part using the diluted resin exhibited a slightly lower Young's Modulus in comparison to the resin without a diluter, and the Modulus/Viscosity ratio was found to be adjustable by modifying the diluter concentration.

3. Heating: Another method to reduce the viscosity of the resin is through heating. The author implemented a heating system that could be integrated with the printing process. The heating element has the capability of reaching a temperature of up to 130℃, which heats the resin to over 90℃ within a few minutes. Experimental results indicate that the viscosity of the resin decreases when heated, thereby simplifying the recoating process.

Overall, successful printing of highly viscous composites in PSL requires a combination of careful material selection, printer optimization, and process adjustments to ensure that the composite can be deposited and cured effectively.

RQ 2 How to print architectured materials with numerous inner overhangs at the micro-scale?

Printing architectured materials with many inner overhangs at the micro-scale can pose a significant challenge, as many micro-scale fabrication techniques are not support-free. Traditional techniques such as TPP, PSL, and DIW require support structures to print overhangs. Commercial inkjet printers often use sacrificial materials that dissolve after printing multiple materials, but they are limited in terms of the resins that can be used due to the nozzle of the inkjet. To address this challenge, this work proposes an mSLAD (multi-material stereolithography selective dissolution) process for printing structures with dissolvable supports. This process can be used to fabricate a variety of resins, including particle-loaded composites. While the technique was initially developed for PSL, it holds great potential for application in TPP and DIW as well.

To enable the successful printing of micro-architectures, several suggestions can be considered:

1. Design for overhangs: Designing the material and its geometry specifically to account for overhangs can help facilitate printing. Design strategies such as creating inclined surfaces, adding support structures, or incorporating self-supporting geometries can help to reduce the need for support structures and improve the likelihood of successful printing.
2. Use multi-material printing: Multi-material printing enables the use of different materials with varying properties in a single print. Using different materials may be possible to print overhangs that would otherwise be impossible to create with a single material.
3. Use support structures: One of the most common ways to print materials with overhangs is to use support structures. These structures are typically printed alongside the material and are designed to provide temporary support to prevent sagging or collapsing during printing. After printing is complete, the support structures can be removed through a dissolving process.

RQ 3 How to develop new AM processes to increase the building area of projection stereolithography while maintaining a high level of resolution?

Two ways can be considered to develop new processes to increase the building area of projection stereolithography while maintaining a high level of resolution:

1. Multi-projection technology: One approach is to use multiple projectors to expose the entire build area simultaneously, reducing the need for scanning and increasing the printing speed.
2. High-speed scanning: Another approach is to use high-speed scanning systems that can scan the build area more quickly while still maintaining high resolution.

While multi-projection is definitely the fastest way to extend the building area while maintaining a good printing resolution, the cost of such a system is high. In this work, the author proposes an alternative approach that involves using a scanning PSL system. This system incorporates two scanning mirrors with a baseline PSL system, allowing for the enlargement of the printing area while still maintaining a high level of resolution. Additionally, the system has the potential to be upgraded to enable continuous exposure, which would synchronize the motion of the scanning mirrors with the UV exposure, further improving the printing speed and efficiency.

RQ 4 What are the new opportunities enabled by projection stereolithography?

Projection stereolithography has opened up new opportunities in the field of AM due to its ability to create complex structures with high precision and accuracy. From this work, the author concludes some of the new opportunities enabled by PSL:

1. High-resolution printing: PSL can produce parts with high resolution and accuracy, making it possible to create detailed, intricate geometries that are difficult to achieve with traditional manufacturing techniques.
2. Multi-material printing: PSL can print with multiple materials simultaneously, enabling the creation of parts with varying properties and characteristics.
3. Large-scale manufacturing: PSL can be scaled up to enable large-scale manufacturing, making it suitable for producing a wide range of products, from small, intricate parts to large, complex structures.

4. Materials: PSL can accommodate a wide range of resins, from regular polymers to composites and hydrogels. This flexibility allows for the incorporation of various functionalities that can benefit numerous application areas.

6.2 Future Work

(1) Controlling the fiber orientation can enhance the mechanical properties of carbon fiber reinforced polymer composites. This process can also be applied to the printing of piezoelectric composites. By controlling the orientation of the piezo fibers, it is possible to achieve superior performance along specific directions, such as improved electrical conductivity, increased piezoelectric activity, and higher mechanical strength. Various methods can be employed to align the fibers. For example, the electric field can be applied for alignment due to the interaction between the electric field and the dipole moments of the piezo fibers. Similarly, magnetic fields can also be employed. Lastly, vibrations can also be utilized to align the fibers, as mechanical vibrations can induce an alignment of the fibers along a specific direction. By applying these methods, it is possible to achieve precise control over the orientation of piezo fibers in the printed composites. This can lead to significant improvements in the performance of piezoelectric devices, particularly in terms of their sensitivity, durability, and energy conversion efficiency. Further research is required to explore the full potential of these techniques and optimize their use in various applications.

(2) As a potential avenue for future research, the use of machine-vision in-situ monitoring of the projection pattern could be incorporated to enhance the printing process for the large-scale high-resolution printing system. This technology has the potential to detect defects and other issues that

may arise during large-scale printing, providing real-time feedback to optimize the printing process and improve the final product's overall quality. To effectively implement this technology, several critical factors would need to be addressed. These include selecting an appropriate wavelength for the monitoring light source, designing effective monitoring patterns, and setting up a closed-loop control motion system. By tackling these issues, it may be possible to significantly improve the success rate and overall quality of large-scale printing using projection stereolithography.

(3) There is potential for further research into the creation and optimization of magnetoelectric energy harvesters using the multi-material AM platform. While the presented work has laid the groundwork for incorporating magnetic particles into UV-sensitive monomers, there are still many opportunities to refine the process and improve device performance. For example, by incorporating both piezoelectric and magnetic particles into the UV-sensitive monomer, it is possible to create highly effective magnetoelectric energy harvesting devices. One area of focus for future investigations could be optimizing particle loadings to maximize power density. This may involve testing different particle sizes, shapes, and compositions to identify the optimal combination for the desired application. Additionally, designing geometries based on magnetic field distributions could be explored as a means to improve overall device efficiency. By further refining the fabrication process and exploring new design strategies, it may be possible to significantly enhance the performance of these devices and unlock new opportunities for renewable energy applications.

References

[1] Z.P. Xu, C.S. Ha, R. Kadam, J. Lindahl, S. Kim, H.F. Wu, V. Kunc, X. Zheng, Additive manufacturing of two-phase lightweight, stiff and high damping carbon fiber reinforced polymer microlattices, Addit Manuf 32 (2020).

[2] A.G. Izard, L. Valdevit, Magnetoelastic Metamaterials for Energy Dissipation and Wave Filtering, Adv Eng Mater 22(2) (2020).

[3] R. Hensleigh, H.C. Cui, Z.P. Xu, J. Massman, D.S. Yao, J. Berrigan, X.Y. Zheng, Charge-programmed three-dimensional printing for multi-material electronic devices, Nat Electron 3(4) (2020) 216-224.

[4] D.S. Yao, H.C. Cui, R. Hensleigh, P. Smith, S. Alford, D. Bernero, S. Bush, K. Mann, H.F. Wu, M. Chin-Nieh, G. Youmans, X.Y. Zheng, Achieving the Upper Bound of Piezoelectric Response in Tunable, Wearable 3D Printed Nanocomposites, Adv Funct Mater 29(42) (2019).

[5] N.J.R.K. Gerard, H.C. Cui, C. Shen, Y.B. Xie, S. Cummer, X.Y. Zheng, Y. Jing, Fabrication and experimental demonstration of a hybrid resonant acoustic gradient index metasurface at 40 kHz, Appl Phys Lett 114(23) (2019).

[6] S.M. Montgomery, S. Wu, X. Kuang, C.D. Armstrong, C. Zemelka, Q.J. Ze, R.D. Zhang, R.K. Zhao, H.J. Qi, Magneto-Mechanical Metamaterials with Widely Tunable Mechanical Properties and Acoustic Bandgaps, Adv Funct Mater 31(3) (2021).

[7] Y.F. Zhu, N.J.R.K. Gerard, X.X. Xia, G.C. Stevenson, L.Y. Cao, S.W. Fan, C.M. Spadaccini, Y. Jing, B. Assouar, Systematic Design and Experimental Demonstration of Transmission-Type Multiplexed Acoustic Metaholograms, Adv Funct Mater (2021).

[8] C.W. Wang, W.W. Ping, Q. Bai, H.C. Cui, R. Hensleigh, R.L. Wang, A.H. Brozena, Z.P. Xu, J.Q. Dai, Y. Pei, C.L. Zheng, G. Pastel, J.L. Gao, X.Z. Wang, H. Wang, J.C. Zhao, B. Yang, X.Y. Zheng, J. Luo, Y.F. Mo, B. Dunn, L.B. Hu, A general method to synthesize and sinter bulk ceramics in seconds, Science 368(6490) (2020) 521-+.

[9] H.C. Cui, R. Hensleigh, D.S. Yao, D. Maurya, P. Kumar, M.G. Kang, S. Priya, X.Y. Zheng, Three-dimensional printing of piezoelectric materials with designed anisotropy and directional response, Nat Mater 18(3) (2019) 234-+.

[10] H.C. Cui, R. Hensleigh, H.S. Chen, X.Y. Zheng, Additive Manufacturing and size-dependent mechanical properties of three-dimensional microarchitected, high-temperature ceramic metamaterials, J Mater Res 33(3) (2018) 360-371.

[11] M. Imran, L.C. Zhang, A.K. Gain, Advanced thermal metamaterial design for temperature control at the cloaked region, Sci Rep-Uk 10(1) (2020).

[12] M. Kadic, T. Buckmann, N. Stenger, M. Thiel, M. Wegener, On the practicability of pentamode mechanical metamaterials (vol 100, 191901, 2012), Appl Phys Lett 101(4) (2012).

[13] C.S. Ha, R.S. Lakes, M.E. Plesha, Cubic negative stiffness lattice structure for energy absorption: Numerical and experimental studies, Int J Solids Struct 178 (2019) 127-135.

[14] C.S. Ha, R.S. Lakes, M.E. Plesha, Design, fabrication, and analysis of lattice exhibiting energy absorption via snap-through behavior, Mater Design 141 (2018) 426-437.

[15] A. Rafsanjani, A. Akbarzadeh, D. Pasini, Snapping Mechanical Metamaterials under Tension, Adv Mater 27(39) (2015) 5931-5935.

[16] T. Frenzel, C. Findeisen, M. Kadic, P. Gumbsch, M. Wegener, Tailored Buckling Microlattices as Reusable Light-Weight Shock Absorbers, Adv Mater 28(28) (2016) 5865-+.

[17] D. Chen, X.Y. Zheng, Multi-material Additive Manufacturing of Metamaterials with Giant, Tailorable Negative Poisson's Ratios, Sci Rep-Uk 8 (2018).

[18] X.T. Wang, B. Wang, X.W. Li, L. Ma, Mechanical properties of 3D re-entrant auxetic cellular structures, Int J Mech Sci 131 (2017) 396-407.

[19] T. Frenzel, M. Kadic, M. Wegener, Three-dimensional mechanical metamaterials with a twist, Science 358(6366) (2017) 1072-1074.

[20] W.W. Wu, D.X. Qi, H.T. Liao, G. Qian, L.C. Geng, Y.H. Niu, J. Liang, Deformation mechanism of innovative 3D chiral metamaterials, Sci Rep-Uk 8 (2018).

[21] Y.Y. Jiang, Y.N. Li, Novel 3D-Printed Hybrid Auxetic Mechanical Metamaterial with Chirality-Induced Sequential Cell Opening Mechanisms, Adv Eng Mater 20(2) (2018).

[22] K.H. Yu, N.X. Fang, G.L. Huang, Q.M. Wang, Magnetoactive Acoustic Metamaterials, Adv Mater 30(21) (2018).

[23] N. Kladovasilakis, K. Tsongas, D. Karalekas, D. Tzetzis, Architected materials for additive manufacturing: A comprehensive review, Materials 15(17) (2022) 5919.

[24] L. Olmos, E. Mihalcea, H. Vergara-Hernández, D. Bouvard, O. Jimenez, J. Chávez, N. Camacho, R. Macías, Design of architectured Ti6Al4V-based materials for biomedical applications fabricated via powder metallurgy, Materials Today Communications 29 (2021) 102937.

[25] Z. Lyu, G.J. Lim, J.J. Koh, Y. Li, Y. Ma, J. Ding, J. Wang, Z. Hu, J. Wang, W. Chen, Design and manufacture of 3D-printed batteries, Joule 5(1) (2021) 89-114.

[26] S.C. Joshi, A.A. Sheikh, 3D printing in aerospace and its long-term sustainability, Virtual Phys Prototy 10(4) (2015) 175-185.

[27] H. Xu, D. Pasini, Structurally efficient three-dimensional metamaterials with controllable thermal expansion, Sci Rep-Uk 6(1) (2016) 1-8.

[28] F. Zhang, L. Wang, Z. Zheng, Y. Liu, J. Leng, Magnetic programming of 4D printed shape memory composite structures, Elsevier, 2019.

[29] D. Behera, S. Chizari, L.A. Shaw, M. Porter, R. Hensleigh, Z. Xu, N.K. Roy, L.G. Connolly, X.R. Zheng, S. Saha, Current challenges and potential directions towards precision microscale additive manufacturing–Part II: Laser-based curing, heating, and trapping processes, Precision Engineering 68 (2021) 301-318.

[30] C. Sun, N. Fang, D. Wu, X. Zhang, Projection micro-stereolithography using digital micro-mirror dynamic mask, Sensors and Actuators A: Physical 121(1) (2005) 113-120.

[31] J.R. Tumbleston, D. Shirvanyants, N. Ermoshkin, R. Janusziewicz, A.R. Johnson, D. Kelly, K. Chen, R. Pinschmidt, J.P. Rolland, A. Ermoshkin, Continuous liquid interface production of 3D objects, Science 347(6228) (2015) 1349-1352.

[32] D.A. Walker, J.L. Hedrick, C.A. Mirkin, Rapid, large-volume, thermally controlled 3D printing using a mobile liquid interface, Science 366(6463) (2019) 360-364.

[33] M. Askari, D.A. Hutchins, P.J. Thomas, L. Astolfi, R.L. Watson, M. Abdi, M. Ricci, S. Laureti, L.Z. Nie, S. Freear, R. Wildman, C. Tuck, M. Clarke, E. Woods, A.T. Clare, Additive manufacturing of metamaterials: A review, Addit Manuf 36 (2020).

[34] S. Kumar, S.H. Tan, L. Zheng, D.M. Kochmann, Inverse-designed spinodoid metamaterials, Npj Comput Mater 6(1) (2020).

[35] J.C. Jiang, X. Xu, J. Stringer, Support Structures for Additive Manufacturing: A Review, J Manuf Mater Proc 2(4) (2018).

[36] X.J. Chen, J.L. Hu, Q.L. Zhou, C. Politis, Y. Sun, An automatic optimization method for minimizing supporting structures in additive manufacturing, Adv Manuf 8(1) (2020) 49-58.

[37] F. Calignano, Design optimization of supports for overhanging structures in aluminum and titanium alloys by selective laser melting, Mater Design 64 (2014) 203-213.

[38] J.K. Liu, A.T. Gaynor, S.K. Chen, Z. Kang, K. Suresh, A. Takezawa, L. Li, J. Kato, J.Y. Tang, C.C.L. Wang, L. Cheng, X. Liang, A.C. To, Current and future trends in topology optimization for additive manufacturing, Struct Multidiscip O 57(6) (2018) 2457-2483.

[39] Z.J. Wu, L. Xia, S.T. Wang, T.L. Shi, Topology optimization of hierarchical lattice structures with substructuring, Comput Method Appl M 345 (2019) 602-617.

[40] Y.W. Mao, Q. He, X.H. Zhao, Designing complex architectured materials with generative adversarial networks, Sci Adv 6(17) (2020).

[41] Z. Xu, R. Hensleigh, N.J. Gerard, H. Cui, M. Oudich, W. Chen, Y. Jing, X.R. Zheng, Vat photopolymerization of fly-like, complex micro-architectures with dissolvable supports, Addit Manuf 47 (2021) 102321.

[42] D. Behera, S. Chizari, L.A. Shaw, M. Porter, R. Hensleigh, Z. Xu, X. Zheng, L.G. Connolly, N.K. Roy, R.M. Panas, Current challenges and potential directions towards precision microscale additive manufacturing–Part IV: Future perspectives, Precision Engineering 68 (2021) 197-205.

[43] M.P. Lee, G.J. Cooper, T. Hinkley, G.M. Gibson, M.J. Padgett, L. Cronin, Development of a 3D printer using scanning projection stereolithography, Sci Rep-Uk 5(1) (2015) 9875.

[44] M.M. Emami, F. Barazandeh, F. Yaghmaie, Scanning-projection based stereolithography: Method and structure, Sensors and Actuators A: Physical 218 (2014) 116-124.

[45] V. Meenakshisundaram, L.D. Sturm, C.B. Williams, Modeling A scanning-mask projection vat photopolymerization system for multiscale additive manufacturing, Journal of Materials Processing Technology 279 (2020) 116546.

[46] X.Y. Zheng, W. Smith, J. Jackson, B. Moran, H.C. Cui, D. Chen, J.C. Ye, N. Fang, N. Rodriguez, T. Weisgraber, C.M. Spadaccini, Multiscale metallic metamaterials, Nat Mater 15(10) (2016) 1100-+.

[47] J. Wang, A. Papathanasopoulos, Y. Rahmat-Samii, R. Hensleigh, Z. Xu, X. Zheng, Ultra-lightweight transmitarray antenna enabled by charge-programmed three-dimensional multi-material printing, 2022 United States National Committee of URSI National Radio Science Meeting (USNC-URSI NRSM), IEEE, 2022, pp. 293-294.

[48] J. Wang, R. Hensleigh, Z. Xu, Z. Wang, X. Zheng, Y. Rahmat-Samii, Fully 3D-Printed Lightweight Combination of a Circularly Polarized Transmitarray and a Feed Horn, 2022 IEEE International Symposium on Antennas and Propagation and USNC-URSI Radio Science Meeting (AP-S/URSI), IEEE, 2022, pp. 645-646.

[49] D. Han, C. Yang, N.X. Fang, H. Lee, Rapid multi-material 3D printing with projection micro-stereolithography using dynamic fluidic control, Addit Manuf 27 (2019) 606-615.

[50] X. Mu, T. Bertron, C. Dunn, H. Qiao, J. Wu, Z. Zhao, C. Saldana, H.J. Qi, Porous polymeric materials by 3D printing of photocurable resin, Mater Horiz 4(3) (2017) 442-449.

[51] X. Song, Y. Chen, T.W. Lee, S.H. Wu, L.X. Cheng, Ceramic fabrication using Mask-Image-Projection-based Stereolithography integrated with tape-casting, J Manuf Process 20 (2015) 456-464.

[52] X.Y. Zheng, J. Deotte, M.P. Alonso, G.R. Farquar, T.H. Weisgraber, S. Gemberling, H. Lee, N. Fang, C.M. Spadaccini, Design and optimization of a light-emitting diode projection micro-stereolithography three-dimensional manufacturing system, Rev Sci Instrum 83(12) (2012).

[53] A. Badev, Y. Abouliatim, T. Chartier, L. Lecamp, P. Lebaudy, C. Chaput, C. Delage, Photopolymerization kinetics of a polyether acrylate in the presence of ceramic fillers used in stereolithography, Journal of Photochemistry and Photobiology A: Chemistry 222(1) (2011) 117-122.

[54] T. Schlotthauer, D. Nolan, P. Middendorf, Influence of short carbon and glass fibers on the curing behavior and accuracy of photopolymers used in stereolithography, Addit Manuf 42 (2021) 102005.

[55] Y. Pan, H. He, J. Xu, A. Feinerman, Study of separation force in constrained surface projection stereolithography, Rapid Prototyping Journal 23(2) (2017) 353-361.

[56] G.D. Goh, Y.L. Yap, S. Agarwala, W.Y. Yeong, Recent Progress in Additive Manufacturing of Fiber Reinforced Polymer Composite, Advanced Materials Technologies 4(1) (2019) 1-22.

[57] F. Ning, W. Cong, J. Qiu, S. Wang, Additive manufacturing of carbon fiber reinforced thermoplastic composites using fused deposition modeling, Composites Part B: Engineering 80 (2015) 369-378.

[58] X.Y. Zheng, H. Lee, T.H. Weisgraber, M. Shusteff, J. DeOtte, E.B. Duoss, J.D. Kuntz, M.M. Biener, Q. Ge, J.A. Jackson, S.O. Kucheyev, N.X. Fang, C.M. Spadaccini, Ultralight, Ultrastiff Mechanical Metamaterials, Science 344(6190) (2014) 1373-1377.

[59] V.S. Deshpande, N.A. Fleck, M.F. Ashby, Effective properties of the octet-truss lattice material, J Mech Phys Solids 49(8) (2001) 1747-1769.

[60] L. Dong, V. Deshpande, H. Wadley, Mechanical response of Ti-6Al-4V octet-truss lattice structures, Int J Solids Struct 60-61 (2015) 107-124.

[61] S.A. Khanoki, D. Pasini, Multiscale Design and Multiobjective Optimization of Orthopedic Hip Implants with Functionally Graded Cellular Material, J Biomech Eng-T Asme 134(3) (2012).

[62] A.G. Evans, J.W. Hutchinson, M.F. Ashby, Multifunctionality of cellular metal systems, Prog Mater Sci 43(3) (1998) 171-221.

[63] L.J. Gibson, M.F. Ashby, Cellular materials: Structure and Properties, Cellular materials, University Press, Cambridge, 1999.

[64] C. Tekoglu, P.R. Onck, Size effects in the mechanical behavior of cellular materials, J Mater Sci 40(22) (2005) 5911-5917.

[65] L. Yang, A study about size effects of 3D periodic cellular structures, Proceedings of the 27th International Solid Freeform Fabrication (SFF) Symposium, Austin, TX, 2016.

[66] R. Lakes, Viscoelastic Materials, Cambridge University Press, 2009.

[67] C.P. Chen, R.S. Lakes, Analysis of High-Loss Viscoelastic Composites, J Mater Sci 28(16) (1993) 4299-4304.

[68] L. Salari-Sharif, T.A. Schaedler, L. Valdevit, Energy dissipation mechanisms in hollow metallic microlattices, J Mater Res 29(16) (2014) 1755-1770.

[69] H.R. Shercliff, M.F. Ashby, Elastic Structures in Design, Encycl. Mater. Sci. Technol. (2001) 2429–2433.

[70] L. Salari-Sharif, T.A. Schaedler, L. Valdevit, Hybrid Hollow Microlattices With Unique Combination of Stiffness and Damping, J Eng Mater-T Asme 140(3) (2018).

[71] A. Asadpoure, M. Tootkaboni, L. Valdevit, Topology optimization of multiphase architected materials for energy dissipation, Comput Method Appl M 325 (2017) 314-329.

[72] M.F. Ashby, Materials Selection in Mechanical Design, 2nd ed., Butterworth Heinemann, Oxford, 1999.

[73] G. Design, CES EduPack 2018, 2019. https://grantadesign.com/education/ces-edupack/. (Accessed 25 NOV 2019).

[74] R. Liska, F. Schwager, C. Maier, R. Cano-Vives, J. Stampfl, Water-soluble photopolymers for rapid prototyping of cellular materials, J Appl Polym Sci 97(6) (2005) 2286-2298.

[75] Y.L. Yap, W.Y. Yeong, Additive manufacture of fashion and jewellery products: a mini review This paper provides an insight into the future of 3D printing industries for fashion and jewellery products, Virtual Phys Prototy 9(3) (2014) 195-201.

[76] F. Bertacchini, E. Bilotta, F. Demarco, P. Pantano, C. Scuro, Multi-objective optimization and rapid prototyping for jewelry industry: methodologies and case studies, Int J Adv Manuf Tech 112(9-10) (2021) 2943-2959.

[77] W.J. Zhang, S.Y. Zhao, R.J. Sun, F. Scarpa, J.W. Wang, In-Plane Mechanical Behavior of a New Star-Re-Entrant Hierarchical Metamaterial, Polymers-Basel 11(7) (2019).

[78] Y.Y. Chen, T.T. Li, F. Scarpa, L.F. Wang, Lattice Metamaterials with Mechanically Tunable Poisson's Ratio for Vibration Control, Phys Rev Appl 7(2) (2017).

[79] T. Strek, H. Jopek, K.W. Wojciechowski, The influence of large deformations on mechanical properties of sinusoidal ligament structures, Smart Mater Struct 25(5) (2016).

[80] N.J. Gerard, M. Oudich, Y. Jing, Omnidirectional elastic wave attenuation via an isotoxal-star-based auxetic micro-lattice, arXiv preprint arXiv:1912.08260 (2019).

[81] N.J. Gerard, M. Oudich, Z. Xu, D. Yao, H. Cui, C.J. Naify, A. Ikei, C.A. Rohde, X. Zheng, Y. Jing, Three-Dimensional Trampolinelike Behavior in an Ultralight Elastic Metamaterial, Phys Rev Appl 16(2) (2021) 024015.

[82] S.J. Park, J.E. Lee, J.H. Park, N.K. Lee, M.Y. Lyu, K. Park, M.S. Koo, S.H. Cho, Y. Son, S.H. Park, Enhanced Solubility of the Support in an FDM-Based 3D Printed Structure Using Hydrogen Peroxide under Ultrasonication, Adv Mater Sci Eng 2018 (2018).

[83] P. Polamaplly, Y.L. Cheng, X.L. Shi, K. Manikandan, X. Zhang, G.E. Kremer, H.T. Qin, 3D printing and characterization of hydroxypropyl methylcellulose and methylcellulose for biodegradable support structures, Polymer 173 (2019) 119-126.

[84] A. Kumar, S. Verma, J.Y. Jeng, Supportless Lattice Structures for Energy Absorption Fabricated by Fused Deposition Modeling, 3d Print Addit Manuf 7(2) (2020) 85-96.

[85] Protolabs, Design Guidelines for Selective Laser Sintering (SLS), 2021. https://www.protolabs.com/. (Accessed 05/31 2021).

[86] A. Awad, F. Fina, A. Goyanes, S. Gaisford, A.W. Basit, 3D printing: Principles and pharmaceutical applications of selective laser sintering, Int J Pharmaceut 586 (2020).

[87] T. Xu, W. Shen, X.S. Lin, Y.M. Xie, Mechanical Properties of Additively Manufactured Thermoplastic Polyurethane (TPU) Material Affected by Various Processing Parameters, Polymers-Basel 12(12) (2020).

[88] H.Z. Wu, O.X. Wang, Y.J. Tian, M.Z. Wang, B. Su, C.Z. Yan, K. Zhou, Y.S. Shi, Selective Laser Sintering-Based 4D Printing of Magnetism-Responsive Grippers, Acs Appl Mater Inter 13(11) (2021) 12679-12688.

[89] W. Li, A. Ghazanfari, D. McMillen, M.C. Leu, G.E. Hilmas, J. Watts, Fabricating ceramic components with water dissolvable support structures by the Ceramic On-Demand Extrusion process, Cirp Ann-Manuf Techn 66(1) (2017) 225-228.

[90] V.C.F. Li, X. Kuang, C.M. Hamel, D. Roach, Y.L. Deng, H.J. Qi, Cellulose nanocrystals support material for 3D printing complexly shaped structures via multi-materials-multi-methods printing, Addit Manuf 28 (2019) 14-22.

[91] Q.Q. Zhang, F. Zhang, S.P. Medarametla, H. Li, C. Zhou, D. Lin, 3D Printing of Graphene Aerogels, Small 12(13) (2016) 1702-1708.

[92] Y.F. He, F. Zhang, E. Saleh, J. Vaithilingam, N. Aboulkhair, B. Begines, C.J. Tuck, R.J.M. Hague, I.A. Ashcroft, R.D. Wildman, A Tripropylene Glycol Diacrylate-based Polymeric Support Ink for Material Jetting, Addit Manuf 16 (2017) 153-161.

[93] L. He, F. Fei, W.B. Wang, X. Song, Support-Free Ceramic Stereolithography of Complex Overhanging Structures Based on an Elasto-viscoplastic Suspension Feedstock, Acs Appl Mater Inter 11(20) (2019) 18849-18857.

[94] J. Jin, Y. Chen, Highly removable water support for Stereolithography, J Manuf Process 28 (2017) 541-549.

[95] P.J. Bártolo, Stereolithography: materials, processes and applications, Springer Science & Business Media2011.

[96] Nikon, Infinity Optical Systems, 2021. https://www.microscopyu.com/microscopy-basics/infinity-optical-systems. (Accessed 07/12 2021).

[97] Thorlabs, Does collimated light maintain a constant beam diameter out to infinity?, 2023. https://www.thorlabs.com/newgrouppage9.cfm?objectgroup_id=14489. (Accessed 03/03 2023).

[98] J. Kirk, Fixed start open traveling salesman problem genetic algorithm in matlab, 2014. http://freesourcecode.net/matlabprojects/56913/fixed-start-open-traveling-salesman-problem---genetic-algorithm-in-matlab#.YXzW9LFXqpE. (Accessed 10/29 2021).

[99] Y. Xu, Y. Zhu, Y. Sun, J. Jin, Y. Chen, A vibration-assisted separation method for constrained-surface-based stereolithography, Journal of Manufacturing Science and Engineering 143(5) (2021).

[100] C. Zhou, Y. Chen, Z. Yang, B. Khoshnevis, Digital material fabrication using mask-image-projection-based stereolithography, Rapid Prototyping Journal (2013).

[101] X. Wu, Q. Lian, D. Li, Z. Jin, Tilting separation analysis of bottom-up mask projection stereolithography based on cohesive zone model, Journal of Materials Processing Technology 243 (2017) 184-196.

[102] F. Liravi, S. Das, C. Zhou, Separation force analysis and prediction based on cohesive element model for constrained-surface Stereolithography processes, Computer-Aided Design 69 (2015) 134-142.

[103] A. Maier, R. Schmidt, B. Oswald-Tranta, R. Schledjewski, Non-destructive thermography analysis of impact damage on large-scale CFRP automotive parts, Materials 7(1) (2014) 413-429.

[104] P. Yeole, A.A. Hassen, S. Kim, J. Lindahl, V. Kunc, A. Franc, U. Vaidya, Mechanical characterization of high-temperature carbon fiber-polyphenylene sulfide composites for large area extrusion deposition additive manufacturing, Addit Manuf 34 (2020) 101255.

[105] S. Kim, G.D. Dreifus, B.T. Beard, A. Glick, A.K. Messing, A.A. Hassen, J.M. Lindahl, P. Liu, T. Smith, J.A. Failla, Graded infill structure of wind turbine blade accounting for internal stress in big area additive manufacturing, Oak Ridge National Lab.(ORNL), Oak Ridge, TN (United States), 2018.

[106] Q.M. Wang, J.A. Jackson, Q. Ge, J.B. Hopkins, C.M. Spadaccini, N.X. Fang, Lightweight Mechanical Metamaterials with Tunable Negative Thermal Expansion, Phys Rev Lett 117(17) (2016) 175901.

[107] V.S. Deshpande, M.F. Ashby, N.A. Fleck, Foam topology bending versus stretching dominated architectures, Acta Mater 49(6) (2001) 1035-1040.

[108] D.R. Clarke, Interpenetrating Phase Composites, J Am Ceram Soc 75(4) (1992) 739-759.

[109] L.D. Wegner, L.J. Gibson, The mechanical behaviour of interpenetrating phase composites - I: modelling, Int J Mech Sci 42(5) (2000) 925-942.

[110] O. Al-Ketan, M.A. Assad, R.K. Abu Al-Ru, Mechanical properties of periodic interpenetrating phase composites with novel architected microstructures, Compos Struct 176 (2017) 9-19.

[111] Z.Y. Xue, J.W. Hutchinson, A comparative study of impulse-resistant metal sandwich plates, Int J Impact Eng 30(10) (2004) 1283-1305.

[112] K.H. Ha, Finite-Element Analysis of Sandwich Plates - an Overview, Comput Struct 37(4) (1990) 397-403.

[113] A. Uzal, F.O. Sonmez, F.E. Oz, K. Cinar, N. Ersoy, A composite sandwich plate with a novel core design, Compos Struct 193 (2018) 198-211.

[114] S.L. Chen, G.H. He, H. Hu, S.Q. Jin, Y. Zhou, Y.Y. He, S.J. He, F. Zhao, H.Q. Hou, Elastic carbon foam via direct carbonization of polymer foam for flexible electrodes and organic chemical absorption, Energ Environ Sci 6(8) (2013) 2435-2439.

[115] B.G. Compton, J.A. Lewis, 3D-Printing of Lightweight Cellular Composites, Adv Mater 26(34) (2014) 5930-+.

[116] B.P. Heller, D.E. Smith, D.A. Jack, Effects of extrudate swell and nozzle geometry on fiber orientation in Fused Filament Fabrication nozzle flow, Addit Manuf 12 (2016) 252-264.

[117] Y. Watanabe, Evaluation of fiber orientation in ferromagnetic short-fiber reinforced composites by magnetic anisotropy, J Compos Mater 36(8) (2002) 915-923.

[118] C.M. Cheah, J.Y.H. Fuh, A.Y.C. Nee, L. Lu, Mechanical characteristics of fiber-filled photo-polymer used in stereolithography, Rapid Prototyping Journal 5(3) (1999) 112-119.

[119] Y. Sano, R. Matsuzaki, M. Ueda, A. Todoroki, Y. Hirano, 3D printing of discontinuous and continuous fibre composites using stereolithography, Addit Manuf 24 (2018) 521-527.

[120] R. Xiao, M.Y. Ding, Y.J. Wang, L.B. Gao, R. Fan, Y. Lu, Stereolithography (SLA) 3D printing of carbon fiber-graphene oxide (CF-GO) reinforced polymer lattices, Nanotechnology 32(23) (2021).

[121] S.Y. Zhang, S. Bhagia, M. Li, X.Z. Meng, A.J. Ragauskas, Wood-reinforced composites by stereolithography with the stress whitening behavior, Mater Design 206 (2021).

[122] H.L. Tekinalp, V. Kunc, G.M. Velez-Garcia, C.E. Duty, L.J. Love, A.K. Naskar, C.A. Blue, S. Ozcan, Highly oriented carbon fiber-polymer composites via additive manufacturing, Compos Sci Technol 105 (2014) 144-150.

[123] Q. Ge, Z. Li, Z. Wang, K. Kowsari, W. Zhang, X. He, J. Zhou, N.X. Fang, Projection micro stereolithography based 3D printing and its applications, International Journal of Extreme Manufacturing 2(2) (2020) 022004.

[124] N.P. Macdonald, J.M. Cabot, P. Smejkal, R.M. Guijt, B. Paull, M.C. Breadmore, Comparing microfluidic performance of three-dimensional (3D) printing platforms, Analytical chemistry 89(7) (2017) 3858-3866.

[125] Prusa, Original Prusa MINI+ kit, 2023. https://www.prusa3d.com/product/original-prusa-mini-kit-3/. (Accessed 03/03 2023).

[126] Creality, Creality shop - Ender 3 DIY 3D Printers Kit, 2023. https://creality3d.shop/. (Accessed 03/03 2023).

[127] E. Jabari, F. Liravi, E. Davoodi, L. Lin, E. Toyserkani, High speed 3D material-jetting additive manufacturing of viscous graphene-based ink with high electrical conductivity, Addit Manuf 35 (2020) 101330.

[128] X. Shen, H.E. Naguib, A robust ink deposition system for binder jetting and material jetting, Addit Manuf 29 (2019) 100820.

[129] B. Hayes, T. Hainsworth, R. MacCurdy, Liquid–solid co-printing of multi-material 3D fluidic devices via material jetting, Addit Manuf 55 (2022) 102785.

[130] T. Inc, Additive production systems, 2023. https://www.trumpf.com/en_US/products/machines-systems/additive-production-systems/. (Accessed 03/03 2023).

[131] E. Inc, Systems and materials for additive manufacturing with metals, 2023. https://www.eos.info/en/industrial-3d-printer/metal. (Accessed 03/03 2023).

[132] Q. Ge, A.H. Sakhaei, H. Lee, C.K. Dunn, N.X. Fang, M.L. Dunn, Multimaterial 4D printing with tailorable shape memory polymers, Sci Rep-Uk 6(1) (2016) 1-11.

[133] R. Zhang, N.B. Larsen, Stereolithographic hydrogel printing of 3D culture chips with biofunctionalized complex 3D perfusion networks, Lab on a Chip 17(24) (2017) 4273-4282.

[134] A.I. Shallan, P. Smejkal, M. Corban, R.M. Guijt, M.C. Breadmore, Cost-effective three-dimensional printing of visibly transparent microchips within minutes, Analytical chemistry 86(6) (2014) 3124-3130.

[135] S. Kawata, H.-B. Sun, T. Tanaka, K. Takada, Finer features for functional microdevices, Nature 412(6848) (2001) 697-698.

[136] K. Takada, H.-B. Sun, S. Kawata, Improved spatial resolution and surface roughness in photopolymerization-based laser nanowriting, Appl Phys Lett 86(7) (2005) 071122.

[137] S.K. Saha, D. Wang, V.H. Nguyen, Y. Chang, J.S. Oakdale, S.-C. Chen, Scalable submicrometer additive manufacturing, Science 366(6461) (2019) 105-109.